ISBN 978-82-326-3708-9 (printed version)
ISBN 978-82-326-3709-6 (electronic version)
ISSN 1503-8181

Doctoral Thesis

Håkon Strandenes

Doctoral theses at NTNU, 2019:52

NTNU
Norwegian University of Science and Technology

Doctoral theses at NTNU, 2019:52

Håkon Strandenes

Turbulent flow simulations at higher Reynolds numbers

NTNU
Norwegian University of
Science and Technology
Faculty of Engineering
Department of MarineTechnology

NTNU
Norwegian University of
Science and Technology

Doctoral theses at NTNU, 2019:52

NTNU

Håkon Strandenes

Turbulent flow simulations at higher Reynolds numbers

Thesis for the degree of Philosophiae Doctor

Trondheim, February 2019

Norwegian University of Science and Technology
Faculty of Engineering
Department of MarineTechnology

NTNU
Norwegian University of
Science and Technology

NTNU
Norwegian University of Science and Technology

Thesis for the degree of Philosophiae Doctor

Faculty of Engineering
Department of MarineTechnology

ISBN 978-82-326-3708-9 (printed version)
ISBN 978-82-326-3709-6 (electronic version)
ISSN 1503-8181

Doctoral theses at NTNU, 2019:52

Printed by Skipnes Kommunikasjon as

Abstract

This thesis presents recent advancements in direct numerical simulations of bluff body wake flows. The flow around a circular cylinder without and with special fairings have been studied, and the effect of boundary conditions compared with what is used in physical experiments.

The flow around a 45° inclined 6:1 prolate spheroid have been studied for a broad range of Reynolds numbers ranging from 4000 to 16 000 based on the minor diameter of the spheroid. During this range of Reynolds numbers there is a transition from a steady, symmetric, laminar flow to a highly turbulent and asymmetric flow. Several interesting flow phenomena have been investigated in details.

In addition to the flow investigations the present thesis present developments in simulation tools and mesh design which were neccesary in order to conduct the largest simulations in this thesis, that is the inclined prolate spheroid at Reynolds number 16000. The grid used contained around 8.4 billion (10^9) grid cells.

Preface

This thesis discuss advancements in the simulations of bluff body wake flows at higher Reynolds numbers. Two wake flow cases have been studied: the flow around a circular cylinder with and without fairings and the flow past an inclined 6:1 prolate spheroid. During my work with this subject, I have submitted several research papers in various journals. These papers together will make the second part of this thesis. The first part will contain a small discussion on common computational methods and a summary of the most important results, as well as additional results that did not fit the scope of any of the published papers.

Attached papers

There are five papers attached to this thesis.

I **On the Effect of Boundary Conditions on the Flow around a Cylinder in a Channel**, Håkon Strandenes, Jose P. Gallardo, Bjørnar Pettersen, Helge I. Andersson. In: Proceedings of MekIT'15 Eighth National Conference on Computational Mechanics, International Center for Numerical Methods in Engineering, 2015, ISBN 97884944244-96

II **Influence of spanwise no-slip boundary conditions on the flow around a cylinder**, Håkon Strandenes, Bjørnar Pettersen, Helge I. Andersson, Michael Manhart. In: Computers & Fluids vol. 156, October 2017, pp. 48–57, DOI: 10.1016/j.compfluid.2017.06.025

III **Efficient and adaptive Cartesian mesh generation and flow initialization for DNS**, Håkon Strandenes, Fengjian Jiang, Florian Schwertfirm, Bjørnar Pettersen, Helge I. Andersson. Submitted to an international journal, September 2018.

IV **The near-wake of an inclined 6:1 spheroid at Reynolds number 4000**, Håkon Strandenes, Fengjian Jiang, Bjørnar Pettersen, Helge I. Andersson. Accepted for publication in AIAA Journal, December 2018, DOI: 10.2514/1.J057615

V **Low-Frequent Oscillations in Flow past an Inclined Prolate Spheroid**, Håkon Strandenes, Fengjian Jiang, Bjørnar Pettersen, Helge I. Andersson. Under review in International Journal of Heat and Fluid Flow, September 2018

Preprint versions of all papers can be found attached to this thesis.

Acknowledgements

During this work I have been heavily dependent on the computational resources provided by UNINETT Sigma2 under project *nn9191k*. Without these resources this research would not be possible to conduct. I highly appreciate the efforts to provide a computational infrastructure and support to Norwegian researchers.

In October 2015 I were offered five months employment in the Chair of Hydromechanics at the Technical University of Munich, Germany. The job was to work on improving the performance of the computational fluid dynamics code *MGLET*. This allowed me a unique insight into the code that I have benefited from in my later research at NTNU.

The help and support of the employees at *Kreuzinger and Manhart Turbulenz GmbH* on the MGLET code have also been invaluable. Their willingness to spend time on supporting and helping me and other users with problems we have been facing with the MGLET code, are unique.

My colleague Fengjian Jiang have given me a lot of ideas and our discussions have always been fruitful and inspiring. My supervisors, Professor Bjørnar Pettersen at the Department of Marine Technology and Professor Helge I. Andersson at the Department of Energy and Process Engineering also deserve honours. They have provided great support, motivation and ideas.

At last I would like to thank my wife Ida and my lovely daughters Ingeborg and Aurora. You have given me time, patience and perspective which I could not have been without.

Trondheim, February 2019, *Håkon Strandenes*

Contents

List of Figures

List of Tables

Nomenclature

Abbreviations

AUV	Autonomous Underwater Vehicle
CFD	Computational Fluid Dynamics
DNS	Direct Numerical Simulation
FVM	Finite Volume Method
LES	Large Eddy Simulation
PIV	Particle Image Velocimetry

RMS	Root-Mean-Square
VIV	Vortex induced vibrations

Greek Symbols

λ	Aspect ratio of spheroid $\lambda = L/D$
ν	Kinematic viscosity of fluid
ρ	Fluid density
Ω	Control volume

Roman symbols

C_p	Pressure coefficient $C_p = 0.5\rho U_\infty^2$
D	Diameter
f	Frequency
L	Length (generic - various definitions)
$\tilde{p}$	Kinematic pressure $\tilde{p} = p/\rho$
p	Pressure
Re_D	Reynolds number based on diameter $Re_D = DU_\infty/\nu$
Re_L	Reynolds number based on length $Re_L = LU_\infty/\nu$
S	Surface of control volume
T	Period (in time)
$\mathbf{U}$	Fluid velocity vector
$\overline{U}, \overline{V}, \overline{W}$	Mean fluid velocity
u'	Fluctuating part of velocity $u' = \overline{U} - u$
U_∞	Inflow velocity
Δx, Δy, Δz	Grid spacing

Chapter 1

Introduction

The physics of fluid flows are one of the cornerstones of many fields within science and engineering. The modern society would not exist if it weren't for the insight we have in the behaviour of fluids in motion. Everything from transportation, power generation, renewable energy harvesting to civil engineering builds upon knowledge on fluid dynamics.

One important class of fluid flow problems are the bluff body wake flows. These cases arise when a fluid passes by a bluff (non-streamlined) body. The resulting physical process is a complicated interaction between boundary layers, separation, shear layers, large-scale vortex dynamics and turbulence. In contrast to the traditional fields of turbulent flow analysis in which it is often assumed that the turbulence is both isotropic and homogeneous, in the case of wake flows neither is generally true. This makes it difficult to use traditional turbulence models, both in the boundary layers and in the far-field away from the body.

There are many bluff body wake challenges in the marine industry. One of the most important ones is the turbulent wake behind a cylinder. Within the oil and gas industry there are many critical cylindrical structures, such as pipes, risers, mooring lines, pipelines etc. This inspired the first part of the present work, which involved study of the circular cylinder with and without VIV-suppressing (Vortex Induced Vibrations) fairings.

Another flow problem is the wake behind a spheroid. The spheroid is a body of revolution, in which a 2-D ellipse is rotated around one of its two axes. If the ellipse is rotated around its shortest axis, as shown to the

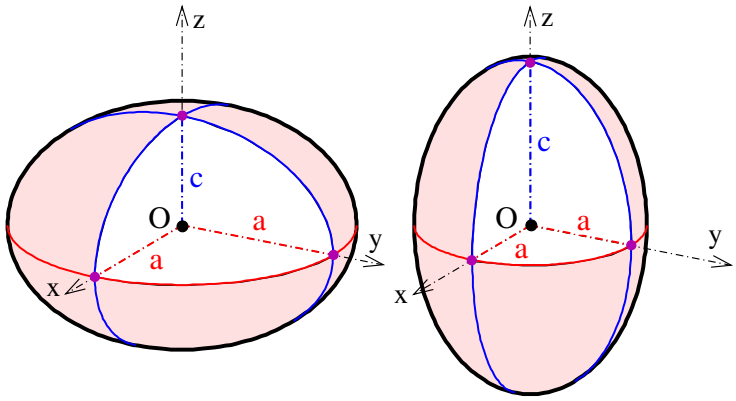

Figure 1.1: Oblate (to the left) and prolate (to the right) spheroids. The diameter D and length L are related to the semi-axes as $D = 2a$ and $L = 2c$. Illustration by Wikipedia user `Ag2gaeh`.

left in figure 1.1, the body is called an oblate spheroid. If the rotation is around the longest axis, we call it a prolate spheroid. The shape of the spheroid is given by a single aspect ratio $\lambda = L/D$ where L is the length of the axis of revolution ($L = 2c$ in figure 1.1) and D is the length of the two other axes ($D = 2a$ in figure 1.1).

The reason for the many studies on the prolate spheroid is that this geometrically simple object, whose shape is given only by the aspect ratio λ, can be a prototype for a variety of scale bodies ranging from microscopic particles (microplastic) to submarines, aircraft and drones. The bow shape of a submarine or the nose of an aircraft can easily be modelled as a part of a prolate spheroid. An example of such a vessel is shown in figure 1.2.

In the early days of science, 'complex' fluid flows were usually studied experimentally. Today we have another option which gets more appealing every day as the price of computational power drops: simulations. The present work is based on the results of Direct Numerical Simulations (DNS) and Large Eddy Simulations (LES) where we simulate the fluid motion down towards the smallest scales present in the problem, and resolve all the details therein. The advantages over various experimental approaches are the level of details one can extract from the problem, and the level of control one have over the boundary conditions of the problem.

Figure 1.2: Hugin 1000 AUV on board a ship. Illustration from Wikipedia under public domain.

Chapter 2

Simulation and modelling techniques

The present work is all about numerical simulations of turbulent flows. This chapter will briefly describe the simulation techniques used.

2.1 Fundamental equations

The fundamental equations for fluid flow are the Navier-Stokes equations for conservation of mass and momentum. In the present work we will assume that the flow is incompressible. This implies that the fluid density ρ is constant throughout the entire fluid volume and at all times. Since the finite volume method (FVM) have been used as the numerical tool, we present the governing equations on integral form, as given in [1]:

$$\begin{aligned}\frac{\partial}{\partial t}\int_\Omega \mathbf{U}\,\mathrm{d}\Omega + \int_S \mathbf{U}\mathbf{U}\cdot\mathbf{n}\,\mathrm{d}S = -\int_S \tilde{p}\,\mathbf{n}\,\mathrm{d}S + \\ \nu\int_S \left(\nabla\mathbf{U} + (\nabla\mathbf{U})^T\right)\cdot\mathbf{n}\,\mathrm{d}S\end{aligned} \tag{2.1}$$

which together with the equation for conservation of mass (which in incompressible flow is expressed as conservation of volume) give the basic mathematical foundation for the present work:

$$\int_S \mathbf{U}\cdot\mathbf{n}\,\mathrm{d}S = 0 \tag{2.2}$$

In both equations S is the surface of the control volume Ω.

The solution of equations 2.1 and 2.2 give the fluid velocity vector $\mathbf{U}$ and kinematic pressure $\tilde{p} = p/\rho$.

2.2 The Finite Volume Method

The finite volume method is a very appealing spatial discretization method for numerical solutions of the Navier-Stokes equations. The resulting set of discrete equations are conservative and simple to implement in practice. Since the governing equations are already formulated at an integral form, we can easily apply two steps:

1. Interpolate the relevant quantity (e.g. velocity, pressure) on to the surface of the grid cells

2. Integrate the quantity over the surface of the control volume

The result is the volume-averaged quantity (velocity, pressure) in each grid cell. A number of interpolation and integration schemes are developed for the different terms in equation 2.1 for various purposes. Usually, second order accuracy can be achieved with the finite volume method, however, there also exist schemes that give fourth order convergence rates.

2.3 Multi-Grid Large Eddy Turbulence - MGLET

In the present work, the CFD code *MGLET* have been used for all simulations. In short, MGLET uses a finite-volume formulation on staggered Cartesian grids, as shown in figure 2.1, to solve the incompressible Navier-Stokes equations. Simple linear interpolation and integration schemes are used for all spatial terms, hence leading to second-order accuracy in space. A third-order low-storage explicit Runge-Kutta time integration scheme [2] is used for time stepping. In combination, this gives high accuracy, very low numerical dissipation and high computational efficiency.

MGLET introduces the solid geometry through an immersed boundary method [3]. A local refinement of the grid in regions of interest is possible. The refinement process is a simple cell splitting, in which each parent grid cell subject to refinement is split into eight equal (3-D) child cells [4].

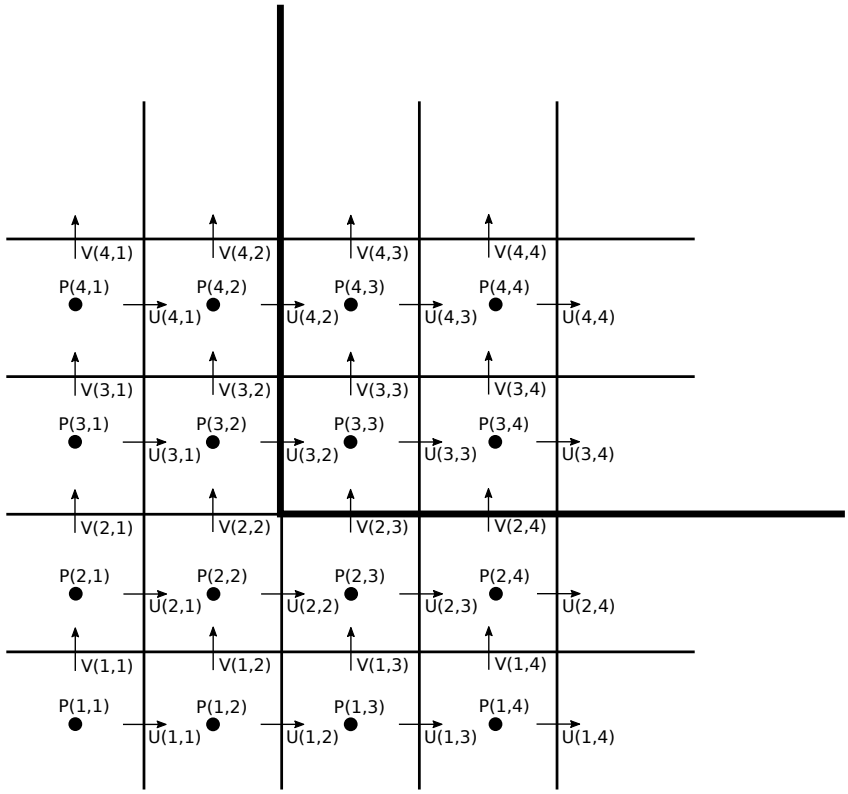

Figure 2.1: 2-D staggered grid illustration with numbering of cells as used in MGLET. The bold line indicate the exterior boundary of the computational grid.

The MGLET code was chosen for this work because of its proven record of producing successful high-quality direct numerical simulations, the appealing immersed boundary method, the parallel performance and scaling and the amount of flexibility and extendability this code gives with respect to implementing new customized features. As of today, we are not aware of any other similar computational tool that can provide the same list of computational benefits and physical features as MGLET for the kind of simulations presented here.

2.3.1 Mesh generation

Significant work have been conducted on the performance of the MGLET code and the simulation workflow. The mesh generation is a particularly important topic, since the computational mesh is the fundament for numerical simulations. It is widely accepted that without a good mesh, it is not possible to get high-quality results from a simulation.

The traditional grid structures used in DNS simulations are variations of structured grids with cuboid cells. In MGLET we use Cartesian grids, and the only way to control the density of the cells have traditionally been to vary the grid spacing (i.e. stretching) in the x, y and z-directions. This allow the user to cluster the cells around objects of interest. Figure 2.2 shows an example of such a mesh strategy around a circular cylinder.

The disadvantage with the classic grid stretching technique is that a lot of cells are wasted in areas of no interest, and that cells with very high aspect ratios are generated. Figure 2.2 illustrate this in the example of a mesh around a circular cylinder. The red highlighted areas in this figure contain lots of cells with high aspect ratio. In addition, the regions **a** and **b** are areas with no significant flow features or gradients that needs to be refined, and the cells here are thus completely wasted. The region **c** does indeed contain the wake, but the results from this region cannot be trusted due to the high aspect ratio of the grid cells. The resolution here is effectively limited by the longest side of the grid cells. In this region **c** that is Δx. A smaller grid spacing in other directions cannot compensate for the lack of resolution in the streamwise direction.

With the above mentioned limitations in mind we have implemented a new meshing technique for DNS simulations in MGLET. The new 'integrated mesh generation and flow initialization' method combine multiple

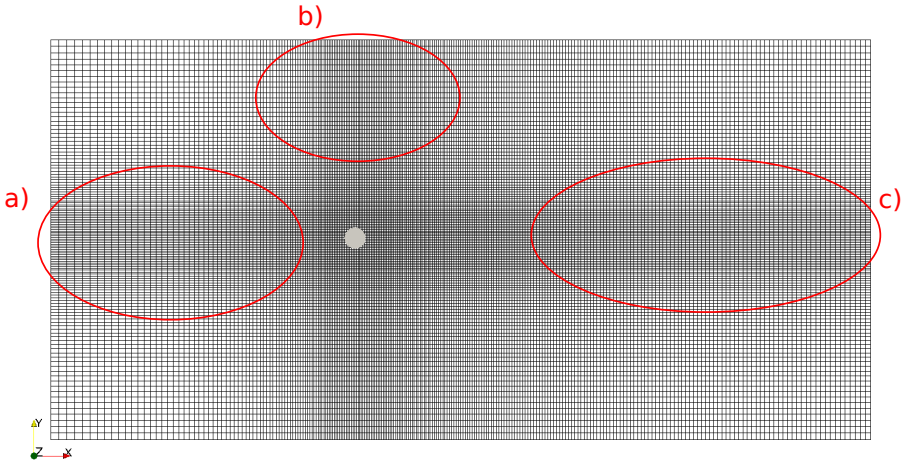

Figure 2.2: Traditional Cartesian mesh around a circular cylinder. The marked red regions are regions with lots of wasted grid cells. In the areas **a** and **b**, the cells are not needed because there are no interesting flow features in these regions. In region **c** the cells have a very high aspect ratio because the grid spacing in the streamwise direction Δx is much larger than the grid spacing in the crossflow direction Δy, which deteriorate the accuracy of the flow solution.

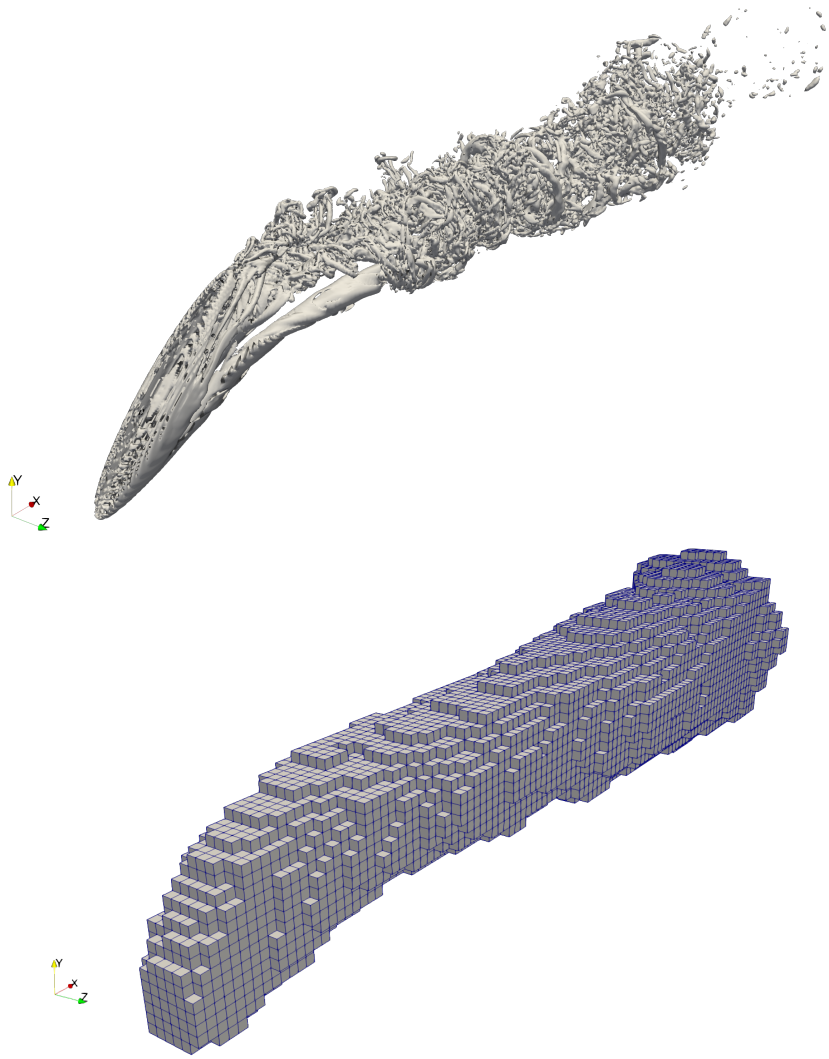

Figure 2.3: Isocontour of $\lambda_2 = -1.0$ for the flow around a 45° inclined prolate spheroid (top) and assiciated grid structure (bottom). Grid boxes with 40^3 grid cells in each box created by the improved meshing technique. The arrangement of grid boxes are automatically adapted to the flow. Only a selected grid level is shown, there are both larger (coarser grid resolution) and smaller (finer grid resolution) boxes in the domain.

individual Cartesian grid boxes in a hierarchical structure with a refinement criterion, allowing arbitrary locally refined meshes in complex regions, see figure 2.3. When initiating the flow, we start out with a few coarse grid boxes and as the flow evolves, we insert more and more grid boxes until necessary resolution in all critical flow regions are achieved. The result of the method is both a flow field we can use as initial condition for further statistical sampling and a computational mesh that resolve all flow structures down to the smallest details.

The advantage of the method is a more precise and efficient mesh generation, significantly less total number of cells and by that a better utilization of the available computational resources. Compared to a traditional Cartesian mesh used today we document savings in computational time of around 80% compared to using traditional single-block Cartesian grids.

The details of this new method can be found in the attached paper III.

2.3.2 Performance improvements

The MGLET code itself have been subject to heavy improvements during the present thesis work. It was motivated by the need and desire to simulate increasingly higher Reynolds numbers with more grid cells than ever before. The original parallelization strategies within MGLET dated back to the mid 1990's, in which the computer systems and capabilities were significantly different from today. The new work started in 2015 as a joint effort between the *Technical University of Munich* (TUM), *Norwegian University of Science and Technology* (NTNU) and *Kreuzinger und Manhart Turbulenz GmbH*, along with the respective supercomputing organizations in Munich and Trondheim, the *Leibniz Rechenzentrum* (LRZ) and *Uninett Sigma2*. This have given enormous improvements in performance and upscaling. In addition we now have a completely redesigned IO format capable of handling meshes with billions (10^9) of grid cells with good performance. Figure 2.4 gives an indication of the development of the performance over time, from the initial work started in 2015 until recently. As the figure shows, in 2015, depending on the case, it was difficult to utilize more than 1000 processes on the computer efficiently, while the current status is that more than 10 000 processes can be used with very little scaling overhead. In addition to the improved scaling (the slope of the lines in figure 2.4), we have also managed to improve the baseline performance, which means

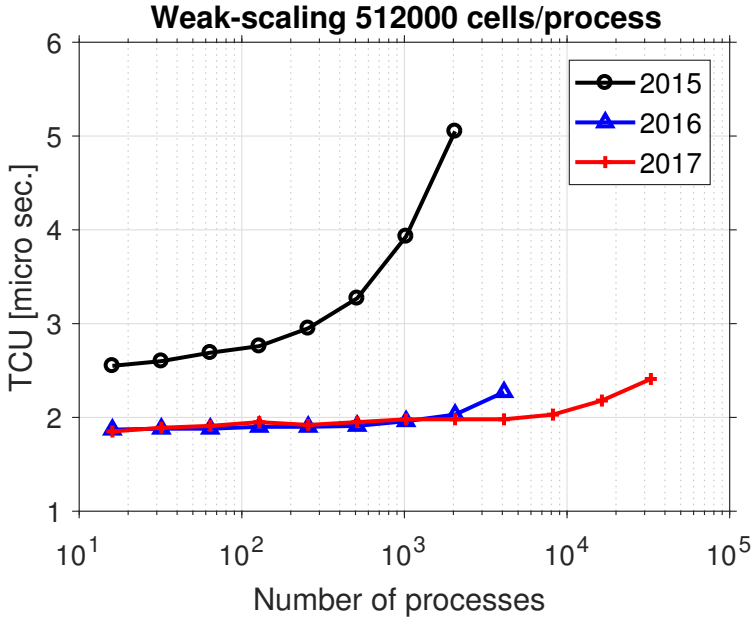

Figure 2.4: MGLET scaling and performance improvements over time. TCU is the number of microseconds of CPU-time required to integrate a single grid cell one time step forwards. The figure is produced by *Yoshiyuki Sakai* at TUM.

that we can put more effort (grid cells) per processor than before and still achieve the same overall run-time of the simulations.

Without this enormous collaborative effort, including funding for more than a year of development work, the simulations presented in this thesis would not have been possible to conduct at all. More details of this work can be found in [5].

Chapter 3

The flow around a cylinder with and without fairings

The flow around a circular cylinder with uniform inflow conditions is among the most widely studied external flow cases in the literature. Besides the engineering importance, it is appealing because the problem is easily formulated with just one parameter, the Reynolds number, and there is access to a wide range of reference data from both numerical simulations and laboratory experiments.

The engineering importance of the flow around a cylinder is often related to the forces acting on the structure. Because of the vortex shedding the forces oscillate, and this can lead to multiple structural challenges such as material fatigue and resonance. Whenever a structure starts oscillating because of excitation from vortex shedding, we call this phenomena vortex induced vibrations (VIV). Problems related to VIV often require extensive studies, and this is why the study of VIV and various mitigation techniques (e.g. strakes or fairings) are important.

3.1 The flow around a cylinder with fairings

In this chapter we will present work and results that shows our simulation tools and methpodology can:

- Simulate and replicate the results of an experiment

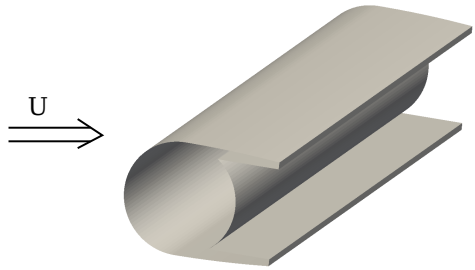

Figure 3.1: Circular cylinder with special fairings to reduce the oscillating forces from the vortex shedding process and the associated vortex induced motions acting on marine risers.

- Produce and evaluate results from both LES and DNS at these Reynolds numbers
- Verify the usability of varying locally refined grids/embedded grids

The above points will be demonstrated with the flow around a cylinder with special VIV-mitigating fairings, as shown in figure 3.1. The choice of a cylinder with fairings was motivated by the fact that we were given access to data from laboratory experiments, which allowed us to compare the simulation results with experimental data.

This advances previous works along multiple axes. First, simulating the results of an experiment are sometimes difficult, which were the main topic of the following work(s). Second, there are in the literature a lot of references using LES models to simulate the flow around a circular cylinder at Reynolds number $Re = 3900$, however, since most of these references are somewhat old, they could never afford to do a fully resolved DNS as well for reference. This is provided here. Third, we wanted more flexibility in the mesh generation process in the future to be able to increase the Reynolds number without using an excessive amount of grid cells. Therefore we decided to conduct the LES simulations with local grid refinement in addition to the traditional stretching techniques to learn and demonstrate that this also compared well with DNS results.

The first attached paper I [6] of the present thesis originated from an attempt to explain the differences in the results from a DNS simulation and a set of experiments with flow around a circular cylinder equipped with

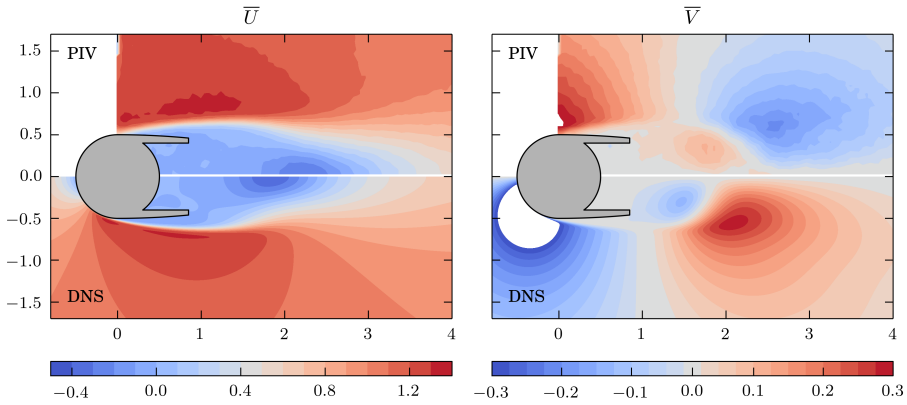

Figure 3.2: Illustration of the discrepancy between PIV experiments and DNS simulations at $Re = 5000$, illustrated by the mean streamwise ($\overline{U}$) and crossflow ($\overline{V}$) velocities. White regions are either outside the color scale or outside the dataset (relevant for PIV only).

special VIV-supressing fairings (fig. 3.1). This difference was first reported in [7]. There we compared a DNS using MGLET, a LES using OpenFOAM and results from a PIV experiment done in the *Circulating Water Tunnel* at the *Marine Technology Center* in Trondheim, all at Reynolds number 5000. In summary, neither of the results were comparable with each other. Figure 3.2 compare the DNS with the PIV, and shows the huge differences between these two datasets. Needless to say, this was a challenge and we got motivated to investigate why this happened.

The first step to solve the issue was to provide high-qulaity LES results that would match the DNS results, in order to reduce the requied computational effort of the various simulations that was requied. With MGLET's LES models and local grid refinement techniques [4], we got results that was close to the DNS data with the same boundary conditions. When this was achieved, we applied **the exact same boundary conditions** as used in the experiment, which is no-slip boundary conditions on the spanwise ends of the cylinder. When we did this, we could see that the results from the experiment was very close to that of the LES with the correct boundary conditions. The results of these simulations were presented in [6].

Figure 3.3 summarize the differences between this set of simulations and

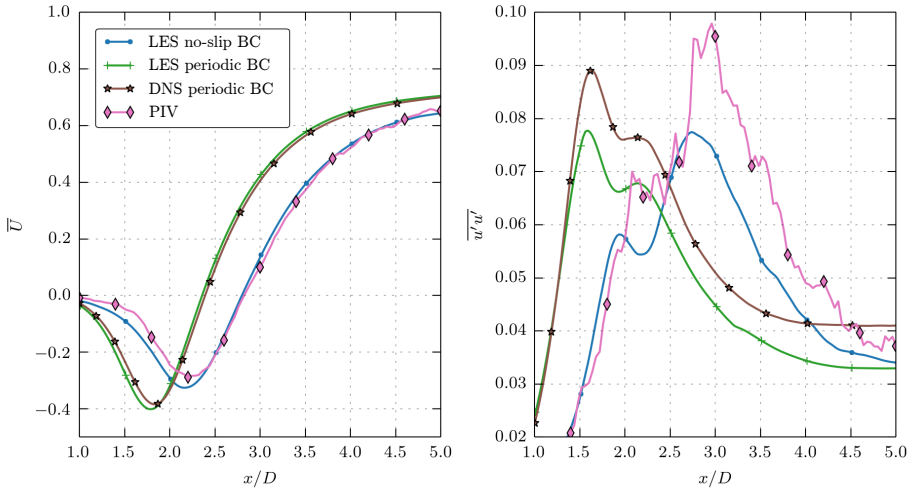

Figure 3.3: Mean streamwive velocity $\overline{U}$ and variance $\overline{u'u'}$ in the centerline behind the cylinder. Comparing LES with no-slip boundary conditions (blue), LES with cyclic boundary conditions (green) DNS (red) and PIV (pink).

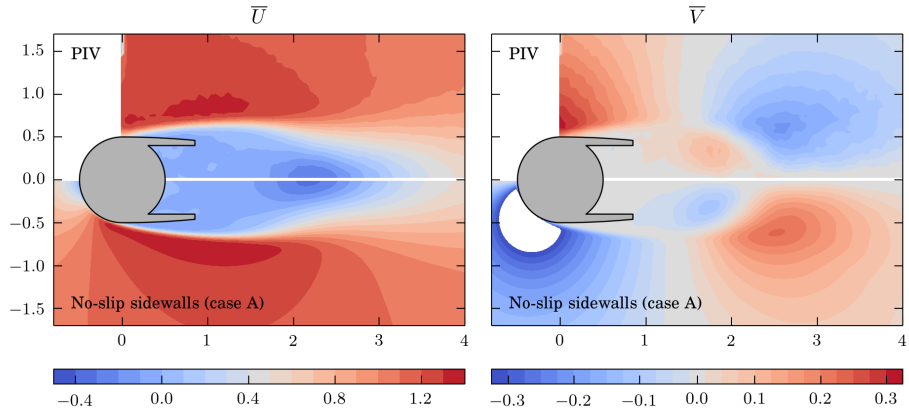

Figure 3.4: Illustration of the good agreement between PIV and LES when the correct no-slip boundary condition is applied to the simulation. Mean streamwise ($\overline{U}$) and crossflow ($\overline{V}$) velocities. The upper half of the figures ($y > 0$) are the results from the PIV and the lower half ($y < 0$) shows the results of the LES. Notice that the crossflow velocity is antisymmetric about the y axis.

experiments. There is a near perfect agreement between the LES and DNS in the mean flow field, given that we use the same boundary conditions. Similarly, there is also a near perfect agreement between the LES and PIV experiment given that we in the LES simulation apply the same boundary conditions as in the experiment. Figure 3.4 shows the detailed comparison between PIV and the LES with no-slip sidewalls to illustrate the good agreement between this simulation and experiment. It is evident that the physical no-slip sides in the PIV experiment leads to a strong influence on the flow field, even in the middle of the experimental cross section where the PIV measurement plane is located, $6D$ from either sidewall (the cylinder is $12D$ long).

In figure 3.5 we compare the periodic boundary condition with the no-slip boundary condition. It illustrates how the shear layers, vortex shedding and recirculation region is influenced by the difference in boundary conditions. In these figures, attention should be drawn to the significantly longer recirculation region (shown in *a)*) and lower level of velocity fluctuations (shown in *b)*) in in the case with no-slip sidewalls compared to the case with periodic sidewalls. The streamlines of the average flow field, shown in the rightmost plot in *c)*, also shows that there are no regions in this case where the average flow field is un-affected by the sidewalls. Significant components of spanwise velocities are observed over the entire span. Further details on the flow around the cylinder with fairings can be found in the attached paper I.

3.2 The flow around a circular cylinder

Based on the results from the simulations of the cylinder with fairings, we became inspired to extend the results to a more universally used Reynolds number and a bare cylinder geometry. Therefore we decided to repeat the computations with a circular cylinder at $Re = 3900$, the most used Reynolds number for this case. We also included multiple cylinder lengths from $6D$ to $24D$ to be able to discuss the length necessary in experimental setups like the previously described PIV case.

The results were published in [8] (attached paper II). The overall conclusions were the same as in the case with the cylinder with fairings at $Re = 5000$. The no-slip boundary condition severely influence the wake

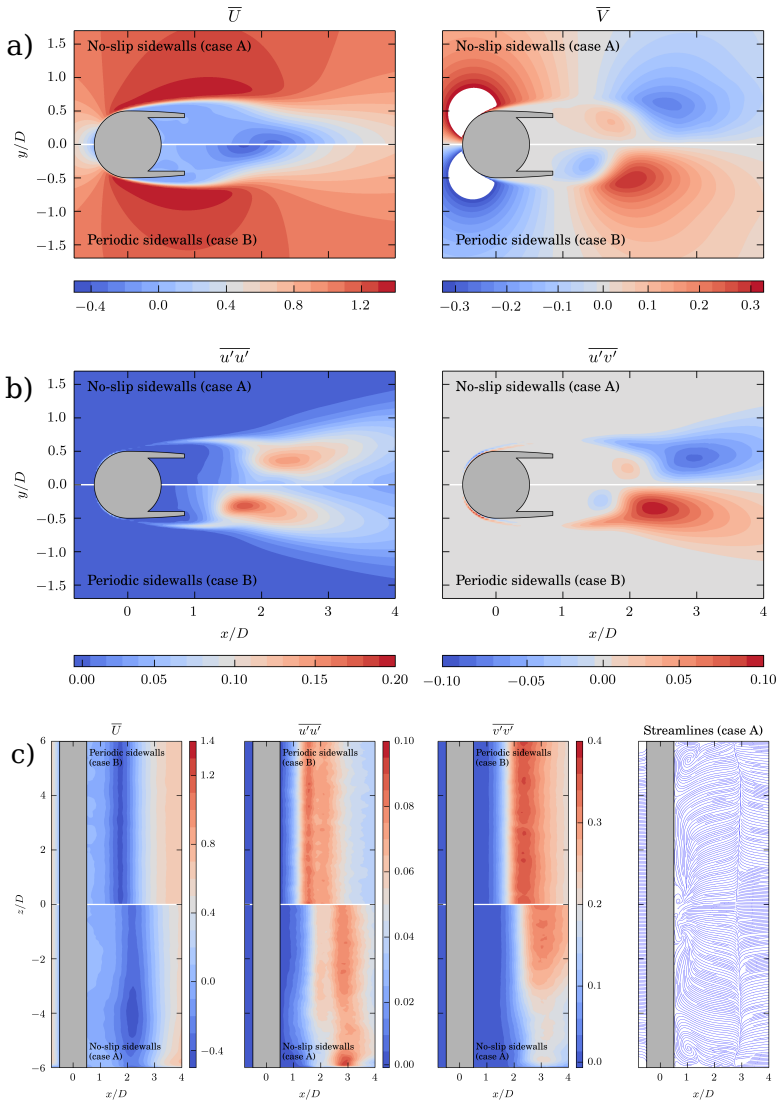

Figure 3.5: Mean streamwise $\overline{U}$ and spanwise $\overline{V}$ velocity (panel a), two Reynolds stress componens ($\overline{u'u'}$ and $\overline{u'v'}$, panel b) for periodic (lower half) and no-slip (upper half) boundary conditions. Cylinder length is $12D$. $\overline{V}$ and $\overline{u'v'}$ are antisymmetric.

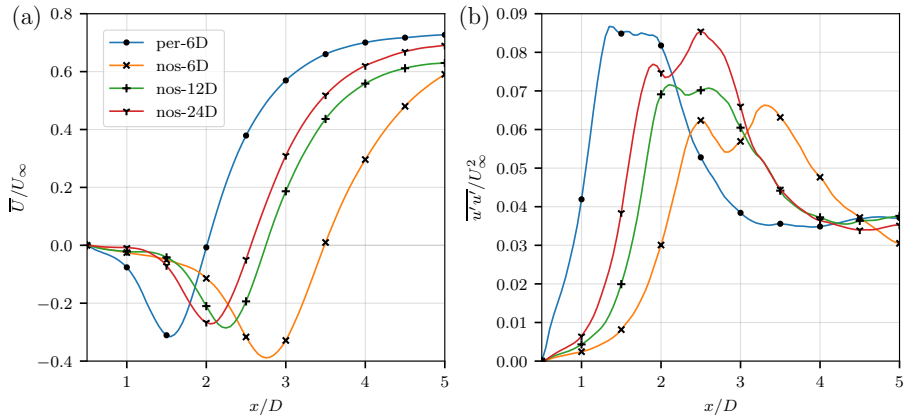

Figure 3.6: Flow profile in the symmetry plane behind the circular cylinder for the case with periodic conditions (label *per-6D*) and no-slip sidewalls with length from $6D$ (label *nos-6D*) to $24D$ (label *nos-24D*).

properties even for very long cylinders ($24D$ long), and no single sampling plane in the experimental tank are representative for the flow we observe around 'infinitely long' cylinders. The relatively small difference seen in for example figure 3.6 when increasing the length of the cylinder from $12D$ to $24D$ also indicate that no small increase in length will mitigate the issue. Without any proof it can be speculated if a length of more than $100D$ might be necessary to represent an 'infinitely long' cylinder given that you use no-slip boundary conditions.

In addition to confirming the validity of the previously conducted simulations of the cylinder with fairings, we also documented that the shear layer instability discussed in [9] was suppressed by the no-slip boundary conditions. This underlines the point that the flow is severely affected by the no-slip boundary conditions.

The overall results deliver an important message: when doing experiments in tanks and flumes like the Circulating Water Tunnel or various cavitation tunnels, one should be aware of the effects of boundary conditions on the flow in question. Due to the needs of free view for the PIV cameras, end-plates, which is often used in other kinds of experiments [10], cannot normally be used, because it would obscure the view of the cameras in

conventional PIV setups. However, with the stereoscopic PIV techniques it is possible to position the cameras at an angle, typically from behind. This will allow moderately sized end-plates to be fitted given a sufficiently long cylinder. However, even though end-plates on short cylinders give similar forces as those found on long cylinders, this is no guarantee that the flow field is not influenced by the end-plates as well!

Chapter 4

The inclined 6:1 prolate spheroid

The flow around the 45° inclined $\lambda = L/D = 6:1$ prolate spheroid have been subject to the toughest investigation among the cases in this thesis. This case was previously studied with DNS up to the Reynolds number $Re_D = 3000$ [11, 12], and for a 90° inclination (crossflow), the highest Reynolds number simulated was $Re_D = 10000$ [13].

At lower angles of attack ($\leq 20°$) and higher Reynolds numbers ($\mathcal{O}(Re_L) \leq 10^6$) the 6:1 prolate spheroid have also been subject to numerous experiments, see for example references [14, 15, 16]. Attention have also been given to the manoeuvring capabilities of the 6:1 prolate spheroid [17, 18]. These experiments underline the engineering importance and the similarity to various vessels in the air and ocean.

The particular interest in the spheroid comes from the many flow features that can be observed in the flow around it. The cross-section of the body is shown in figure 4.1, and gives an impression of the geometry. The nose is in fact very sharp, with a radius curvature of only $0.083D$, giving it similarities to both sharp-nosed bodies and blunt-nosed bodies.

In the present work we started by analysing previously studied cases at 45° inclination angle [11, 12], that is $Re \leq 3000$, and then continued to simulate cases with higher Reynolds numbers (4000, 8000, 16000). The domain is the same in all of the cases, and similar to the one used previously at Reynolds number 3000. An overview of the domain and axis system is

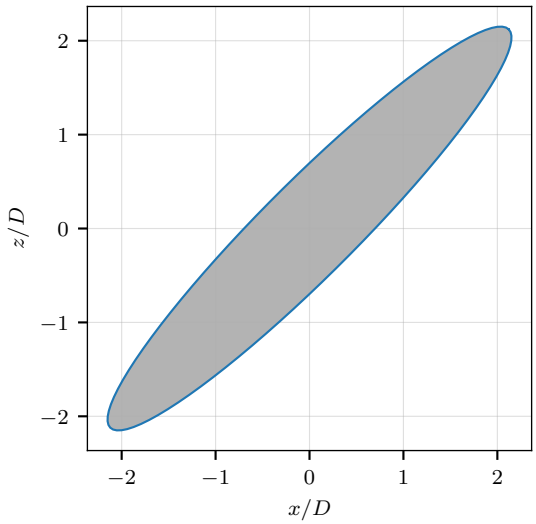

Figure 4.1: Cross-section through the 45° inclined 6:1 prolate spheroid.

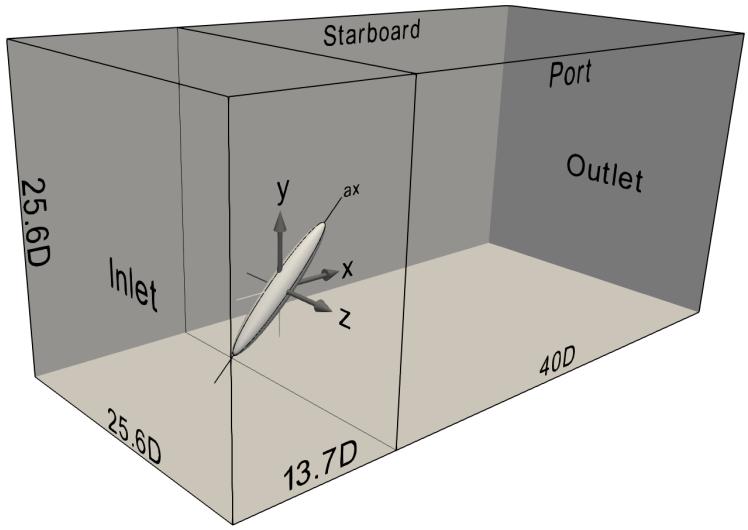

Figure 4.2: Computational domain and coordinate system definitions used in the simulation of the inclined prolate spheroid.

shown in figure 4.2. To facilitate easy discussions we choose to adopt the (aero)nautical terms *port* and *starboard* to distinguish the two sides of the spheroid. The port side is to the left when the observer is positioned at the spheroid and looking toward the oncoming flow. In mathematical notation, the port side is the half of the spheroid with $z > 0$ and the starboard side is the half of the spheroid with $z < 0$, see figure 4.2.

The results for the case at $Re_D = 16000$ in chapter 4.4 should be considered preliminary because of insufficient simulation time. This was because an unexpected bug in the computer system *Fram* suddenly occurred and interrupted our simulations. However, there is still a lot of useful information to extract from instantaneous snapshots in this case, as shown in 4.4.

4.1 Reynolds number 3000 and below

The flow at Reynolds number 3000 and below were already thoroughly investigated by others [11, 12, 19]. However, because of the improvements in the simulation strategies, modifications and improvements to the code that was conducted in the period between the previous and the present work (see chapter 2), we felt that it was necessary to replicate older results to make sure that the new simulation strategies and tools still produced the same high quality data.

Based on the new possibilities in efficient mesh generation we decided to refine the mesh in the far wake behind the spheroid. We constructed a mesh with a resolution near the wall that was slightly finer than the original simulations by Jiang et al. [11], and with very much finer resolution far behind the spheroid. In summary, we concluded that:

- At Reynolds number 800, the wake is symmetric and stable, as earlier works concluded.

- At Reynolds number 1000, we found a significantly asymmetric wake. This is in agreement with the results in [19]. However, we also found significant and strong regular oscillations in the velocities far behind the spheroid. This was probably captured due to the finer grid resolution. The amplitude of these oscillations were in the order of magnitude $0.1U_\infty$. This was never reported earlier. In previous works

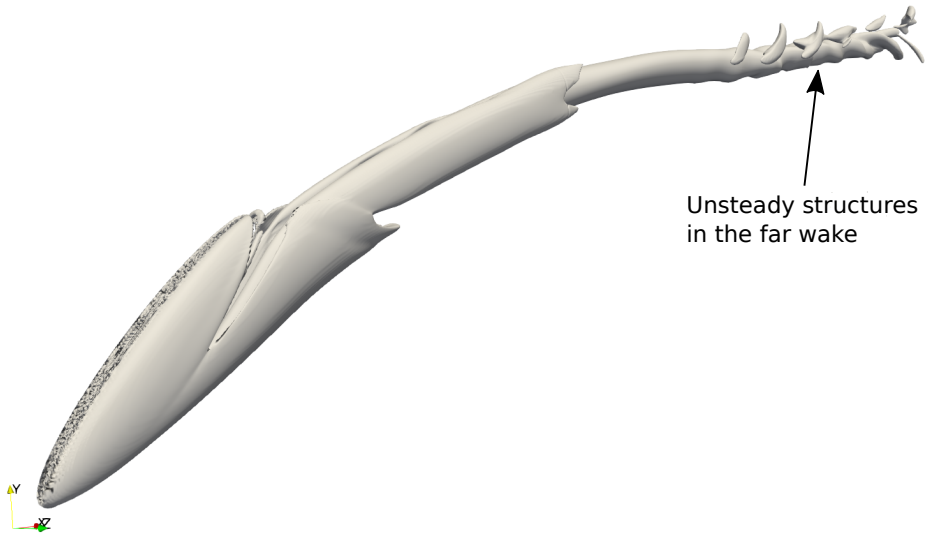

Figure 4.3: Wake at $Re_D = 1000$ shown by isocontours of the λ_2 vortex identification criterion [20]. In the far wake the flow is unsteady.

this Reynolds number was always described to yield a stationary flow. Because of this, the far wake topology differs clearly from previous works. See figure 4.3.

- At Reynolds number 1200, the point of transition from a steady to an unsteady wake has shifted closer towards the spheroid, and is now at about $x/D = 10$. The over-all pattern of the wake topology is according to the previous works. At this Reynolds number the average side-force is non-zero, which was not discovered in the original simulations. Although the amplitude is small (around 1% of the drag force), the result is significant and indicate that the entire wake, also the near-wall region, is asymmetric.

- At Reynolds number 2000, the entire wake is asymmetric and unstable. The average sideforce is significantly, about 20% of the drag-force. The drag- and lift-force exhibits intermittent high-frequent oscillations, and the sideforce oscillate irregularly with long periods. The intermittent high-frequent oscillations in the drag- and lift-forces are

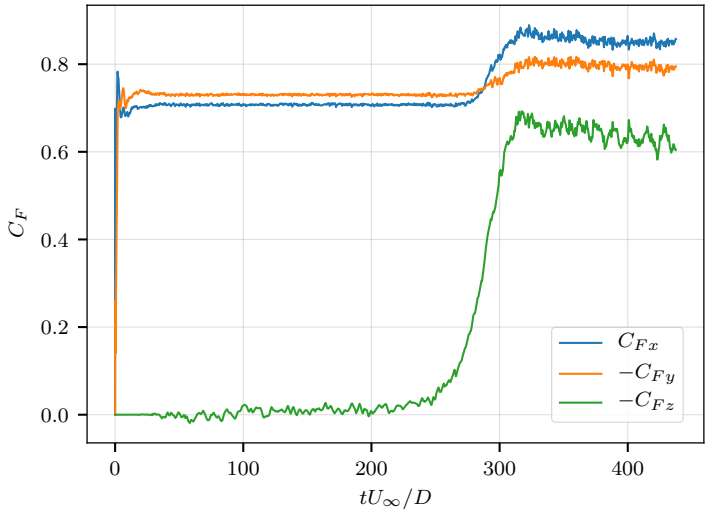

Figure 4.4: Development of forces on the spheroid at Reynolds number 3000. The key message here is that more than 300 000 timesteps were needed until the flow reached a fully developed state.

not reported before.

- At Reynolds number 3000 the overall wake structures found in the new simulation were qualitatively similar to those previously reported, see figure 4.4.

A side-note to the last point above is that the number of timesteps to create a fully developed flow field increase with increasing Reynolds number. This was particularly problematic at Reynolds number 3000, in which more tham 300 000 timesteps were needed to reach a fully developed flow state, as shown in figure 4.4. This means that the computational time required to reach a fully developed state is comparable to the computational time used for statistical sampling, which is highly unusual. This is the reason why the new combined grid generation and flow initialization method (as presented in chapter 2) were developed.

4.2 Reynolds number 4000

After the initial simulations at lower Reynolds numbers ($Re_D \leq 3000$) we decided to search for new flow features and phenomena at higher Reynolds numbers. Based on our insight in the development of the flow up to $Re_D = 3000$ we suspected that we were in a highly transitional region in which the flow rapidly changed with increasing Reynolds number. In addition, the intermediate regime in between Reynolds number 3000 (previous limit of simulations) and 10^6 (typical experimental Reynolds number) is not explored at all. With the new and improved preprocessing and simulation tools available we could simulate significantly higher Reynolds numbers, which triggered us to conduct more simulations on this geometry at higher Reynolds numbers.

At first glance, the flow at Reynolds number 4000 seemed to be quite similar to that of Reynolds number 3000. However, several new flow phenomena were discovered, which will be summarized briefly in this thesis. For the in-depth analysis and details, please refer to the attached article IV.

4.2.1 Backflow

A region of unexpected backflow was discovered on starboard side of the forward part of the spheroid, see figure 4.5. This have never been observed or reported by anyone earlier. The fluid enters this region from the opposite side of the spheroid nose, but close the center of the spheroid, the fluid turns around, and flows towards the front tip. Before it reach the tip, it is attracted by the nearby vortex, and transported downstream in the wake.

We have deliberately labelled this region the 'backflow' region, because unlike for example the recirculation region behind a cylinder, the fluid is continuously exchanged, fluid is not trapped inside this region. This can be proven by looking at the streamlines generated from the average flow field, in which streamlines enter and leave this area, as shown in figure 4.5.

So far no obvious explanation of the backflow regions have been found. However, speculations about the cause could for instance lead us to believe that there are high pressure gradients in the direction of the spheroid axis which lead to a separation of the upwards jet flow, which then flows back towards the tip.

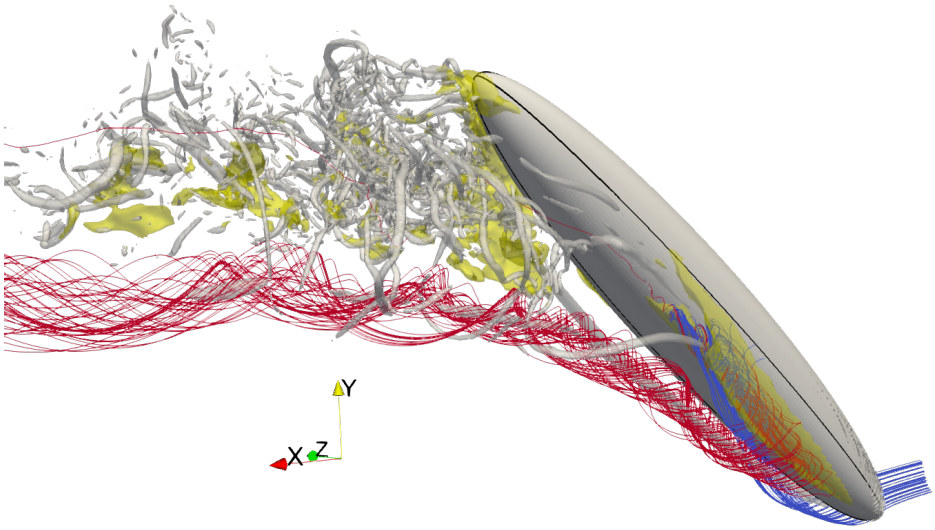

Figure 4.5: 3-D perspective view of starboard side at $Re_D = 4000$. Regions with backflow ($u_{ax} < 0$) are enclosed in yellow. The spheroid body and vortex cores (here defined by $\lambda_2 < -80$) are both grey. The streamlines are integrated from randomly selected seed points in the backflow region, both upstream and downstream. The lines from the backflow region and upstream towards the inflow, are blue, and the lines exiting and moving downstream and into the wake, are red.

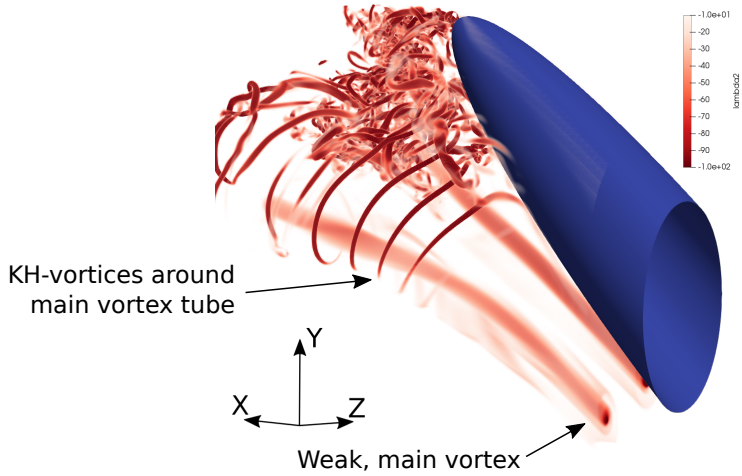

Figure 4.6: Kelvin-Helmholtz vortices around starboard vortex at $Re_D = 4000$ visualized by the λ_2 vortex identification criterion.

4.2.2 Kelvin-Helmholtz vortices

Another interesting phenomena is a sequence of Kelvin-Helmholtz vortices formed as rings around the weakest of the two main vortices, see figure 4.6. The special characteristics about these vortices, are that they rotate in a counter-intuitive direction. Normally for these kind of vortices, the freestream is the high-velocity driving side of the flow, and the wake region is the low-velocity side. However, in this case the weak vortex tube acts like a jet and drives the Kelvin-Helmholtz vortices with a significantly higher velocity than the freestream.

We only observe these vortices very intermittently. During a simulation with duration $30D/U_\infty$ we count around five vortices occurring in two 'bursts' (time intervals). The observations are not repeated later. When the Reynolds number is increased to $Re_D = 8000$ (chapter 4.3), these vortices are no longer intermittent, they become a permanent phenomena occurring around one of the vortex cores.

4.2.3 Wall shear stress calculations

One of the big disadvantages with the ghost-cell immersed boundary methods is that the solid prolate spheroid body surface is not properly defined. The solver only knows whether a grid cell is inside the body, near the boundary or completely outside. This makes it very difficult to compute the wall shear stress precisely. However, there is a new immersed boundary method developed for MGLET as well, in which the intersection of the body with the geometry is treated by accurately modifying the control volumes (cutting) to the desired body shape [21]. These methods are often called *cut-cell immersed boundary methods*.

The disadvantage with the cut-cell immersed boundary methods is that they are computationally significantly more expensive than traditional ghost-cell methods. Still, we managed to compute the instantaneous wall-shear stress distribution of the present $Re_D = 4000$ case using this method. The result is shown in figure 4.7 for both sides of the spheroid. The backflow feature can be clearly seen on the left (starboard) half, and clear differences between the two sides can be seen by closer examination.

This is an evolution in the simulation strategy and tools that will lead to more value for the invested simulation effort. Wall shear stresses are often important quantities that are requested, because they are vital in turbulence and wall modelling at high Reynolds numbers, for both RANS and LES applications. When we now can provide the wall shear stress from an immersed boundary code this will make our results more applicable as references or validation to other users of other codes. Additionally, we can use the exact wall treatment to model the boundary layers in LES simulations with well-known wall-functions, which makes it possible to conduct simulations of even higher Reynolds numbers where the boundary layers are impossible to resolve. Previously this was only possible to do with unstructured body-fitted mesh codes.

4.3 Reynolds number 8000

At Reynolds number 8000 the flow is significantly different from the flow at Reynolds numbers 3000 and 4000. The near wake flow is now nearly completely dominated by smaller, turbulent structures, and only parts of

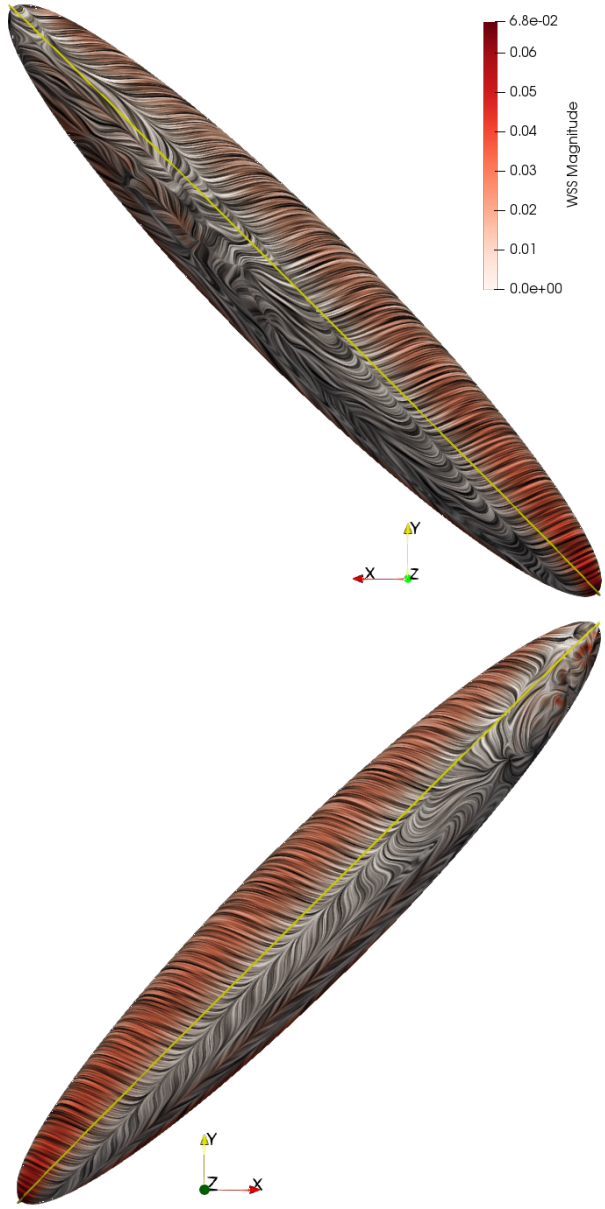

Figure 4.7: Wall shear stress lines on the spheroid, coloured by magnitude of the shear stress. Starboard side on top, port side below.

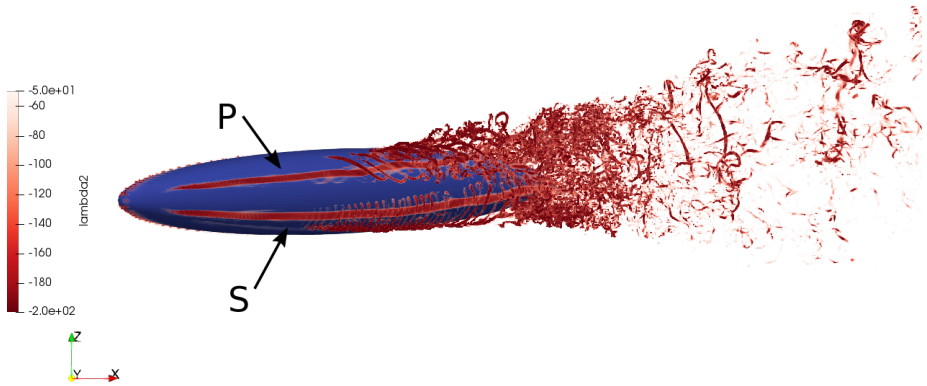

Figure 4.8: Flow structures near spheroid at Reynolds number 8000. Notice the Kelvin-Helmholtz vortices around the vortex S slightly to the right of the arrow. Visualization by isosurfaces of λ_2.

the larger coherent structures that dominate the lower Reynolds numbers remain.

Besides the more turbulent nature of the flow, the main vortices are significantly altered. For lower Reynolds numbers, the *weak* vortex was the long, persistent coherent structure, and the *strong* vortex was the one that was disintegrating into smaller structures first around the rear tail of the spheroid. At Reynolds number 8000, the **strong** vortex, S (starboard) in figure 4.8, persist as a coherent structure further downstream compared to the weak one P (port), although the point where the two vortices disintegrate is now significantly closer to each other. Neither of the vortices survive as coherent structures past the tail of the spheroid.

The Kelvin-Helmholtz vortices that we briefly observed at $Re_D = 4000$, are now permanently present as a continuous, repeating process with fixed frequency around vortex S in figure 4.8.

4.3.1 Low-frequent oscillations of the forces

The most new dominant feature at Reynolds number 8000 that catches our immediate attention is the massive oscillations in the forces acting on the spheroid, as shown in figure 4.9.

The period of these low-frequent oscillations are almost exactly $T =$

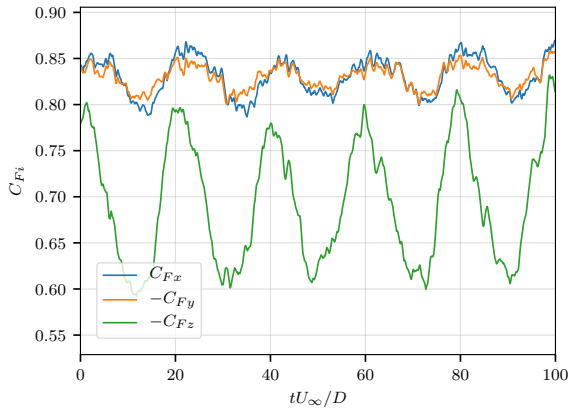

Figure 4.9: Drag and sideways force coefficient at Reynolds number 8000 for the first 100 U_∞/D simulated.

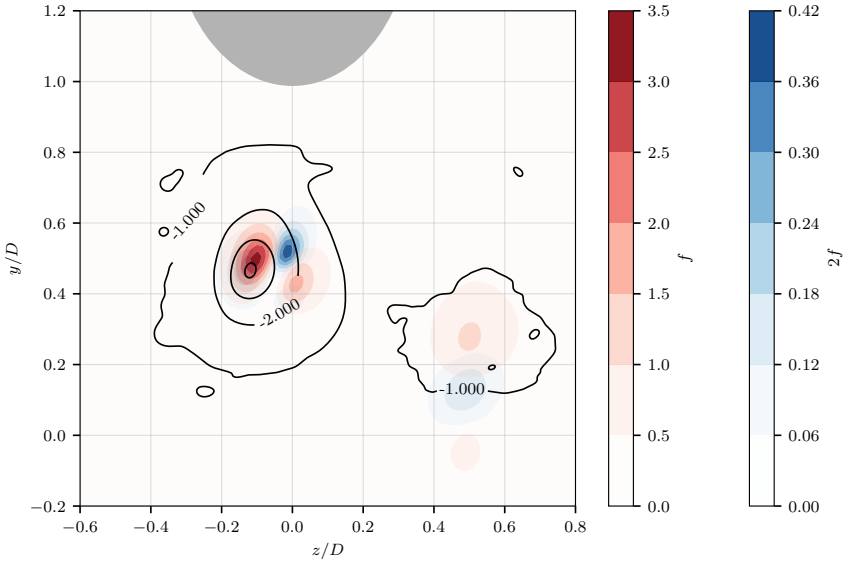

Figure 4.10: Fourier amplitudes of the pressure in a plane at $x/D = 1.55$ for the frequency corresponding to the low-frequent oscillations in the forces $f = 1/20\, DU_\infty$ (red colors) and the double of this frequency $2f = 2/20\, DU_\infty$ (blue colors). The pressure coefficient $C_p = p/(0.5\rho U_\infty^2)$ from a randomly selected timestep is drawn with black iso-contours.

$1/f = 20U_\infty/D$, leading to a Strouhal number of $St = fD/U_\infty = 0.05$. Compared to for instance a typically vortex street behind a circular cylinder at similar Reynolds number with Strouhal number of $St = 0.2$, the present process is very slow. We notice from figure 4.9, that the peak-to-peak amplitude of the side force (C_{Fz}) oscillations are more than **25 percent** of its mean value, revealing very strong flow dynamics in the wake that heavily influences the near pressure field. However, by inspection of the velocity field in the wake, we cannot find any signs of vortex shedding, and the presence of a von Karman vortex street can be ruled out. There are by traditional inspection mechanisms (visualization in 2-D and 3-D of quantities such as velocity, pressure, vorticity, λ_2 etc.) no obvious other structures that can be attributed to this phenomena either.

Figure 4.10 shows a Fourier analysis of the frequency components $f = 1/20\,DU_\infty$ (red) and $2f = 2/20\,DU_\infty$ (blue). The pattern can easily be explained: there is a cyclic motion of the two main wake vortices. The strongest vortex, which is located to the left in figure 4.10, move from the leftmost red area (where it is strong), passing through the blue area (where it gets weaker or the path is more uncertain), and towards the next red area again, before it moves back towards the origin at the leftmost red area following the same path. The vortex passes through the blue area to the left twice per cycle, hence the double frequency. The pattern of this motion is an upside-down 'U'-pattern.

Further details on this can be found in [22] (attached paper V).

4.3.2 Comparing Reynolds number 3000, 4000 and 8000

At first glance, the flow around the 45° inclined prolate spheroid at Reynolds numbers 3000, 4000 and 8000 appears to be quite similar to each other. However, closer investigation reveal that this is not the case. Figure 4.11 show the pressure in the vortex cores at different Reynolds numbers. The characteristic helical vortex alteration process leads to the two distinct minimas in the weak vortex at $Re_D = 3000$, while this is just barely visible at $Re_D = 4000$. A further increase in Reynolds number to $Re_D = 8000$ gives a completely different pressure distribution, with just one distinct global pressure minima. At the same time the strong vortex core have grown significantly stronger, with a very low C_p in the core of the strongest vortex at $Re_D = 8000$.

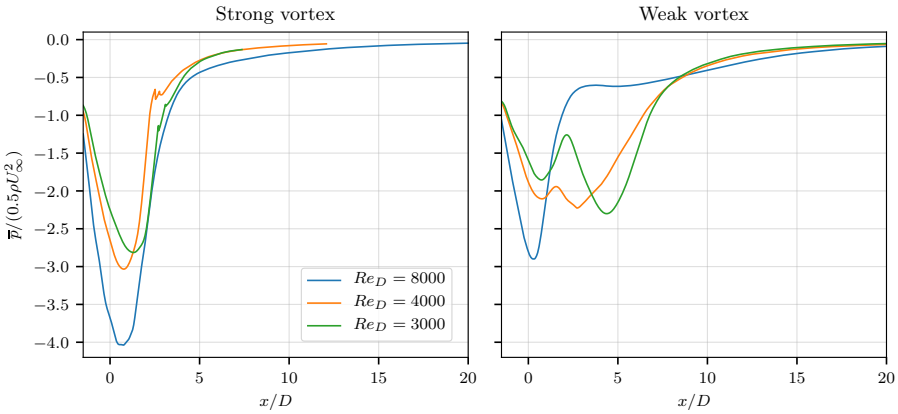

Figure 4.11: Pressure in the vortex cores at various Reynolds numbers.

This development in the pressure illustrate and proof a point we have stated multiple times, that the flow is highly transitional, Reynolds number dependent and small variations in Reynolds numbers, boundary conditions or similar will lead to major flow changes in the flow pattern.

4.4 Reynolds number 16000

To simulate the flow around the inclined prolate spheroid at Reynolds number 16 000, we created a grid with about 8.4 billion grid cells. The simulation was properly initialized and conducted on the computer system *Fram* using about 8000 CPU cores. However, suddenly we started receiving unknown memory corruption errors leading to a full crash of the simulation. We have not been able to recover from these issues, and therefore we do not have sufficient sampling length to be able to present statistical information. For the same reason, these results are not published in any journal at the time of writing this thesis. Anyhow, in the following paragraphs a brief overview of the flow and some findings will be given.

At Reynolds number 16000 another interesting phenomena occur. In lower Reynolds numbers, there were two main vortices, one originating from each side of the spheroid. At Reynolds number 16 000, there are now several coherent vortices emerging from each side of the spheroid, see

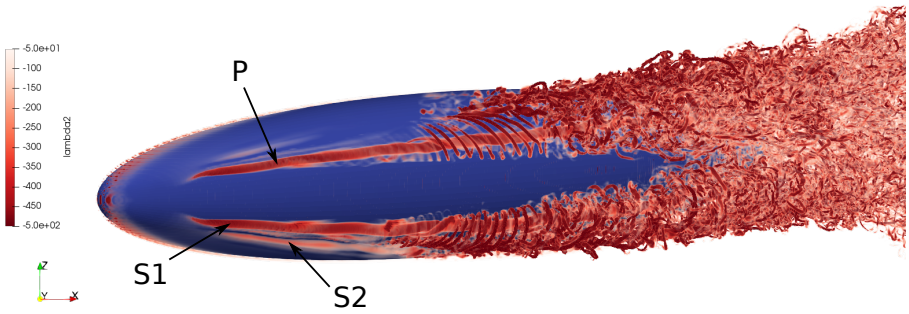

Figure 4.12: Flow structures near spheroid at Reynolds number 16000 shown by λ_2. Spheroid seen from below. Notice the multiple coherent structures on the starboard side of the spheroid (labeled *S1* and *S2* on the figure)

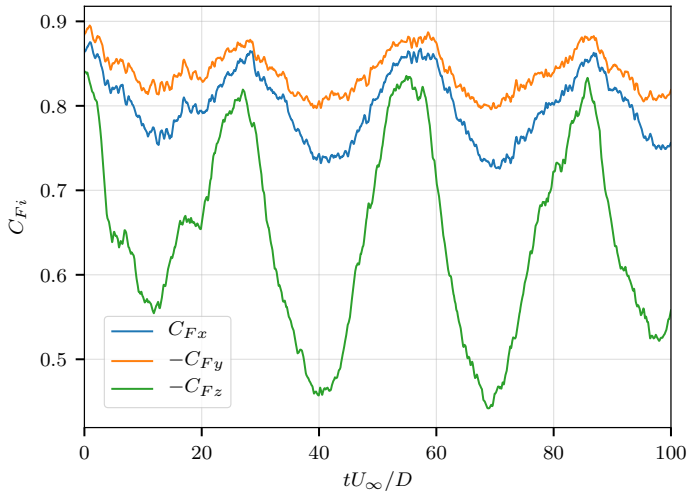

Figure 4.13: Development of forces on the spheroid at $Re_D = 16000$.

figure 4.12. This is particularly evident on the starboard side, where the secondary vortex is very predominant, see *S2* in figure 4.12. On the port side there is also a secondary vortex, however, this is significantly less visible compared to the starboard side. Both vortices on each side rotate in the same direction, but one major vortical structure dominates.

The forces on the spheroid are oscillating even stronger than at lower Reynolds numbers, see figure 4.13. We still notice the low-frequent oscillations in both the drag, lift and sideforce, and the period of these oscillations seems to have increased even further compared to the $Re_D = 8000$ case, from $20D/U_\infty$ to around $28D/U_\infty$. The sideforce coefficient now oscillate between $C_{Fz} = 0.44$ and $C_{Fz} = 0.82$, as seen in figure 4.13. Similarly, the magnitude of the oscillations in the drag- and lift-force coefficients seems to be around 0.12, around twice that observed in the case at $Re_D = 8000$.

Despite the lacking statistical sampling in this case, the observations and statements here are already conclusive in the sense that even though values might change in the last digits, the overall conclusions are likely to remain the same. The development with even stronger, periodic oscillations in the forces on the spheroid is interesting, because this is a trend that cannot persist very much further (the forces cannot grow infinitely). At some point the mechanisms that create these oscillations will break down. Since we know from the $Re_D = 8000$ case that these force oscillations is created by spatial oscillations in the two main vortices, its is very hard to speculate what happens when the Reynolds number is increased beyond 16 000.

The main patterns of this flow, which are the two coherent vortices emerging from the tip of the spheroid, are present at all the Reynolds numbers from the laminar and steady cases ($Re < 1000$) up towards the high-Reynolds number turbulent cases. The fact that we now see multiple structures on each side of the spheroid, *might* indicate that this main pattern might change. What would happen at even higher Reynolds numbers is of course a very interesting topic of investigation, and until someone actually do this, speculation is hard.

4.5 Large Eddy Simulations

One very appealing usage of the results from the DNS simulations are of course the possibilities to validate the results of other, cheaper simulations, for instance LES. In the beginning of this thesis we did a comparison between LES and DNS of the flow around a circular cylinder with fairings, which showed good agreement between the DNS and LES.

The present inclined prolate spheroid example is a very good candidate for a LES benchmark. The geometry is a double-curved surface, as opposed to the single-curved cylinder. There is an important region near the nose where the flow is laminar. There are the laminar-to-turbulent transition phase, opposing pressure gradients and highly non-uniform wake with strong rotation. The presently investigated flow is additionally in a range where small changes in the Reynolds number results in large changes in the flow topology, which makes it very important to use numerical schemes without numerical diffusion and a suitable subgrid scale model.

It has previously been attempted to simulate the higher Reynolds numbers spheroid case with OpenFOAM [23] ($Re_D = 16000$) and with the commercial CFD code Fluent [24, 25] ($Re_D = 10000$). However, this proved very difficult, the results differ significantly between the publised LES [23, 24, 25] and present DNS results. Essential flow features such as the asymmetry and distinct vortical structures seems to be missing from the LES results. There can be multiple explanations for this. One possible reason could be that the unstructured meshes not accurately resolve the very important flow region around the nose where the instability leading to the asymmetry develops. Another possible explanation could be that the numerical metods are not energy conservative, leading to excess numerical diffusion. In the most recent attempt by Zhou et al. [25] at $Re_D = 10000$, they presented a sideforce around $C_{Fz} = 0.12$ and no low-frequent oscillations in the forces. In this thesis we document a strong sideforce and low-frequent oscillations in the cases both at $Re_D = 8000$ and $Re_D = 16000$. In lights of this the results in [25] seems to be of little practical use.

To prove that it is possible to conduct a complicated flow analysis like this with a coarse mesh and LES, we conducted a LES in MGLET with around 200 million grid cells, about 1/10 of the cells of the original DNS. We used the WALE subgrid scale model [26], the same as we used in the simulations of the cylinders in chapter 3.

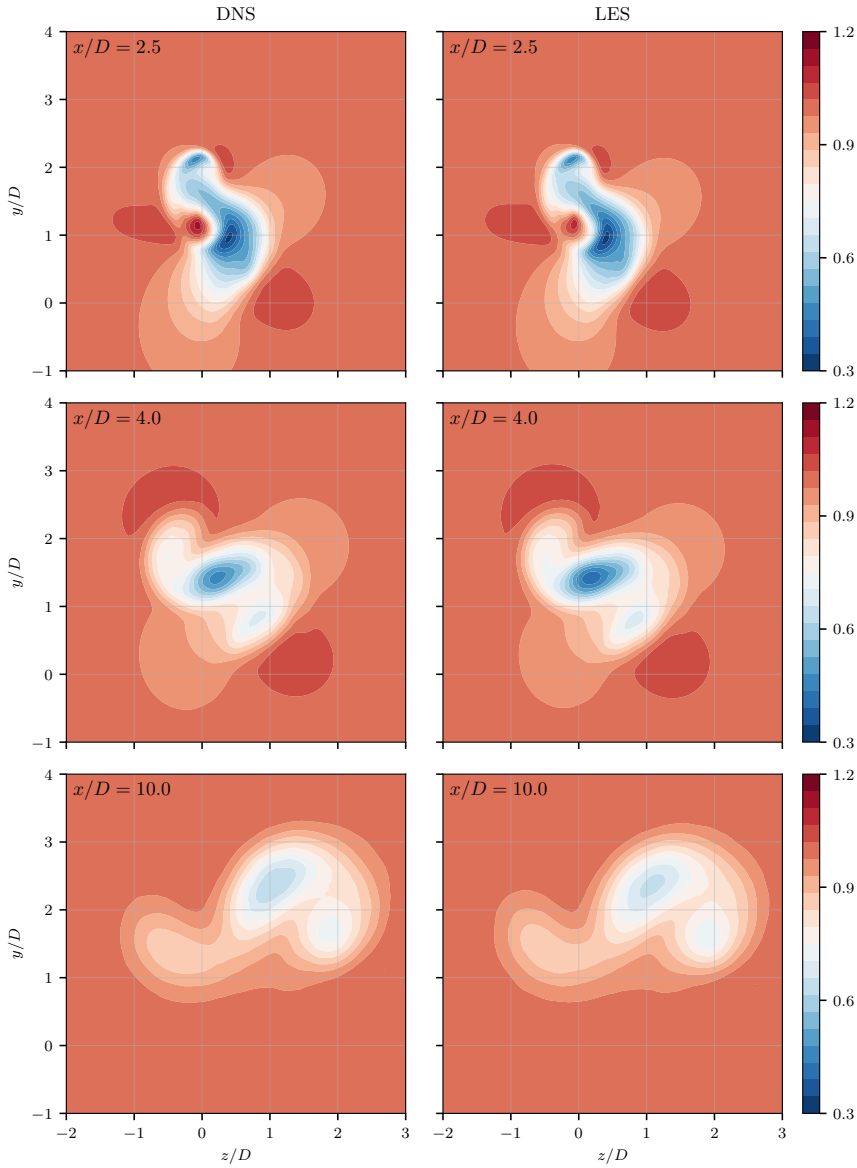

Figure 4.14: Mean streamwise velocity $\overline{U}$ from DNS and LES in three different planes ($x/D = 2.5$, $x/D = 4.0$, $x/D = 10$) for the $Re_D = 8000$ case.

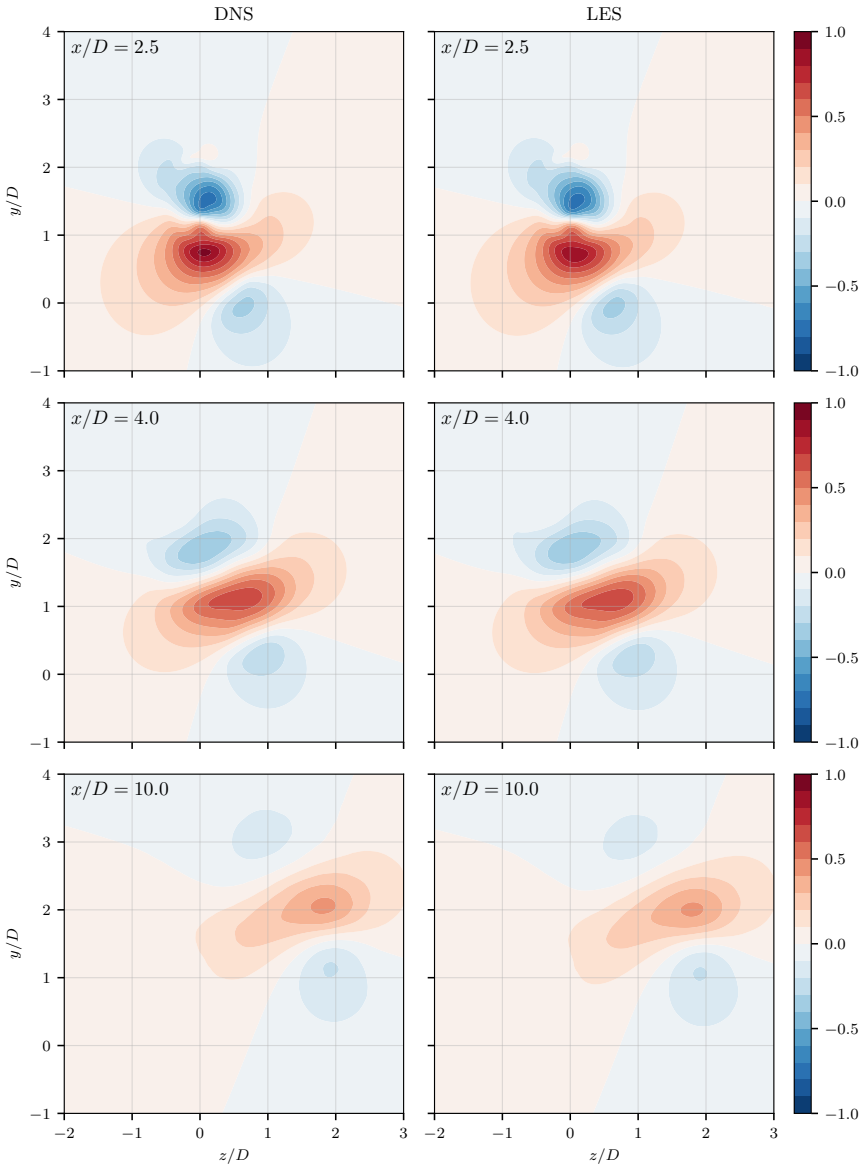

Figure 4.15: Mean crossflow velocity $\overline{W}$ from DNS and LES in three different planes ($x/D = 2.5$, $x/D = 4.0$, $x/D = 10$) for the $Re_D = 8000$ case.

Table 4.1: Mean and root-mean-square (RMS) of the force and torque coefficients from LES and DNS at $Re_D = 8000$.

Case		C_{Fx}	C_{Fy}	C_{Fz}	C_{Mx}	C_{My}	C_{Mz}
DNS	Mean	0.832	-0.831	-0.701	-0.123	0.122	0.316
	RMS	0.022	0.014	0.069	0.023	0.023	0.014
LES	Mean	0.837	-0.836	-0.705	-0.120	0.119	0.317
	RMS	0.022	0.014	0.067	0.023	0.023	0.015

The results are summarised in figures 4.14 and 4.15. As the figures show, there are very good agreement between the mean flow field in the wake predicted with LES compared to the (10 times more expensive) DNS results. The forces on the spheroid computed with DNS and LES are given in table 4.1. The results shows a very good agreement with less than 1% deviation between the LES and DNS results, both for the mean and RMS values.

In the previous chapters we have presented the preliminary results from a DNS of the 45° inclined spheroid case at $Re_D = 16000$, however, the massive amount of grid cells necessary (8.5 billion cells) makes this simulation extremely complicated to conduct. With the good comparisons between DNS and LES in the present $Re_D = 8000$ case, there is however, a very good chance that the same cases would be 'trivial' to conduct with a LES model and approximately 1 billion grid cells, given a good high-quality mesh.

Chapter 5

Conclusions and outlook

This work have advanced the field of high-fidelity numerical simulations of turbulent flows through detailed investigations of the flow around cylinders and prolate spheroids. This have been aided by developments in simulation tools and methods. We have produced results on grids with up to 8.4 billion (10^9) cells, which in this field is very rare.

During this work we have simulated the effects of different boundary conditions at cylinder ends, which will have important implications for how to conduct similar PIV experiments in the future. We also re-analysed previous cases of the inclined prolate spheroid and found details that earlier simulations could not catch due to computational constraints.

In the last part of the work we increased the Reynolds number of the spheroid case beyond what was previously possible to do, up to $Re_D = 16000$. This lead to the discovery of many interesting phenomena which have never been observed before. This shows the true power of state-of-the art simulation technology.

In the future I believe that there will be many interesting paths to develop this work further. I have only briefly experimented with the new cut-cell immersed boundary method which will obvious be a very appealing tool for such simulations in the future. I believe that the details this immersed boundary method give close to the surface could help in understanding the nature of the origin and development of the asymmetry in the spheroid wake.

This work and the challenges related to run the spheroid case with 8.1

billion cells at Reynolds number 16 000 shows that we are facing even larger problems in the future if we want to continue to resolve all details of such cases with DNS. The last part of this thesis, briefly compare DNS and LES, and shows that we can produce very good flow fields with only a fraction of the grid cells that we use in DNS. This allows for increase the Reynolds number even further with no additional effort. This allows us to continue the $Re_D = 16000$ case with an LES model and a reduced grid to really investigate what happens in this case. The appearance of multiple coherent structures are something not reported before and should be followed up.

Bibliography

[1] J. H. Ferziger and M. Peric. *Computational Methods for Fluid Dynamics*. 3rd ed. Springer-Verlag Berlin Heidelberg, 2002. DOI: 10.1007/978-3-642-56026-2.

[2] J. H. Williamson. 'Low-storage Runge-Kutta schemes'. In: *Journal of Computational Physics* vol. 35, no. 1, Mar. 1980, pp. 48–56. DOI: 10.1016/0021-9991(80)90033-9.

[3] N. Peller, A. L. Duc, F. Tremblay and M. Manhart. 'High-order stable interpolations for immersed boundary methods'. In: *International Journal for Numerical Methods in Fluids* vol. 52, no. 11, Apr. 2006, pp. 1175–1193. ISSN: 1097-0363. DOI: 10.1002/fld.1227.

[4] M. Manhart. 'A zonal grid algorithm for DNS of turbulent boundary layers'. In: *Computers & Fluids* vol. 33, no. 3, Mar. 2004, pp. 435–461. ISSN: 0045-7930. DOI: 10.1016/s0045-7930(03)00061-6.

[5] H. Strandenes, M. Manhart, M. Allalen, I. Pasichnyk and W. Schanderl. 'Improving scalability for the CFD software package MGLET'. In: *Innovatives Supercomputing in Deutschland* vol. 14, no. 2, 2016, pp. 48–51.

[6] H. Strandenes, J. P. Gallardo, B. Pettersen and H. I. Andersson. 'On the Effect of Boundary Conditions on the Flow around a Cylinder in a Channel'. In: *MekIT'15 Eigth national conference on Computational Mechanics*. Ed. by B. Skallerud and H. I. Andersson. 2015, pp. 343–357. ISBN: 978-84-944244-9-6.

[7] H. Strandenes, J. P. G. Canabes, J. Visscher, B. Pettersen, H. I. Andersson, H. Lie and R. Baarholm. 'A Comparative Study Between DNS, LES and PIV for a Marine Riser With Fairings'. In: *ASME*

2015 34th International Conference on Ocean, Offshore and Arctic Engineering. American Society of Mechanical Engineers. 2015. DOI: 10.1115/OMAE2015-41494.

[8] H. Strandenes, B. Pettersen, H. I. Andersson and M. Manhart. 'Influence of spanwise no-slip boundary conditions on the flow around a cylinder'. In: *Computers & Fluids* vol. 156, 2017, pp. 48–57. DOI: 10.1016/j.compfluid.2017.06.025.

[9] A. Prasad and C. H. Williamson. 'The instability of the shear layer separating from a bluff body'. In: *Journal of Fluid Mechanics* vol. 333, Feb. 1997, pp. 375–402. DOI: 10.1017/S0022112096004326.

[10] P. Stansby. 'The effects of end plates on the base pressure coefficient of a circular cylinder'. In: *Aeronautical Journal* vol. 78, Jan. 1974, pp. 36–37. DOI: 10.1017/S0001924000036319.

[11] F. Jiang, J. P. Gallardo, H. I. Andersson and Z. Zhang. 'The transitional wake behind an inclined prolate spheroid'. In: *Physics of Fluids* vol. 27, no. 9, 2015, p. 093602. DOI: 10.1063/1.4929764.

[12] F. Jiang, H. I. Andersson, J. P. Gallardo and V. L. Okulov. 'On the peculiar structure of a helical wake vortex behind an inclined prolate spheroid'. In: *Journal of Fluid Mechanics* vol. 801, 2016, pp. 1–12. DOI: 10.1017/jfm.2016.428.

[13] G. K. El Khoury, H. I. Andersson and B. Pettersen. 'Crossflow past a prolate spheroid at Reynolds number of 10000'. In: *Journal of Fluid Mechanics* vol. 659, 2010, pp. 365–374. DOI: 10.1017/S0022112010003216.

[14] C. J. Chesnakas and R. L. Simpson. 'Full three-dimensional measurements of the cross-flow separation region of a 6:1 prolate spheroid'. In: *Experiments in Fluids* vol. 17, no. 1-2, 1994, pp. 68–74. DOI: 10.1007/BF02412805.

[15] C. J. Chesnakas, D. Taylor and R. L. Simpson. 'Detailed investigation of the three-dimensional separation about a 6:1 prolate spheroid'. In: *AIAA journal* vol. 35, no. 6, 1997, pp. 990–999. DOI: 10.2514/2.208.

[16] M. C. Goody, R. L. Simpson and C. J. Chesnakas. 'Separated flow surface pressure fluctuations and pressure-velocity correlations on prolate spheroid'. In: *AIAA journal* vol. 38, no. 2, 2000, pp. 266–274. DOI: 10.2514/2.953.

[17] N. T. Hoang, T. G. Wetzel and R. L. Simpson. 'Unsteady measurements over a 6:1 prolate spheroid undergoing a pitch-up maneuver'. In: *32nd Aerospace Sciences Meeting and Exhibit*. 1994, p. 197. DOI: 10.2514/6.1994-197.

[18] T. G. Wetzel and R. L. Simpson. 'Unsteady crossflow separation location measurements on a maneuvering 6:1 prolate spheroid'. In: *AIAA journal* vol. 36, no. 11, 1998, pp. 2063–2071. DOI: 10.2514/2.307.

[19] F. Jiang, J. P. Gallardo and H. I. Andersson. 'The laminar wake behind a 6:1 prolate spheroid at 45° incidence angle'. In: *Physics of Fluids* vol. 26, no. 11, 2014, p. 113602. DOI: 10.1063/1.4902015.

[20] J. Jeong and F. Hussain. 'On the identification of a vortex'. In: *Journal of Fluid Mechanics* vol. 285, 1995, pp. 69–94. DOI: doi.org/10.1017/S0022112095000462.

[21] J. Kreuzinger and F. Schwertfirm. 'Erweiterung einer immersed-boundary-Methode auf die Simulation der Schallabstrahlung umströmter bewegter Körper'. In: *DAGA 2018 – 44. Deutsche Jahrestagung für Akustik*. 2018.

[22] H. Strandenes, F. Jiang, B. Pettersen and H. I. Andersson. 'Near-Wake of an Inclined 6:1 Spheroid at Reynolds Number 4000'. In: *AIAA Journal*, 2019. DOI: dx.doi.org/10.2514/1.J057615.

[23] H. S. Larssen. 'Turbulence Modelling of the Flow Around a Prolate Spheorid'. MSc thesis. Norwegian University of Science and Technology, 2018.

[24] R. He, Z. Zhang and X. Wang. 'Wake instabilities and flow state analysis of the flow past a prolate spheroid'. In: *Tenth International Conference on Computational Fluid Dynamics (ICCFD10)*. July 2018.

[25] H. Zhou, H. Liu, Z. Zhang, X. Wang and D. Feng. 'Numerical Study of the Wake Behind an Inclined Prolate Spheroid at Re=10000 Using LES'. In: *ASME 2018 37th International Conference on Ocean, Offshore and Arctic Engineering*. American Society of Mechanical Engineers. 2018.

[26] F. Nicoud and F. Ducros. 'Subgrid-scale stress modelling based on the square of the velocity gradient tensor'. In: *Flow, Turbulence and Combustion* vol. 62, no. 3, Sept. 1999, pp. 183–200. DOI: 10.1023/A:1009995426001.

Appendix A

Bibliography

During the course of the present doctoral work, I have given presentations at several sientific conferences and contributed to scientific works other than the papers attacehd to the present thesis. The following list is a bibliography of these presentationa. In most cases there is an associated conference paper avaiable electreonically.

2013

- Håkon Strandenes, Bjørnar Pettersen, Helge I. Andersson: Numerical Simulations of Particle-Laden Wake Flows. In: 16th Numerical Towing Tank Symposium, September 2013. URL: `https://www.uni-due.de/imperia/md/content/ist/nutts_16_2013_muelheim.pdf`

- Håkon Strandenes: Implementation of an Efficient Storage Strategy for Fluid-Particle Simulations in OpenFOAM. In: MekIT'13 Seventh National Conference on Computational Mechanics, 2013, Akademika forlag, ISBN: 978-82-321-0266-2

2014

- Håkon Strandenes, Bjørnar Pettersen: New IO Strategy for OpenFOAM on HPC Systems. In: Parallel Computational Fluids Dynamics-PARALLEL CFD 2014, A book of extended abstracts of the 26th International Conference on Computational Fluid Dynamics held

in Trondheim, Norway, 20-22 May, 2014. International Center for Numerical Methods in Engineering (CIMNE), 2014, ISBN 978-84-941686-6-6

- Håkon Strandenes, Jose P. Gallardo, Bjørnar Pettersen, Helge I. Andersson: Comparison of LES and DNS for the flow past a circular cylinder with fairings. In: 17th Numerical Towing Tank Symposium, September 2014. URL: `https://www.uni-due.de/imperia/md/content/ist/nutts_17_2014_marstrand.pdf`

2015

- Håkon Strandenes, Audun Yrke, Lennard Bösch, Christian Kosacki, Bjørnar Pettersen, Helge I. Andersson: Recent DNS, LES and Experiments on a Cylinder with Fairings. In: 18th Numerical Towing Tank Symposium, September 2015. URL: `https://www.uni-due.de/imperia/md/content/ist/nutts_18_2015_cortona.pdf`

- Håkon Strandenes, Jose P. Gallardo, Jan H. Visscher, Bjørnar Pettersen, Helge I. Andersson, Halvor Lie, Rolf J. Baarholm: A Comparative Study Between DNS, LES and PIV for a Marine Riser With Fairings. In: ASME 2015 34th International Conference on Ocean, Offshore and Arctic Engineering Volume 2: CFD and VIV. ASME Press 2015 ISBN 978-0-7918-5648-2.

- Håkon Strandenes, Jose P. Gallardo, Bjørnar Pettersen, Helge I. Andersson: On the Effect of Boundary Conditions on the Flow around a Cylinder in a Channel. In: Proceedings of MekIT'15 Eighth National Conference on Computational Mechanics. International Center for Numerical Methods in Engineering (CIMNE), 2015, ISBN 97884944244-96

- Håkon Strandenes, Jose P. Gallardo, Bjørnar Pettersen, Helge I. Andersson: Comparison of LES and DNS for the flow past a circular cylinder with fairings. In: 17th Numerical Towing Tank Symposium (NuTTS 2014). Curran Associates Inc, 2015, ISBN 9781634398282. URL: `https://www.uni-due.de/imperia/md/content/ist/nutts_18_2015_cortona.pdf`

2016

- Håkon Strandenes, Michael Manhart, Momme Allalen, Igor Pasichnyk, Wolfgang Schanderl: Improving scalability for the CFD software package MGLET. In: Innovatives Supercomputing in Deutschland, 2016, vol. 14.1. URL: `http://inside.hlrs.de/assets/pdfs/inside_autumn16.pdf`

2017

- Håkon Strandenes, Bjørnar Pettersen, Helge I. Andersson, Michael Manhart: Influence of spanwise no-slip boundary conditions on the flow around a cylinder. In: Computers & Fluids, 2017, vol. 156.

- Håkon Strandenes, Fengjian Jiang, Bjørnar Pettersen, Helge I. Andersson: Recent Developments and New Results on The Flow Around an Inclined 6:1 Prolate Spheroid. In: MekIT'17 - Ninth national conference on Computational Mechanics, International Center for Numerical Methods in Engineering (CIMNE), 2017, ISBN 978-84-947311-1-2

Attached paper I

On the Effect of Boundary Conditions on the Flow around a Cylinder in a Channel

Håkon Strandenes, Jose P. Gallardo, Bjørnar Pettersen, Helge I. Andersson

In: Proceedings of MekIT'15 Eighth National Conference on Computational Mechanics, International Center for Numerical Methods in Engineering, 2015, ISBN 97884944244-96

8. National Conference on Computational Mechanics
MekIT'15
B. Skallerud and H I Andersson (Eds)

ON THE EFFECT OF BOUNDARY CONDITIONS ON THE FLOW AROUND A CYLINDER IN A CHANNEL

HÅKON STRANDENES[1,3], JOSÉ P. GALLARDO[1], BJØRNAR PETTERSEN[1] AND HELGE I. ANDERSSON[2]

[1]Department of Marine Technology
[2]Department of Energy and Process Engineering

Norwegian University of Science and Technology
Trondheim, Norway

[3] Corresponding author: hakon.strandenes@ntnu.no

Key words: CFD, LES, boundary conditions, cylinder, channel

Abstract. In this paper, the incompressible external flow around an offshore drilling riser with fairings at Reynolds number 5000 is used to study the effects of varying boundary conditions in numerical simulations. We use a direct numerical simulation (DNS) to compare and verify large eddy simulations (LES) and use further simulations to explain the effects of different boundary conditions that can occur in a physical experiment. Particular attention is drawn towards the impact of the no-slip spanwise boundary condition often occurring in circulating water tunnels and similar setups because of fixed walls.

NOMENCLATURE

C_D	Drag coefficient	St	Strouhal number $St = f_v D/U_\infty$
C_L	Lift coefficient	T	Width of domain (in z-direction)
C_{pb}	Base pressure coefficient	u, v, w	Instantaneous fluid velocity
D	Cylinder diameter	$\overline{U}, \overline{V}, \overline{W}$	Time-averaged fluid velocity
H	Height of domain (in y-direction)	u', v', w'	$u' = u - \overline{U}$ etc.
f_v	Vortex shedding frequency	U_∞	Inlet (freestream) velocity
L_r	Recirculation length	ν	Kinematic viscosity of fluid
L_v	Vortex formation length	$\overline{\square}$	Time-averaged coefficient
Re	Reynolds number $Re = DU_\infty/\nu$	$\square^{\text{rms}}$	Root-mean-square $= \sqrt{\overline{(\square - \overline{\square})^2}}$

1 INTRODUCTION

1.1 Background

Comparing simulations with real-life physical experiments can often be requested to prove that the simulations represent the physical world. In computational fluid dynamics, this is often easier said than done. Both simulations and experiments have their strengths and weaknesses. One Achilles' heel of experiments of external fluid flows is the ability, or lack of ability, to control, monitor and adjust the boundary conditions. Even if the desired physical setup is a body (which can be a car, a ship, a sport athlete or anything else) in 'infinite fluid', the experimental facility will always impose certain boundary conditions onto the flow that is not in accordance with the desired 'infinite fluid' configuration.

One of the strengths about performing numerical simulations is that it is possible to implement different boundary conditions that are not possible to achieve in real life, such as slip-walls and periodic conditions. This allows us to adjust the boundary conditions in a controlled manner and assess their impact on the flow of interest.

We have previously studied the incompressible flow around an offshore drilling riser with fairings, called 'Short Crab Claw' [1] at Reynolds number 5000 with both direct numerical simulation (DNS) and large eddy simulation (LES) [2]. The agreement between the different simulations were relatively poor, and we concluded that we needed to work more on the LES to reduce the difference with DNS. We have also performed more detailed DNS (with longer temporal sampling lengths) and compared the results from both DNS and LES with particle image velocimetry (PIV) experiments [3]. Surprisingly, the PIV data was found to be completely different from the simulation results. In previous works, we were not able to identify the causes of the large differences between the simulations and the experiments. Many possible hypothesises for the causes were presented, such as too short sampling time, inflow turbulence and blockage effects.

1.2 Present study

The present study is a numerical investigation of the effects of the different boundary conditions we use in simulations and experiments. We will re-use the previously presented DNS data [2, 3] in this paper as a reference dataset. However, to assess and reduce the previously mentioned differences between DNS and LES, we have improved and re-done all LES data for this study. To keep the number of possible explanations and discussions manageable, we will not compare any results with experimental data. We will only investigate a small subset of the possible causes of the previously published differences between the simulations and experiments. By comparing simulations with simulations it is possible to disregard completely any discussion on topics such as inflow turbulence and experimental setups that contribute to the differences and uncertainties.

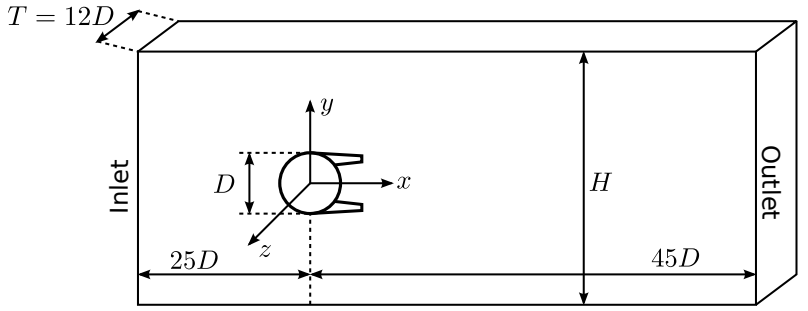

Figure 1: Simulation domain and coordinate system. The origin of the coordinate system is in the center of the circular part of the cylinder. The three directions are named streamwise (x-direction), crossflow (y-direction) and spanwise (z-direction). H is a variable height. Not to scale.

1.3 Previous work by others

Other authors have studied various cylinders in channels extensively, but the focus in the existing literature seems to be cylinders in between two infinitely large plates with a specific spacing. Zovatto and Pedrizzetti [4] studied the 2D flow around a circular cylinder between two plane walls up to Reynolds number 2000 while varying the blockage ratio and the distance from the cylinder to the nearest wall. Kim et al. [5] used LES to study the flow past a square cylinder in a channel for Reynolds number 3000 and blockage ratio of 20%. They found that the presence of the channel walls reduced the size of the recirculation region and induced larger drag force and lift force fluctuations on the cylinder. Charkaborty et al. [6] did the same study for 2D flows past a circular cylinder with various blockage ratios up to Reynolds number 200, and came to the same conclusions as Kim et al. [5] for the square cylinder.

On the topic of spanwise boundary conditions Huang et al. [7] considered the end-wall effects on vortex shedding around a circular cylinder at $Re = 100$ in which they studied the difference between slip and no-slip boundary conditions on the spanwise boundaries. They found that for a cylinder of length $6D$ the effect of no-slip boundary conditions substantially altered the vortex shedding in the middle of the channel. However, their low Reynolds number and short spanwise length does not make any useful reference for our problem.

2 PROBLEM AND DEFINITIONS

The simulation domain is shown in figure 1. The coordinate system is indicated in the figure, where the x-, y- and z-direction are the streamwise, crossflow and spanwise direction, respectively. The width of the domain T (and thus also the cylinder length), is fixed to $T = 12D$ in all new cases in this paper. Previously published data use a length of $T = 6D$. The reason for doubling the width is to mimic an experimental setup in a square

Table 1: Simulation matrix.

Simulation	A	B	C	DNS ref. [3]
Domain width T/D	12	12	12	6
Domain height H/D	12	12	40	40
Top & bottom BC	No-slip	No-slip	Slip	Slip
Spanwise BC	No-slip	Periodic	Periodic	Periodic

water tunnel, with a blockage ratio of 1/12. In the cases where the flow is homogeneous along the cylinder span, this change should not influence the results. Parnaudeau et al. [8] investigated the difference between a span of πD and $2\pi D$ for the flow around a circular cylinder at $Re = 3900$. They found the difference to be very small and concluded that a span of πD in many cases was good enough. With that in mind, we believe that $6D$ and $12D$ should produce similar results.

The height of the domain H is adjusted to study the sensitivity of the results with respect to this parameter. In the original DNS and LES [2], the height was fixed to $40D$. As a part of this work, we want to investigate the effect of blockage and will include two cases with a smaller height of $H = 12D$ in addition to our reference case with $H = 40D$.

To mimic a cylinder that is infinitely long, we impose a periodic boundary condition in the spanwise direction. We have also have a simulation where we impose solid no-slip walls on the spanwise boundaries to investigate what happens in a physical water tank with no-slip walls.

The inlet flow is laminar, uniform and constant in all simulations, disregarding any turbulence and boundary layers. The outlet condition is a fixed pressure outlet. The Reynolds number is, as previously mentioned, $Re = 5000$ in all cases.

The different simulated cases are summarized in table 1. All simulations were run until the effects of any initial condition no longer was present. After this initial phase, statistics was sampled over 1800 D/U_∞ time units, corresponding to roughly 360 vortex shedding cycles (given a Strouhal number of $St \approx 0.2$).

3 NUMERICAL METHODS

The code *MGLET* [9] has been used to perform all simulations presented in this paper, including our reference DNS simulations. The previously presented LES simulations in [2, 3] were done with OpenFOAM, but this data is not re-used here. In short, MGLET is a finite-volume code solving the incompressible Navier-Stokes equations using linear interpolation and integration for all spatial terms, hence leading to second-order accuracy in space. A third-order explicit Runge-Kutta time integration scheme is used for time stepping.

MGLET uses a staggered Cartesian grid and introduces the solid geometry through

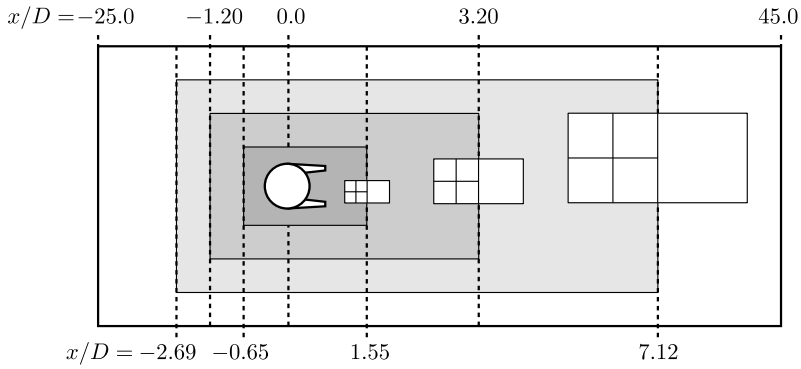

Figure 2: Schematic illustration in 2D of the grid design and refinement process. The grid refinement regions are marked with darker shades of grey for finer regions. Not to scale.

an immersed boundary method [10]. In the LES presented here, we used three levels of local grid refinement (plus one coarse, parent grid) around the cylinder. This resolves the cylinder, its boundary layers and the wake behind it sufficiently while keeping the total number of grid cells at a reasonable level. The refinement process is a simple cell splitting, in which each parent grid cell subject to refinement is split into eight equal (3D) child cells [11]. The grid itself is too fine to print, but a schematic illustration of its design is given in figure 2. The resulting smallest grid cell size is $0.00625D$, about twice the size of the smallest cells in the reference DNS data, which used a minimum cell size of $0.003D$. In total about 152 million grid cells were used in the present LES work, compared to about 491 million grid cells in the reference DNS dataset. When taking into account that the width of the domain T in the LES is twice that of the DNS ($12D$ versus $6D$), one see that the overall average cell density is about one order of magnitude higher in the DNS than in the LES.

The 'Wall-Adaptive Local Eddy-viscosity' model, henceforth WALE model [12], was used as the subgrid-scale model for the LES simulations. The time step was fixed at 0.002 D/U_∞ in all LES simulations.

3.1 'Empty tank' conditions

Case A in this work resembles an experimental facility in which the fluid flows between four fixed walls in a square channel, like a water or wind tunnel. The ideal and desired setup is that the flow in the center of the channel is uniform and free of any influence from the tank wall boundary layers.

A simulation with an empty tank have been performed, i.e. a simulation without any geometry in the channel. In this way, we can show how the boundary layers grow without the interference from the cylinder. A slice through the tank at the location of the cylinder ($x = 0$) is presented in figure 3. This plot shows that there is a large region of nearly

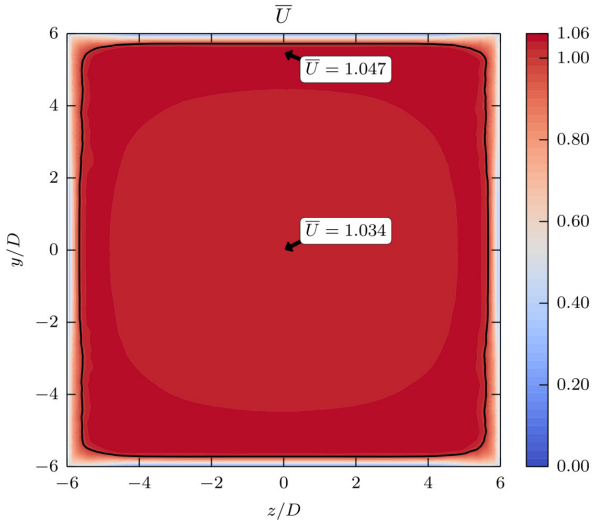

Figure 3: Map of $\overline{U}$ in the cross section of an empty channel corresponding to case A (with no-slip walls) at position $x = 0$. The solid black line indicate a contour for $\overline{U} = 1.0$.

uniform velocity in almost the entire cross-section. The velocity at the center is slightly larger than the inlet velocity by about 3.4%. When approaching the walls, the velocity increases from the value in the center of the channel, up to a maximum of 4.7% larger than the inflow velocity. The boundary layer thickness predicted by a Blasius profile for this location in the tank is $\delta \approx 0.35D$, and this seems to match with the simulated channel flow. This simulation also shows that the empty channel is free of any turbulence, except from some small fluctuations in the corners where two walls intersect.

In total, it seems like the simulated channel is well suited for this purpose, even though the velocity profile is not completely uniform. However, in real life experiments this is not the case either.

4 RESULTS

4.1 General coefficients

The main flow results and force coefficients are summarized in table 2. The mean lift force coefficient $\overline{C_L}$ is left out because it for symmetry reasons is zero. The force coefficients presented here are measured (and averaged) over the entire span of the cylinder. A practical consequence of this is that the ends of the cylinder are within the wall boundary layer in case A, and consequently the force coefficients are affected by this. The Strouhal number is calculated based on the time history of the fluid velocity u and v in position

$(x, y, z) = (3D, 0.45D, 0)$ in the wake. The base pressure coefficient is based on the mean pressure difference between a point immediately behind the cylinder (at $x = 0.5D$) in the center of the domain and a corresponding point upstream at $x = -20D$. We do however not consider the mean base pressure coefficient to be of any relevance other than comparing case C with the DNS (and possibly previously performed LES). For cases A and B the presence of the no-slip walls will lead to a pressure drop along the channel that will affect the base pressure coefficient.

All statistics for case B and C have been averaged over the span of the cylinder to improve the quality of the data. The DNS reference data are also averaged over the span of the cylinder. However, due to the fact that case A is not homogeneous in the spanwise direction this averaging cannot be performed here. The statistics for case A is consequently extracted from a plane in the middle of the channel at $z = 0$.

The mean recirculation length L_r is found by locating the zero mean streamwise velocity $\overline{U}$ at the centerline in the domain. The vortex formation length L_v is found by searching for the maximum value of $\overline{u'u'}$ along the same line. Here $U_{\min}$ is the minimum value of the mean streamwise velocity $\overline{U}$ along the same line. All these values are plotted in figure 4.

4.2 Effect and validation of LES model

Simulation C and the reference DNS differ only by the spanwise length T of the domain ($T = 12D$ in the LES versus $T = 6D$ in the DNS), a coarser grid and the use of an LES model for the non-resolved stresses. We believe that the span of $T = 6D$ in the DNS is enough, thus allowing us to compare these two cases directly to see the effect of the coarser grid and subgrid scale model on the flow.

Figure 5 shows a comparison of the mean flow fields from our DNS reference and the LES case with the wide domain (case C). The agreement seems to be acceptable between the two simulations. The largest difference is in the wake close to the cylinder, in the region between $x = 1.0D$ and $x = 1.8D$. However, the differences here are not large.

The Strouhal number St is identical in the three first digits between the simulations, and the mean drag coefficient $\overline{C_D}$ from the LES is only 0.6% lower than from the DNS. The base pressure coefficient $-\overline{C_{pb}}$ differs only by 0.3%. On the other hand, coefficients like the RMS of the drag and lift force seems to be rather different. One possible explanation for this might be that the forces in the LES is measured over a cylinder that is twice as long as in the DNS. Increasing the length will probably change how the global, integrated, forces on the cylinder behave.

In summary, despite the difference between in the RMS of the force coefficients, we believe that compared to DNS, the results from the LES is sufficiently good to proceed using this grid and simulation setup in the following studies.

Table 2: Main flow results. The symbols are explained in the nomenclature in the beginning of the paper. The recirculation and vortex formation length are measured from the center of the cylinder.

Simulation	A	B	C	DNS ref. [3]
St	0.219	0.239	0.225	0.225
$\overline{C_D}$	0.919	0.952	0.877	0.882
C_D^{rms}	0.0132	0.0120	0.0107	0.0124
C_L^{rms}	0.0278	0.0713	0.0640	0.0482
$-\overline{C_{pb}}$	0.831	0.901	0.766	0.764
L_r/D	2.798	2.300	2.358	2.391
L_v/D	2.737	1.562	1.587	1.629
$U_{\min}/U_\infty$	−0.326	−0.416	−0.402	−0.384

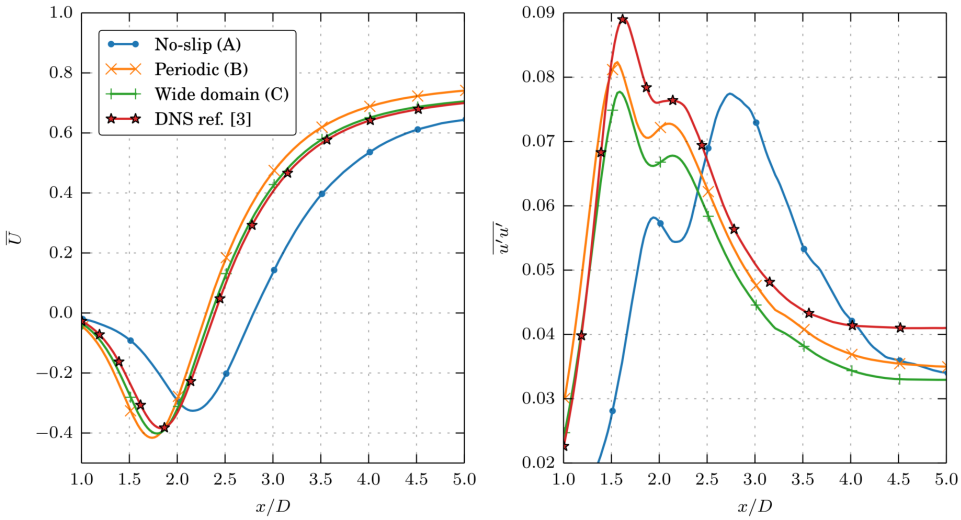

Figure 4: Profiles of mean velocity $\overline{U}$ and $\overline{u'u'}$ along the center line behind the cylinder. The origin of the x-axis is in the center of the cylinder.

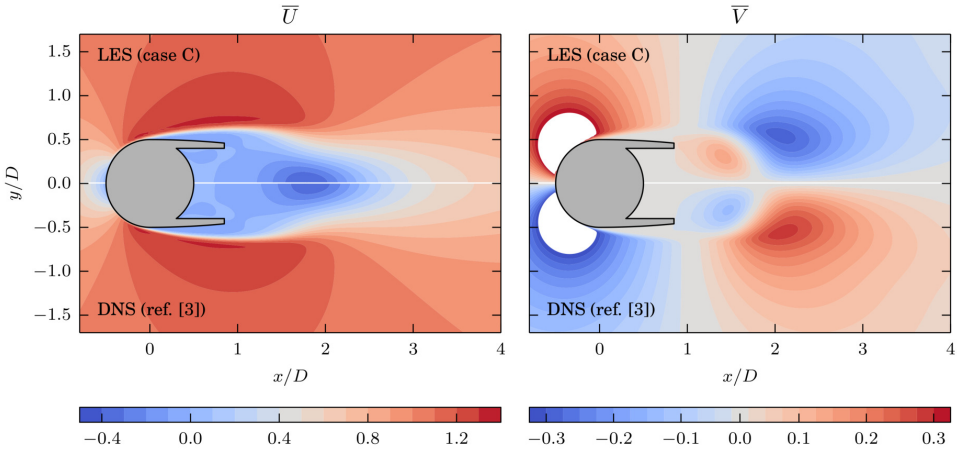

Figure 5: Comparison between the DNS reference data and LES case C (wide grid). The white regions in the rightmost figure are areas where the fluid velocity is outside the color scale, which is adapted to suite the velocity range in the wake. The upper half ($y > 0$) of the figures are the wide domain (case C) and the lower half ($y < 0$) are the DNS reference case [3].

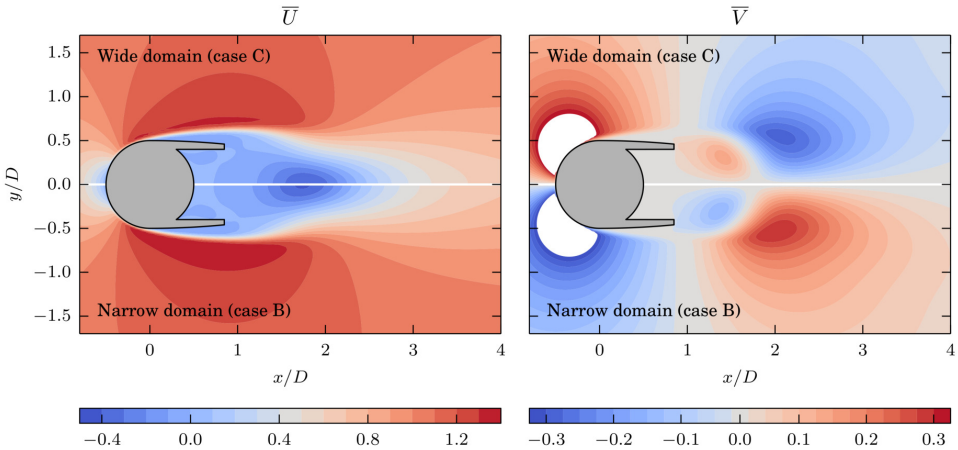

Figure 6: Comparison between the wide (case C with $T = 40D$) and narrow (case B with $T = 12D$) domain to illustrate the effect of blockage. The largest visible effect is immediately above and below the cylinder, where higher velocities is seen with the narrow domain.

4.3 Effect of blockage

The effect of blockage can be seen by comparing the simulation with the wide domain (case C) with the simulation with narrower domain and no-slip boundary conditions on the y-normal boundaries (case B). Both cases have the same boundary conditions in the spanwise direction, and the grid is identical around the cylinder and in the wake region.

From the main flow and force coefficients in table 2 we can see that both mean and RMS value of the drag force is, not surprisingly, higher for the case with high blockage than for the cases without. The base pressure coefficient is also substantially higher for case B compared to case C, witn an increase of almost 18 %. The recirculation length and vortex formation length seems to be more or less identical between the cases.

Figure 6 shows that the main effect of the blockage is *not* to modify the mean flow field in the wake behind the cylinder, but to introduce a rather large region with higher velocities above and below the cylinder. Figure 4 also show that the mean streamwise velocity at the centerline is almost identical between the case with high and low blockage. Inspecting the numerical result show us that the maximum streamwise velocity $\overline{U}$ in case C is 1.32, and case B is 1.37. Both maxima are located at the shoulders of the cylinder, near the separation point. Even though it is intuitive that the increased blockage lead to higher velocities past the obstacle in the channel, it is surprising that the mean pattern in the wake is not more affected. This could be the effect of the fairings; however, that is left as an open question for later investigation.

4.4 Effect of no-slip spanwise boundaries

The effect of the no-slip boundaries is perhaps the most interesting comparison in this study. The first sign of this being a special case is via the coefficients in table 2, where we see that the RMS of the lift coefficient C_L^{rms} is less than half of the value of the other LES cases, and that the recirculation length L_r is about $0.5D$ longer than all other cases. The vortex formation length L_v have increased from $1.56D$ in case B to $2.73D$ in case A.

The plot in figure 4 shows that both the minimum and maximum value of the mean streamwise velocity $\overline{U}$ is lower than in the other cases. The shape of the curve for $\overline{u'u'}$ is significantly changed. Instead of having one primary peak first around $x = 1.6D$, and one almost invisible secondary peak at $x = 2.2D$, there is now a smaller, secondary peak at $x = 1.9D$ and a higher, primary peak as far downstream as $x = 2.7D$. The peak at $x = 2.7D$ is also about as high as the primary peaks seen from the other simulations. It should be noted that case A is the only case where the statistics in the xy-plane is not averaged over the span of the cylinder.

Figure 7 compare the mean flow field in the case of periodic and no-slip sidewalls, and it is clear that the mean wake is significantly different in the two cases. The wake is severely stretched in the streamwise direction in case A. It seems like the regions with high and low mean crossflow velocity $\overline{V}$, that in the other cases 'touch' the corners of the fairings, now are almost detached from these.

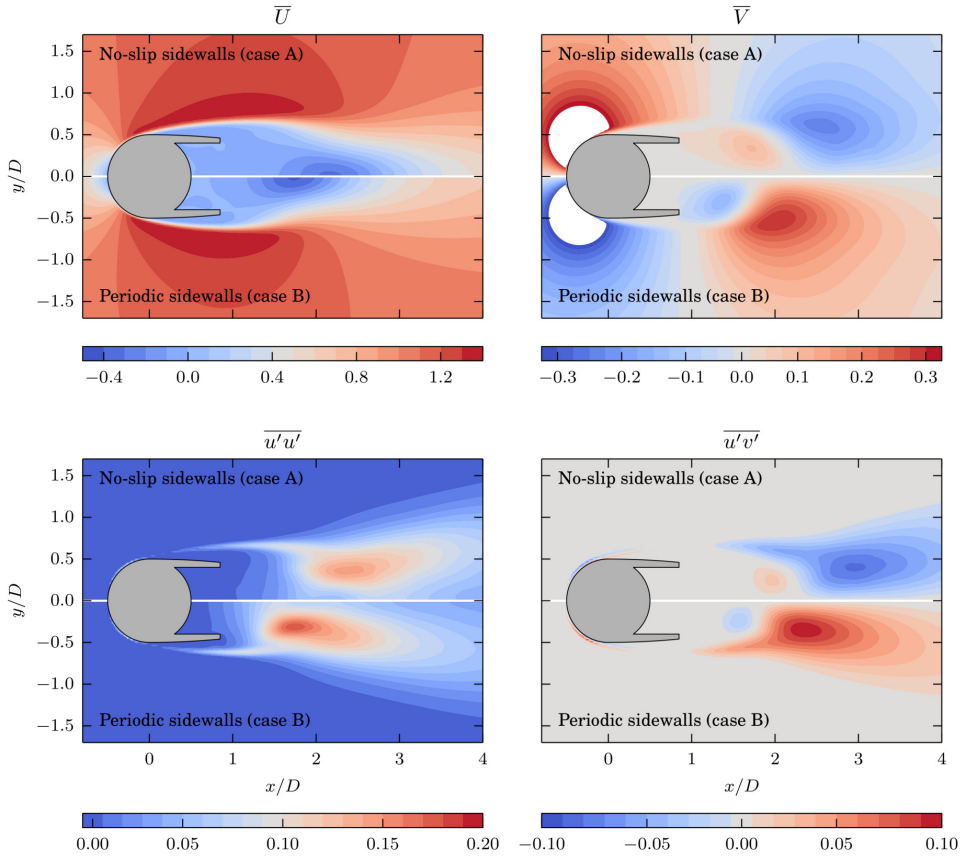

Figure 7: A slice through the center of the domain for the cases with no-slip (case A) and periodic (case B) sidewalls.

The attention can also be drawn toward the high-velocity regions above and below the cylinder in figure 7, which in these cases seems to be of both same size and magnitude. Closer inspection of the numerical values reveals that the maximum mean streamwise velocity $\overline{U}$ is about 1.34, which is a significant decrease from case B ($\overline{U} = 1.37$). Due to the nature of the contour plots in figure 7, this is not clearly visible since the difference happens to fall in between two contours.

The second-order correlations $\overline{u'u'}$ and $\overline{u'v'}$ are shown for case A and B in figure 7. The streamwise fluctuations $\overline{u'u'}$ seem to be significantly damped in the case of no-slip sidewalls, even in the center of the domain. We also see the same trend as in the mean flow plots; that the major flow structures are stretched and dragged backwards. On the other hand, the peak in the cross-correlation $\overline{u'v'}$ seems to be of about the same magnitude in both cases, and the smaller secondary peaks in $\overline{u'v'}$ also seems to be of about same strength although the positions are different.

Another interesting observation is that the wake seems to be of almost exactly equal width in the two cases in figure 7. If we follow the 'first visible' contour of any variable, i.e. the first visible contour above (or below) zero, we observe that at the end of the figure, both contours end up in the same y-coordinate.

Figure 8 shows the wake in the plane with the cylinder axis. Large regions of negative fluid velocity are seen in the regions around $z = -4D$ for the case with solid walls (case A), where both the fluctuations in the streamwise $\overline{u'u'}$ and crossflow $\overline{v'v'}$ direction are low. We also see that the general shape of the curve for $\overline{u'u'}$ in figure 4 is confirmed by this figure. Even though there is some variation due to insufficient sampling, the general location of the peaks is constant. The largest, primary peak of $\overline{u'u'}$ is located after a smaller, secondary peak closer to the cylinder, even though the field is not completely uniform along the span. It also shows that although the mean flow field statistics probably are converged, the temporal sampling of about 360 vortex shedding cycles is not enough to give uniform second order statistics in the spanwise direction in cases B and C. The statistical quality is significantly improved in the cases with periodic sidewalls by doing a spanwise average. However, in the case with no-slip walls there is no other option than sampling longer time series. This is very important to consider when planning an experiment in which only the flow in a plane is investigated, and no spanwise averaging is possible.

The streamlines of the mean flow field in a xz-plane through the center plane of the cylinder are shown in figure 8. It clearly shows that there are no regions of uniform flow that can be compared to a case with periodic conditions, as there is a mean flow in the spanwise direction along the entire cylinder span. Even though there is a symmetry plane in the middle where the mean spanwise velocity $\overline{V}$ is zero, there is no region in which the velocity field is uniform and independent of the spanwise location. The presence of the no-slip walls also leads to the formation of multiple eddies in the mean flow field, especially near the sidewalls.

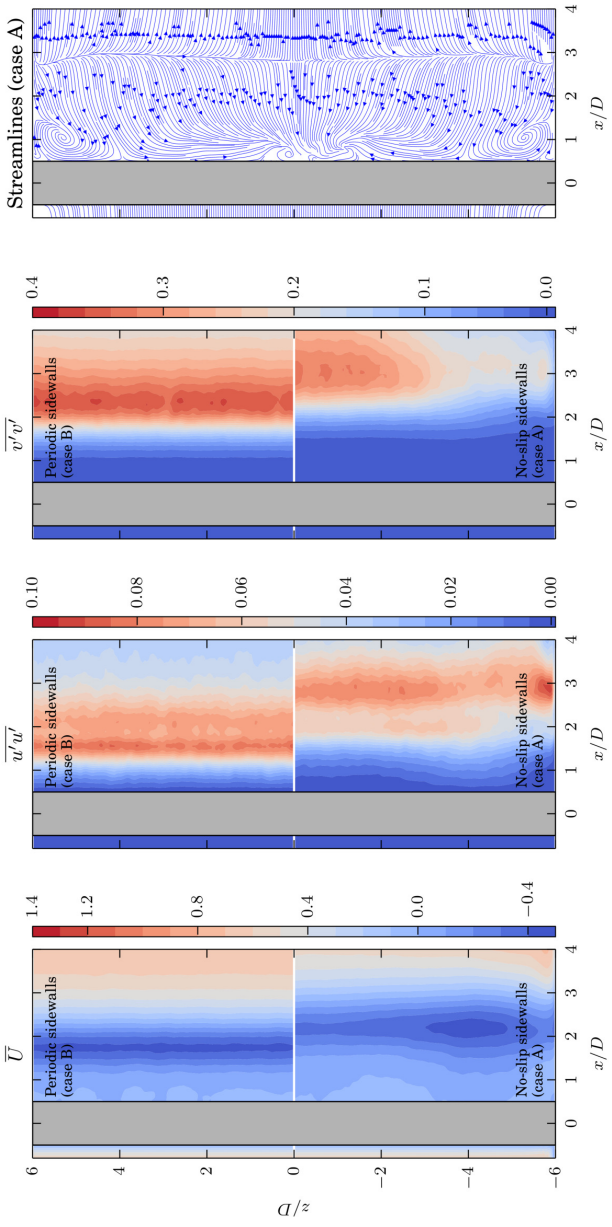

Figure 8: Slices through the cylinder axis (at $y = 0$) for the case with no-slip (case A, lower half) and periodic (case B, upper half) sidewalls. The mean flow streamlines to the far right are for the case with no-slip sidewalls (case A) and emphasis the strong 3D effects in this case.

5 CONCLUDING REMARKS

We believe that we have resolved many of the issues previously identified in our simulations on this cylinder configuration. The comparison between the LES and DNS are now in our opinion excellent, but there will always be room for further improvements. This case demonstrates that for many aspects, LES can compete with DNS in terms of large-scale accuracy for bluff body wake flows.

The most surprising result in this study is the large effect of the no-slip boundary conditions on the spanwise boundaries. This boundary condition alters the wake much more than the effect of blockage from the top and bottom walls. When going back to our previous work where we have presented results from PIV experiments [3], we also see a remarkable good agreement between our simulations with no-slip boundaries and the flow fields obtained from the experiments.

In the bitter end, it also means that at this Reynolds number, a cylinder length of $12D$ is not sufficient if one wants to study this flow experimentally. Even though this work is done on a particular cylinder with fairings, we do believe that this can be considered valid also for other similar (long and slender) geometries. It also shows that experiments do not necessarily give the correct and desired answers just because it is an experiment. Just as in a simulation, real-world physical boundary conditions influence the result in ways that are not always easy to predict.

ACKNOWLEDGEMENTS

The authors wish to thank the employees at the *Chair of Hydromechanics* at *TU München* and *KM Turbulenz GmbH* for all their help and technical support on the MGLET code. We are grateful for the comments and feedback from the two reviewers. Their effort have contributed significantly to the paper.

This work would not have been possible without the support from the computational resources at NTNU provided by NOTUR.

REFERENCES

[1] R. Baarholm, K. Skaugset, H. Lie and H. Braaten. 'Experimental studies of hydrodynamic properties and screening of riser fairing concepts for deep water applications'. In: *34th International Conference on Ocean, Offshore and Arctic Engineering*. OMAE2015-41730. St. John's, Canada, June 2015.

[2] H. Strandenes, J. P. Gallardo, B. Pettersen and H. I. Andersson. 'Comparison of LES and DNS for the flow past a cylinder with fairings'. In: *17th Numerical Towing Tank Symposium*. Marstrand, Sweeden, Sept. 2014.

[3] H. Strandenes, J. P. Gallardo, B. Pettersen and H. I. Andersson. 'A comparative study between DNS, LES and PIV for a marine riser with fairings'. In: *34th International*

Conference on Ocean, Offshore and Arctic Engineering. OMAE2015-41494. St. John's, Canada, June 2015.

[4] L. Zovatto and G. Pedrizzetti. 'Flow about a circular cylinder between parallel walls'. *Journal of Fluid Mechanics* 440 (Aug. 2001), pp. 1–25. DOI: 10.1017/s0022112001004608.

[5] D.-H. Kim, K.-S. Yang and M. Senda. 'Large eddy simulation of turbulent flow past a square cylinder confined in a channel'. *Computers & Fluids* 33 (1) (Jan. 2004), pp. 81–96. DOI: 10.1016/s0045-7930(03)00040-9.

[6] J. Chakraborty, N. Verma and R. Chhabra. 'Wall effects in flow past a circular cylinder in a plane channel: a numerical study'. *Chemical Engineering and Processing: Process Intensification* 43 (12) (Dec. 2004), pp. 1529–1537. DOI: 10.1016/j.cep.2004.02.004.

[7] Z. Huang, H. I. Andersson and W. Cui. 'End-wall effects on vortex shedding in planar shear flow over a circular cylinder'. *Computers & Fluids* 42 (1) (Mar. 2011), pp. 102–107. DOI: 10.1016/j.compfluid.2010.10.009.

[8] P. Parnaudeau, J. Carlier, D. Heitz and E. Lamballais. 'Experimental and numerical studies of the flow over a circular cylinder at Reynolds number 3900'. *Physics of Fluids* 20 (8) (2008), p. 085101. DOI: 10.1063/1.2957018.

[9] M. Manhart, F. Tremblay and R. Friedrich. 'MGLET: a parallel code for efficient DNS and LES of complex geometries'. In: *Parallel Computational Fluid Dynamics - Trends and Applications*. Ed. by C. B. Jenssen et al. Elsevier Science B.V., 2001, pp. 449–456.

[10] N. Peller, A. L. Duc, F. Tremblay and M. Manhart. 'High-order stable interpolations for immersed boundary methods'. *International Journal for Numerical Methods in Fluids* 52 (11) (2006), pp. 1175–1193. DOI: 10.1002/fld.1227.

[11] M. Manhart. 'A zonal grid algorithm for DNS of turbulent boundary layers'. *Computers & Fluids* 33 (3) (Mar. 2004), pp. 435–461. DOI: 10.1016/s0045-7930(03)00061-6.

[12] F. Nicoud and F. Ducros. 'Subgrid-scale stress modelling based on the square of the velocity gradient tensor'. *Flow, Turbulence and Combustion* 62 (3) (1999), pp. 183–200.

Attached paper II

Influence of spanwise no-slip boundary conditions on the flow around a cylinder

Håkon Strandenes, Bjørnar Pettersen, Helge I. Andersson, Michael Manhart

In: Computers & Fluids vol. 156, October 2017, pp. 48–57
DOI: 10.1016/j.compfluid.2017.06.025

Influence of spanwise no-slip boundary conditions on the flow around a cylinder

Håkon Strandenes[1], Bjørnar Pettersen[1], Helge I. Andersson[2], and Michael Manhart[3]

[1] *Department of Marine Technology, Norwegian University of Science and Technology, Otto Nielsens veg 10, 7052 Trondheim, Norway*

[2] *Department of Energy and Process Engineering, Norwegian University of Science and Technology, Kolbjørn Hejes vei 1B, 7034 Trondheim, Norway*

[3] *Professorship of Hydromechanics, Technical University of Munich, Arcisstr. 21, 80333 Munich, Germany*

Corresponding author e-mail: `hakon.strandenes@ntnu.no`

28th April 2017

Abstract

First we present high resolution large eddy simulations (LES) for the flow past a circular cylinder at Reynolds number 3900 to prove the quality of the simulations. A thorough grid convergence study is presented, and the agreement in the mean flow statistics between our simulations and the references is excellent. Then we apply a no-slip boundary condition at the spanwise boundaries of the cylinder, with aspect ratios of 6, 12 and 24. This results in large changes in the shear layers and wake topology, even for an aspect ratio of 24. Even though the boundary layers along the side walls are only about 0.4 diameters thick, they nevertheless manage to stabilize the shear layers all the way through the channel, thus effectively delaying the roll-up and transition to a turbulent wake.

Keywords: cylinder; LES; no-slip; spanwise boundary; shear layer stability

NOMENCLATURE

C_D	Drag coefficient	Q	Second invariant of ∇u
C_L	Lift coefficient	Re	Reynolds number $Re = DU_\infty/\nu$
C_{pb}	Base pressure coefficient	St	Strouhal number $St = f_v D/U_\infty$
D	Cylinder diameter	u, v, w	Instantaneous fluid velocity
f_v	Vortex shedding frequency	$\overline{U}, \overline{V}, \overline{W}$	Time-averaged fluid velocity
L	Cylinder length	u', v', w'	$u' = u - \overline{U}$ etc.
L_r	Recirculation length	U_∞	Inlet (freestream) velocity
L_v	Vortex formation length	ν	Kinematic viscosity of fluid
ω_z	Vorticity $\omega_z = \partial v/\partial x - \partial u/\partial y$	x, y, z	Cartesian coordinates
p	Pressure	$\overline{\square}$	Time-averaged
P_{uu}	Power spectral density of u-velocity	$\square^{\text{rms}}$	Root-mean-square $= \sqrt{\overline{(\square - \overline{\square})^2}}$

1 Introduction

The flow around a circular cylinder is one of the most widely studied flow cases, both experimentally and numerically. It is applicable to many physical processes, and the definition of the problem is straight-forward. For long and smooth circular cylinders in infinite fluid the solution is a function of the Reynolds number $Re = DU_\infty/\nu$ only, where D is the constant cylinder diameter, U_∞ is the far-field inflow velocity and ν is the kinematic viscosity of the fluid. The flow solution turns unsteady already around Reynolds number $Re \approx 40$ and the wake become three-dimensional when $Re \gtrsim 200$ [1].

Due to the simple problem definition and the relatively complex flow solution, together with a wide range of applications in nature, science and engineering, numerous experiments and simulations have been performed on this case. Although experiments have been performed on cylinders with lengths up to several thousand diameters [2] to completely eliminate the effect of end boundary conditions, this is currently not feasible to replicate in a simulation, even for very low Reynolds numbers. Instead, periodic boundary conditions are used to replicate an 'infinitely long' cylinder. This is an efficient numerical 'trick' to save computational effort. In real life physical experiments this is not possible, since true periodicity cannot be realized in the laboratory.

It has been known for a long time that flow around cylinders are easily influenced by the spanwise boundary conditions, even for large aspect ratios L/D. Szepessy and Bearman [3] performed experiments on cylinders with end-plates and varying distance between the plates, measuring forces and vortex shedding frequencies for the range $8000 < Re < 1.4 \times 10^5$. Norberg [2] studied the influence of very large aspect ratios, up to $L/D = 5000$ in the most extreme cases for the $50 < Re < 4 \times 10^4$. Both used end-plates to reduce the effect of the solid-wall termination of the cylinder. The specific end-plate configuration was first described by Stansby [4] who developed an optimized end-plate design to reduce the change in base suction with varying cylinder lengths. However, no other flow parameters were taken into account during this design process, i.e. no indications were given on how the end plates changes the flow and wake topology.

Zhang et al. [5] used large eddy simulation to study finite length cylinders in proximity to a symmetry plane (i.e. a frictionless surface) in the spanwise direction at $Re = 3900$. They found that the forces on the finite length cylinder was lower than in the infinite length case, with a drag reduction of up to 25%. They also found that the shear layers of the finite cylinder are more stable, leading to a delayed roll-up further downstream. Pereira et al. [6] used RANS and XLES (eXtra Large Eddy Simulation) to study the difference between periodic and symmetry-plane end-wall boundary conditions also for $Re = 3900$. They found a significant difference in integral quantities such as drag coefficient between these two types of boundary conditions. Frölich and Rodi [7] simulated a short cylinder ($L/D = 2.5$) with one end mounted on a solid wall and the other end in the freestream at $Re = 43000$ focusing on exploring the vortex dynamics on this special case. Neither of these references discuss the effect of no-slip end-wall boundary conditions for long cylinders.

Huang et al. [8] considered the end-wall effects on vortex shedding around a circular cylinder at $Re = 100$ in which they studied the difference between slip and no-slip boundary conditions on the spanwise boundaries. They found that for a cylinder of length $6D$ the effect of no-slip boundary conditions substantially altered the vortex shedding in the middle of the channel. However, their low Reynolds number and short spanwise length does not make any useful reference for a turbulent flow case.

But what happens really in an experiment when a cylinder terminate in a no-slip wall, like the wall of a wind tunnel or water tank? In this paper we present simulation results for cylinders with lengths up to 24 diameters and no-slip boundary conditions in the spanwise direction,

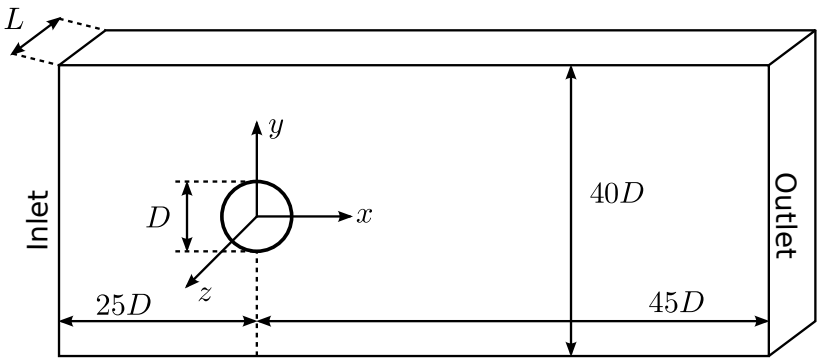

Figure 1: Computational domain and coordinate system. The origin of the coordinate system is in the center of the cylinder. The three directions are named streamwise (x-direction), crossflow (y-direction) and spanwise (z-direction). L is the length of the cylinder and width of domain. The figure is not to scale.

replicating an experimental channel with a cylinder mounted between two parallel solid walls. In addition, we have simulated a cylinder with periodic spanwise boundary conditions as a reference simulation for comparison with other published data.

We have previously studied a particular cylinder with fairings at $Re = 5000$ with both LES, DNS and PIV [9] and studied the influence of boundary conditions on this specific case and aspect ratio $L/D = 12$ [10]. In these studies we limited ourselves to one aspect ratio and one Reynolds number. The geometry we used was equipped with special fairings designed to reduce drag and the oscillating forces from vortex shedding. Since the geometry was unique and never studied before, there were no reference data available from other sources. The present paper is a follow-up on this work, where the case is generalized by removing the fairings and lowering the Reynolds number to $Re = 3900$, making it possible to compare our results with previously published data. We also increase the largest aspect ratio to $L/D = 24$ and include a lower aspect ratio of $L/D = 6$ to give a more complete description of the flow case.

2 Problem and definitions

The computational domain is shown in figure 1. The coordinate system is indicated in the figure, where the x-, y- and z-direction are the streamwise, crossflow and spanwise direction, respectively. The width of the domain equals the length of the cylinder L. All cases have a fixed-velocity inflow boundary condition at the inlet, that is $(u, v, w) = (U_\infty, 0, 0)$ and Neumann condition on the pressure ($\partial p/\partial x = 0$). The outlet condition is a fixed pressure outlet ($p = 0$) with Neumann conditions on all three velocity components. The boundary conditions in the crossflow direction

Table 1: Simulation matrix.

Simulation	per-6D	nos-6D	nos-12D	nos-24D
Cylinder length L	$6D$	$6D$	$12D$	$24D$
Spanwise BC	Periodic	No-slip	No-slip	No-slip
Number of grid cells	76×10^6	76×10^6	152×10^6	304×10^6
Min. $\Delta x/D, \Delta y/D$	0.00625	0.00625	0.00625	0.00625
Min. $\Delta z/D$	0.0125	0.0125	0.0125	0.0125

are that of a symmetry plane, this prescribe zero wall-normal velocity ($v = 0$) and Neumann conditions on all other flow quantities. For all no-slip boundaries (in the spanwise direction and on the cylinder surface) we prescribe zero velocity and a Neumann condition for the pressure.

For the cases with no-slip spanwise boundary conditions, we have simulated three aspect ratios: $L/D = 6$, $L/D = 12$ and $L/D = 24$. For the reference case with periodic conditions, we only simulated $L/D = 6$. Parnaudeau et al. [11] investigated the difference between $L/D = \pi$ and $L/D = 2\pi$ for the same Reynolds number. They found the difference to be small and concluded that a span of πD in many cases could be sufficient. With that in mind, we believe that there is no need for any longer cylinders than $L/D = 6$ when using periodic conditions. The Reynolds number is, as previously noted, $Re = 3900$ in all cases.

The different simulated cases are summarized in table 1. All simulations were run until the effects of the initial condition no longer was present. After this initial phase, statistics were sampled over 2000 D/U_∞ time units, corresponding to roughly 400 vortex shedding cycles (given a Strouhal number of $St \approx 0.2$). The reason for this large number of cycles is to achieve converged statistics along the entire span of the cylinder, without using a spanwise average.

3 Numerical methods

The code *MGLET* [12] has been used to perform all simulations presented in this paper. In short, MGLET uses a finite-volume formulation on staggered grids solving the incompressible Navier-Stokes equations using linear interpolation and integration for all spatial terms, hence leading to second-order accuracy in space. A third-order low-storage explicit Runge-Kutta time integration scheme [13] is used for time stepping.

MGLET uses a staggered Cartesian grid and introduces the solid geometry through an immersed boundary method [14]. A local refinement of the grid around the cylinder is achieved

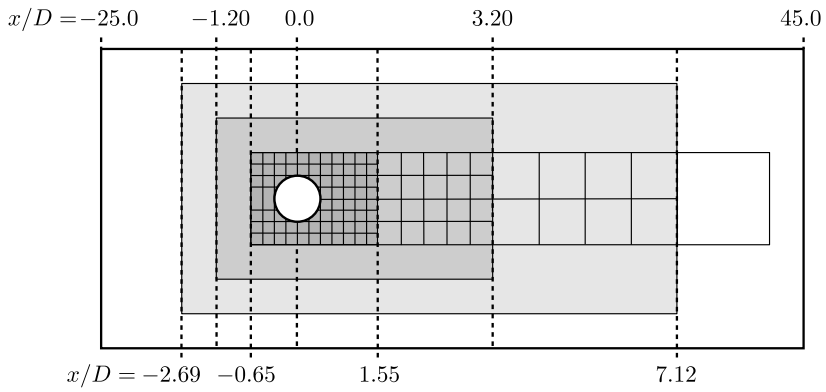

Figure 2: Schematic illustration in 2D of the grid design and refinement process. The grid refinement regions are marked with darker shades of grey for finer regions. Not to scale.

by embedding zonal grids. In the LES presented here, we used three levels of local grid refinement (plus one coarse, parent grid) around the cylinder. This resolves the cylinder, its boundary layers and the wake behind it sufficiently while keeping the total number of grid cells at a reasonable level. The refinement process is a simple cell splitting, in which each parent grid cell subject to refinement is split into eight equal (3-D) child cells [15]. A schematic illustration of the grid design is given in figure 2. The resulting smallest grid cell size is $0.00625D$ in the x- and y-direction and $0.0125D$ in the z-direction. The grid is homogeneous in the spanwise direction. The grids consist of 76, 152 and 304 million grid cells for the three aspect ratios $L/D = 6$, $L/D = 12$ and $L/D = 24$, respectively.

The time step was fixed at 0.002 D/U_∞ in all simulations, except in the initial phase where we used a smaller timestep for stability reasons, but no data was sampled from this phase. This resulted in an average maximum CFL (Courant–Friedrichs–Lewy) number of 0.77, well below half of the stability limit of the time integration method. For comparison, the results by Parnaudeau et al. [11] were simulated with a time step of 0.003 D/U_∞ and a second order time integration method. The 'Wall-Adaptive Local Eddy-viscosity' model, more commonly known as the WALE model [16], was used as the LES subgrid-scale model. The same numerical setup has also been used in other recent works, such as [17].

3.1 Grid convergence

A detailed grid convergence study has been conducted. Four different grids of similar kind but with different resolution were created and the reference periodic case simulated. The overall properties of each grid is provided in table 2. The results in figure 3 clearly show that there

Table 2: Grid convergence study setup

Simulation	coarse	medium	fine	veryfine
Cylinder length L	$6D$	$6D$	$6D$	$6D$
Spanwise BC	Periodic	Periodic	Periodic	Periodic
Number of grid cells	15×10^6	35×10^6	76×10^6	613×10^6
Min. $\Delta x/D, \Delta y/D$	0.025	0.0125	0.00625	0.00312
Min. $\Delta z/D$	0.05	0.025	0.0125	0.00625
Time step Δt	0.002	0.002	0.002	0.001
Time steps	262144	262144	262144	167580

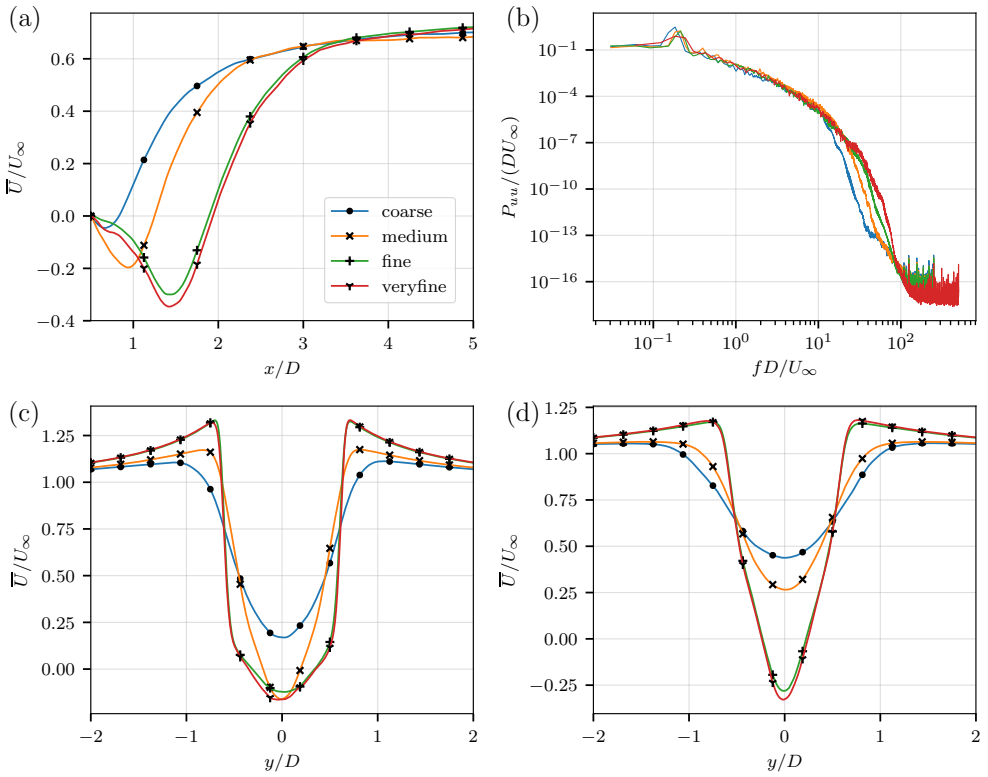

Figure 3: Results from the grid convergence study with the four grids from table 2. (a) time-averaged streamwise velocity in the centerline behind the cylinder at $y = 0$. (b) energy spectra in the point $(x, y, z) = (1.54D, 0.6D, 0.0)$ and (c) and (d) time-average streamwise velocity in two transverse lines at $x/D = 1.06$ (c) and $x/D = 1.54$ (d). All data are sampled in the centerplane at $z = 0$.

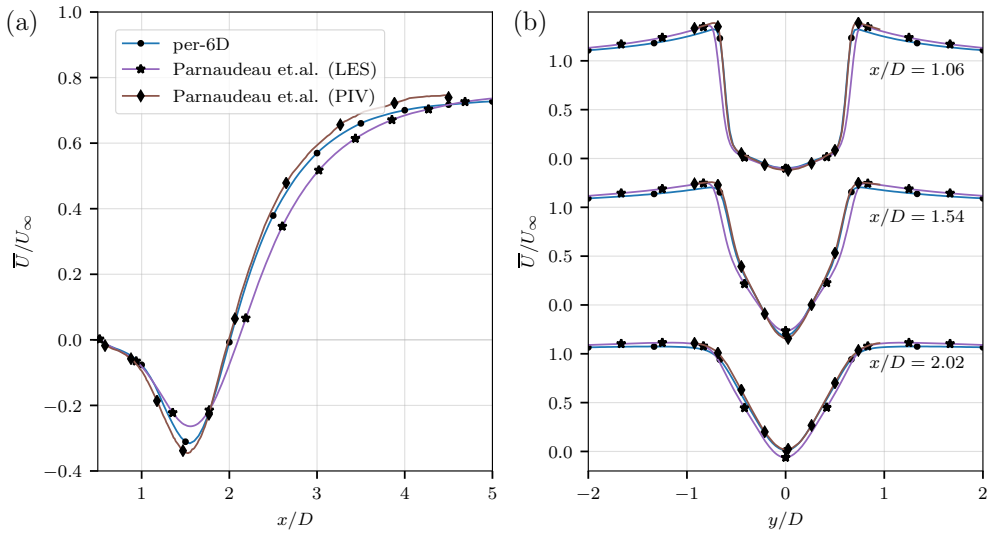

Figure 4: Comparing results from case *per-6D* with data from Parnaudeau et al. [11] (high resolution LES and PIV cases). All lines are sampled in the center plane at $z = 0$.

is only minor difference between the case *fine* and *veryfine*. Since the *veryfine* grid has more than eight times the number of cells and require a time step of half that of the *fine* grid, the computational cost of the *veryfine* grid is more than 16 times that of the *fine*. For this reason the *veryfine*-case was only run a limited time until the first order statistics were converged. The results in figure 3 are very clearly showing that the *fine* and *veryfine* case provide almost identical results. For this reason the *fine* grid was chosen for all further simulations.

3.2 Comparing with references

We have obtained the velocity profile data from Parnaudeau et al. [11]. The reference dataset contain both flow data simulated with LES and experimental data obtained by PIV (particle image velocimetry). A cylinder with end-plates was used in the experiment, and the cylinder length between the end plates were $L/D = 20$. The reference data is plotted together with (the same) data from the current simulation *per-6D* in figure 4. The reference LES dataset exhibits a somewhat higher minimum streamwise velocity at the centerline behind the cylinder, and a slightly lower velocity in the range $1.8 < x/D < 4.0$. The match between our simulations and the experimental PIV data from the same reference [11] is on the other hand excellent. In total, we consider the comparison to be satisfactory, and that all the effects discussed in the remainder of this paper will be much larger than the discrepancies seen in figure 4.

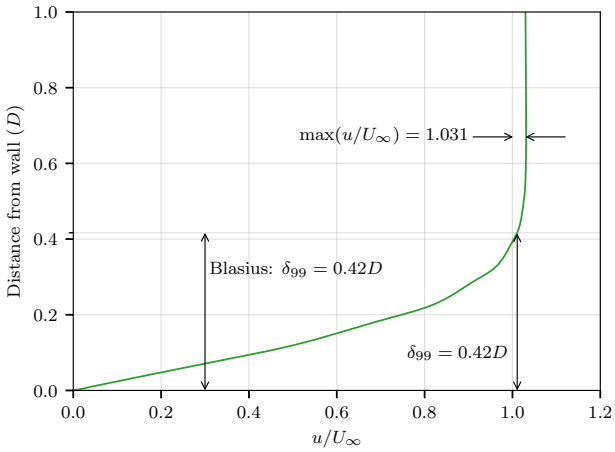

Figure 5: Illustration of boundary layer profile $\overline{U}$ in the empty channel corresponding to case *nos-12D* at position $x = 0$. The Blasius boundary layer thickness defined as the location where $u/U_\infty = 0.99$ is indicated on the figure. The actual boundary layer thickness, defined as the location in which the velocity approach 99% of the value in the center of the channel, is also indicated as δ_{99}. The boundary layer is resolved by approximately 34 grid cells.

3.3 Simulation without body

A parameter in the simulations with the no-slip spanwise boundary conditions is the nature of the boundary layer in the vicinity of the cylinder. If we position the cylinder closer to the (uniform) inlet, it 'sees' a thinner boundary layer compared to a cylinder placed further away. Since the boundary layer is laminar, we can make an estimation of the boundary layer shape based on a Blasius profile. However, due to the coarse grid near the channel inlet the boundary layer profile will deviate from the ideal Blasius solution. In addition, we have a blockage effect due to the displacement of the boundary layers which will contribute to increase the velocity in the center of the domain.

We have performed a simulation with an empty channel, that is without any cylinder present. We used the domain from the intermediate length cylinder case ($L/D = 12$). In this way, we can see how the boundary layers develop without the interference from the cylinder. A velocity profile taken at the location of the cylinder ($x = 0, y = 0$) is presented in figure 5. This shows that there is a large region of nearly uniform velocity u in almost the entire cross-section. The velocity at the center is slightly larger than the inlet velocity U_∞ by about 2.1%. When approaching the walls, the velocity increases from the value in the center of the channel, up to a maximum of 3.1% larger than the inflow velocity $0.67D$ from the wall (indicated in the figure 5 with both position and magnitude). The boundary layer thickness predicted by a Blasius profile for this

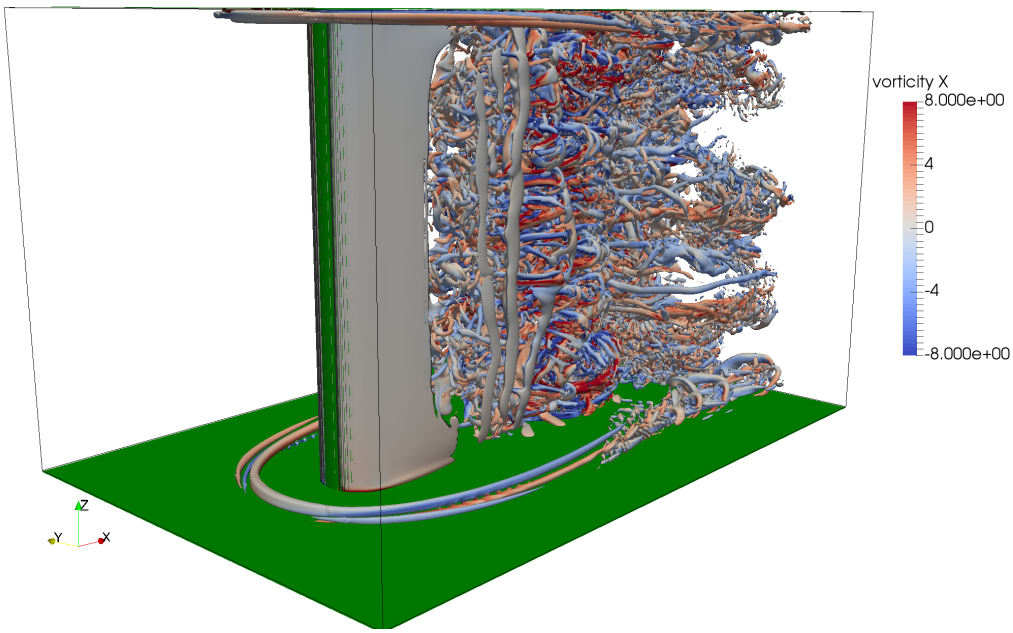

Figure 6: Instantaneous view of the flow field for the 'nos-6D' case showing the cylinder wake and horseshoe vortex system. The solid green surfaces indicate the no-slip boundary conditions on the cylinder itself and the side walls. The isosurfaces are computed for $Q = 2.0$ and coloured by the streamwise vorticity $\omega_x D/U_\infty$.

location in the tank is $\delta_{99} \approx 0.42D$. When we define our boundary layer thickness as the location in which the velocity reach 99 % of the velocity in the center of the channel, we get a computed boundary layer thickness of $\delta_{99} \approx 0.42D$, which happens to be exactly the same as predicted by the Blasius profile.

In total, it seems like the simulation is representing a physical channel flow. The velocity profile is not completely uniform, but in laboratory experiments this will never be the case either. Since the velocity increase in the middle of the channel is small, to keep it simpler, we will normalize all velocities with respect to the inlet velocity U_∞ instead of using the actual velocity in the center of the channel.

4 Results

To give an overview of the flow topology for the cases with no-slip boundary conditions, the Q-criterion was computed for the case 'nos-6D' and is shown in figure 6. The most important feature compared to the flow around an infinitely long cylinder, is the horseshoe vortex system

Table 3: Main flow coefficients. The symbols are explained in the nomenclature in the beginning of the paper. The characteristics from [11] are from the high-resolution LES case and the data from [18] are from 'run 7'. Recirculation length and vortex formation length are measured from the base of the cylinder.

Simulation	per-6D	nos-6D	nos-12D	nos-24D	Ref. [11]	Ref. [18]
St	0.212	0.196	0.208	0.210	0.208	0.210
$\overline{C_D}$	0.968	0.867	0.897	0.904		
C_D^{rms}	0.0258	0.0116	0.0093	0.0123		
C_L^{rms}	0.1249	0.0076	0.0235	0.0224		
$-\overline{C_{pb}}$	0.865	0.699	0.747	0.763		0.900
L_r/D	1.508	2.987	2.250	2.061	1.56	1.198
L_v/D	0.872	2.814	1.615	2.003	0.92	
$U_{\min}/U_\infty$	-0.316	-0.389	-0.285	-0.271	-0.26	-0.28

developing around the intersection between the solid wall and cylinder. The figure shows a laminar horseshoe vortex forming around the cylinder, which turns turbulent around $x/D = 3.0$. This point of transition is significantly further downstream than the point of transition in the shear layers separating from the cylinder. The same principle flow configuration with a horseshoe vortex is present in all no-slip cases even though they are not all shown here.

The main flow characteristics and force coefficients are summarized in table 3. The force coefficients presented here are measured and averaged over the entire span of the cylinder. A practical consequence of this is that the ends of the cylinder are within the wall boundary layer in the cases with no-slip boundaries, and consequently the force coefficients are affected by this. The largest difference between the cases with- and without the no-slip spanwise boundary is that the RMS of the lift coefficient C_L^{rms} is dramatically lower in the cases with no-slip boundary condition, compared to the periodic case.

The Strouhal number is calculated based on the time history of the fluid velocity u and v in position $(x, y, z) = (3.0D, 0.45D, 0)$ in the wake. The base pressure coefficient is based on the mean pressure difference between a point immediately behind the cylinder (at $x = 0.5D$) in the center of the domain and a corresponding point upstream at $x = -20D$. For the cases with no-slip boundary conditions, the presence of the no-slip walls will lead to a pressure drop along the channel that will affect the base pressure coefficient.

Figure 7 shows the time-averaged streamwise and spanwise velocities in a slice through $y = 0$. The first important point is that the velocities are nearly perfectly symmetric ($\overline{U}$) and antisymmetric ($\overline{V}$) in the z-direction, which mean that the statistics are well converged

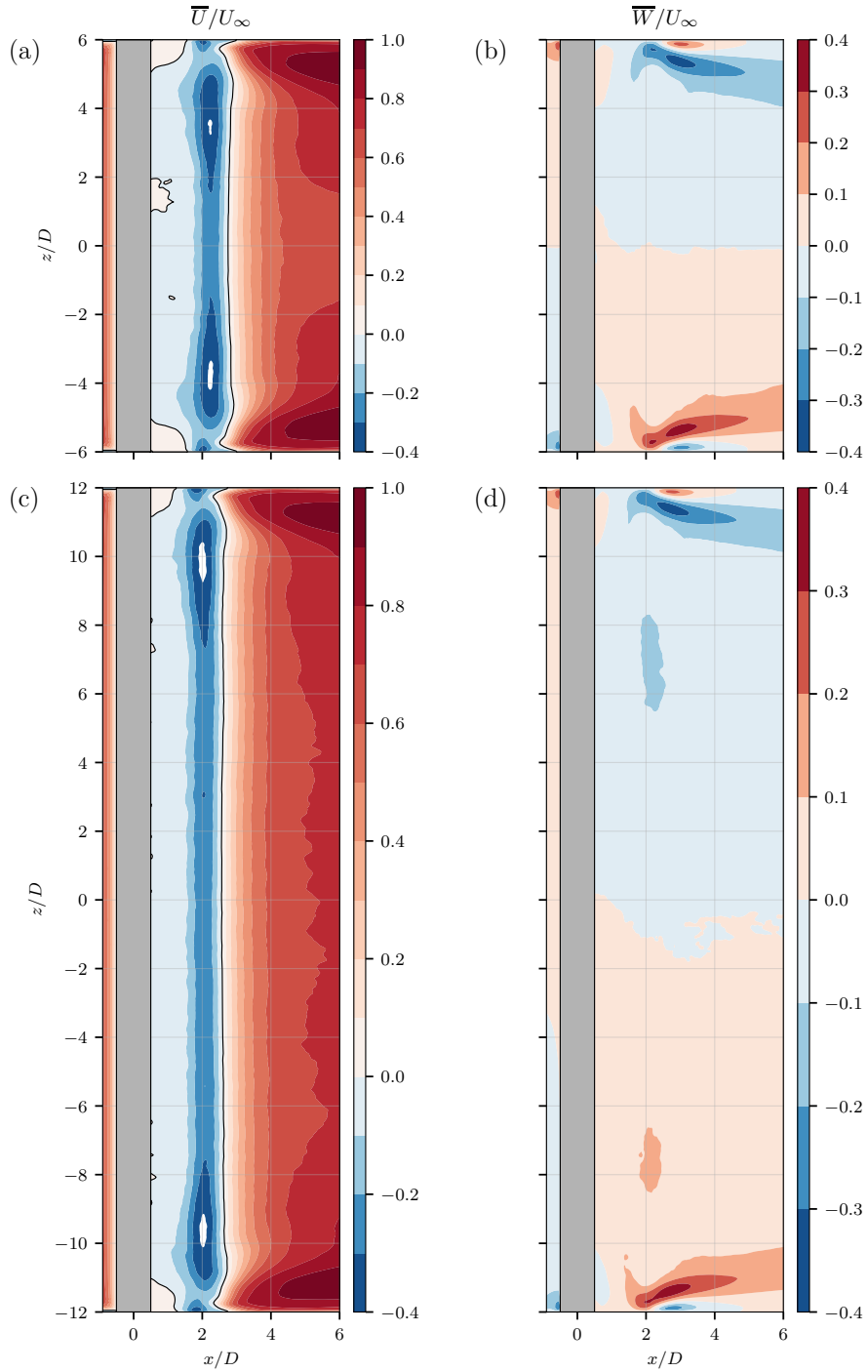

Figure 7: Time-average streamwise (a, c) and spanwise (b, d) velocity in a slice through $y = 0$ for the cases *nos-12D* (a, b) and *nos-24D* (c, d). White regions are regions where the velocity exceed the defined color scale indicated on the colorbar. Blue colors are negative velocities and red colors are positive velocities. The solid black line in plots (a, c) indicate the contour $\overline{U} = 0$.

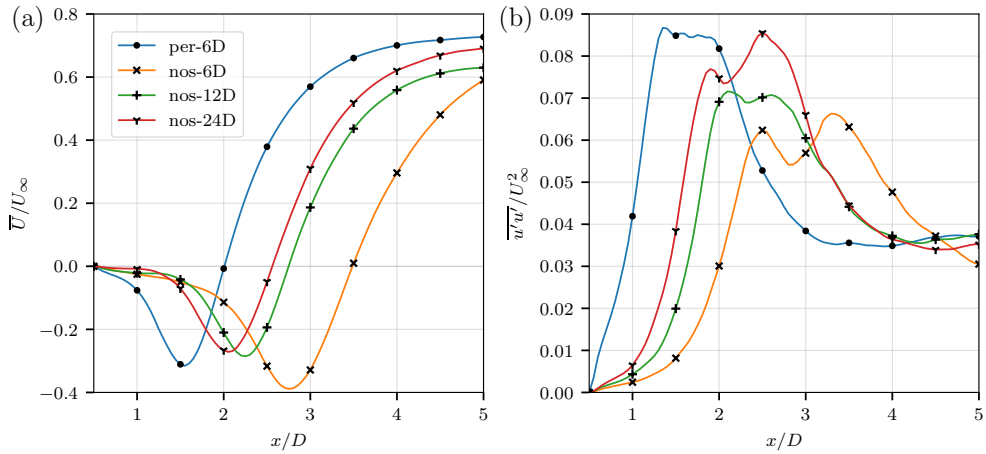

Figure 8: Profiles of mean velocity $\overline{U}$ (a) and $\overline{u'u'}$ (b) along the center line behind the cylinder. The origin of the x-axis is in the center of the cylinder. The lines are sampled in the center of the domain at $z = 0$.

throughout the channel. Secondly, the figure shows that the walls have a significant effect on the mean flow around the cylinder. The extent of the influence is much wider than the boundary layer thickness δ_{99}, from the previous chapter we recall that this is only about $0.4D$. From figure 6 we also recall that the horseshoe vortex system is confined to a region very close to the wall, typically less than $1D$ away. Despite this, the influence of the wall reaches all the way into the channel for the *nos-12D* case as seen in figure 7 (a). The mean streamwise velocities on the other hand, are influenced by the wall up to about $4D$ from the wall. The spanwise velocities have significant non-zero values up to $2D$ away from the walls. In the center of the channel, there is also a wide region with nearly 2-D flow statistics, this region is also about $4D$ wide. This region of influence from the walls is increasing quickly downstream in the wake.

Stäger and Eckelmann [19] studied the thickness of the wall-affected region on a cylinder with various end-plate diameters. If we use their data (provided in [19] figure 9) and assume that our setup is similar to an endplate with diameter $25D$ (the same as the distance from the cylinder to the inflow boundary in the present study), we find that the thickness of the wall-affected region is between $5D$ and $6D$. This fits nicely within both figure 7 (a) and (c). Despite that we see a large region with 2-D flow statistics in figures 7 (c) and (d), the flow is still strongly influenced by the wall throughout the entire domain. The notion of a certain 'wall-affected' region is thus in our opinion misleading.

Figure 8 present the mean streamwise velocity in the centerline behind the cylinder, in the

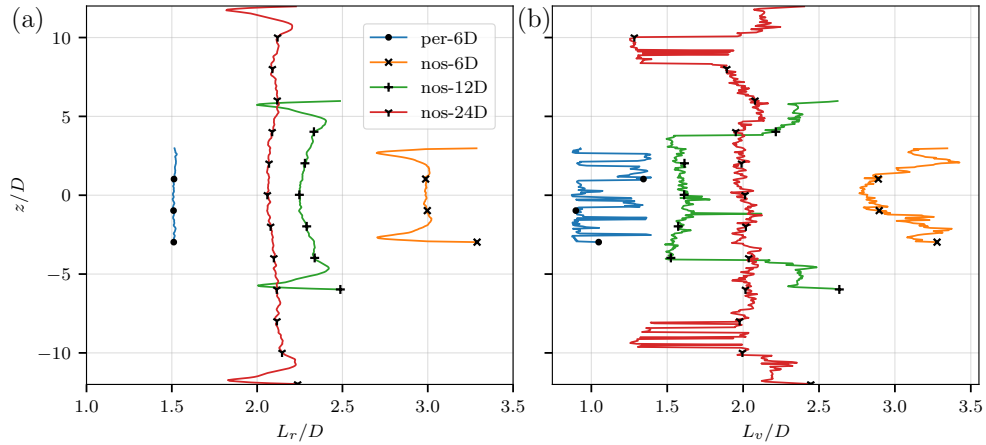

Figure 9: Profiles on how the recirculation length L_r (a) and vortex formation length L_v (b) vary along the span of the cylinder for the different cases.

middle of the domain (at $y = 0$ and $z = 0$) for all simulated cases. This figure shows the major impact of the no-slip boundary condition. All characteristic points, like the recirculation length (the distance from the base of the cylinder to the the point where $\overline{U}$ turns positive) and vortex formation length (the distance from the base of the cylinder to the maximum of $\overline{u'u'}$) is longer by $0.5D$ to $1D$ for all no-slip cases compared to the periodic case.

Another interesting feature is that there is no sign of immediate convergence towards the periodic reference case. Even the *nos-24D* case deviate significantly from the *per-6D* case. We believe that a cylinder length of more than $100D$ is needed before the results are comparable with the periodic reference case. This argument can be made because the difference between the *nos-12D* and *nos-24D* cases are quite small compared to the difference with the *per-6D* case, and hence no sudden convergence can be expected.

The recirculation length and vortex formation length are extracted from every grid cell location in the z-direction along the cylinder span, and plotted in figure 9. Again we see large differences between the cases, even between the $24D$ length cylinder and the periodic case. The recirculation length increase from about $1.5D$ to about $2.1D$ in the center of the channel going from the periodic case to the *nos-24D* case. Both quantities vary only marginally along the cylinder span, and there are huge regions in the center of the channels where these quantities do not change at all. The trend we have commented on earlier is also still present, i.e change from the *nos-12D* to *nos-24D* case is much smaller than the difference compared to the *per-6D* case.

Ma et al. [20] discussed the shape of the streamwise velocity profiles in the very near wake,

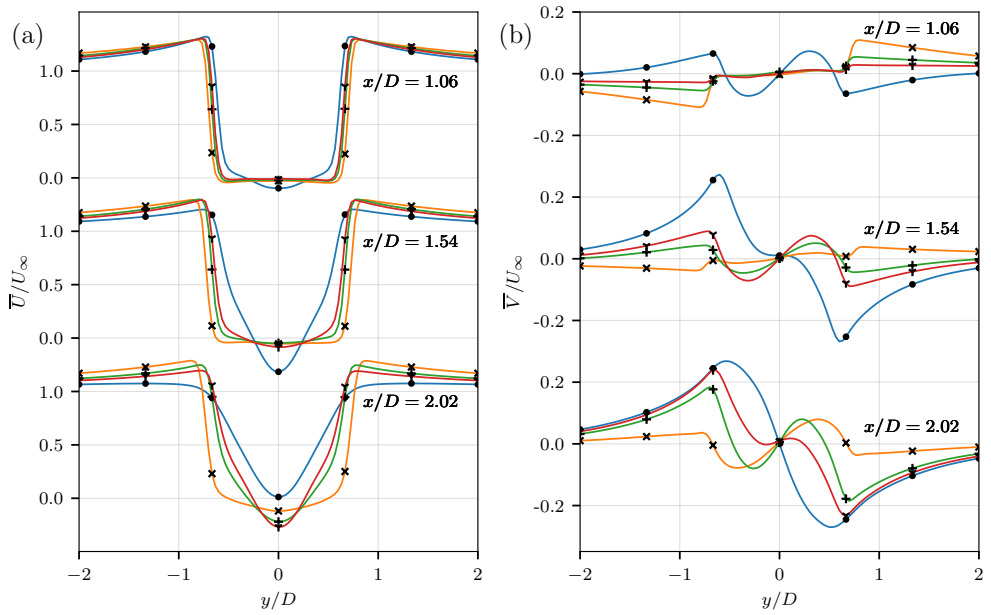

Figure 10: Time-averaged streamwise (a) and crossflow (b) velocity in the wake behind the cylinder at three different locations at $z/D = 0$. For legend, see figures 8 - 9.

and how very small changes in the simulation setup, such as the length of the cylinder and inflow turbulence intensity can trigger a change from a U-shaped velocity profile to a V-shaped velocity profile. Tremblay [21], on the other hand, demonstrated how insufficient sampling can influence the shape of the velocity profiles in the wake, and comment that a lot of the previously published data in this field are probably sampled over too few shedding cycles.

We have plotted the same velocity profiles at the same locations in figure 10. At the nearest section, at $x/D = 1.06$, the shape of the profile is nearly square for all cases with no-slip boundary conditions, with very high crossflow gradients of the mean velocity. The periodic reference case shows a more U-shaped profile. In the middle section at $x/D = 1.54$ the periodic case has turned into a V-shaped profile, the *nos-6D* case is still a square profile and the *nos-24D* case is more like a U-shape. At the section furthest away, all profiles, except the $6D$ case, are clearly V-shaped.

The shear layers forming behind the cylinder is shown in the plot of spanwise vorticity $\overline{\omega_z} D/U_\infty$ in figure 11 for both time averaged and instantaneous values. This figure indicates that the shear layers of the cases with no-slip sidewalls are more stable than in the periodic case. This enhanced stability leads to a delay of the roll-up of the shear layer vortices and subsequent breakdown. If we compare the location of the last negative or positive vorticity contour before

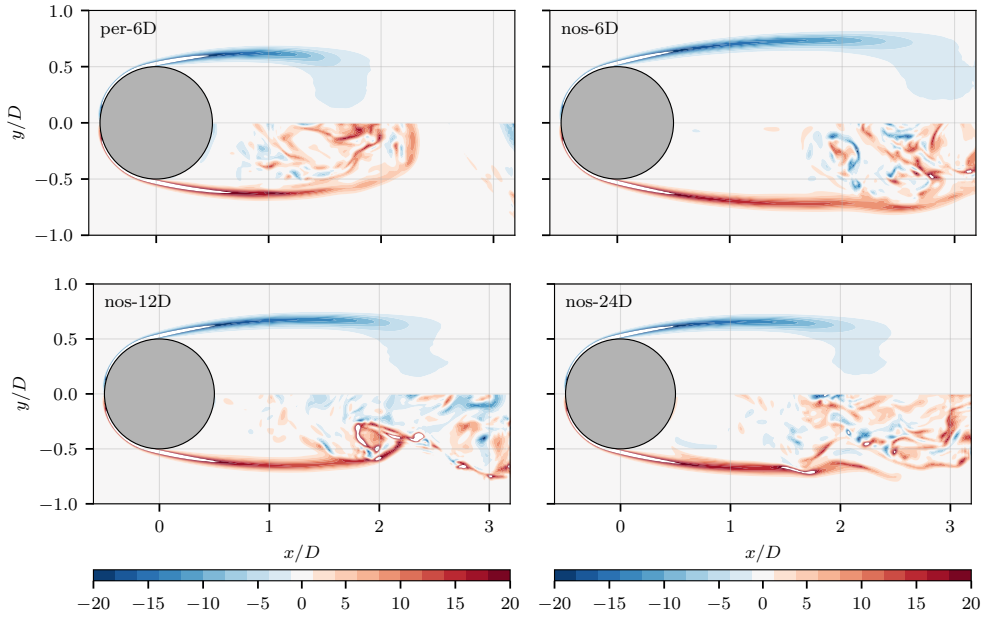

Figure 11: Split view plot: Time-averaged vorticity $\overline{\omega_z} D/U_\infty$ on the top half in each panel, and instantaneous spanwise vorticity $\omega_z D/U_\infty$ in the lower half. Both quantities are sampled in the center of the domain at $z = 0$. The instantaneous values are not in phase with each other and are from the last computed timestep of each simulation.

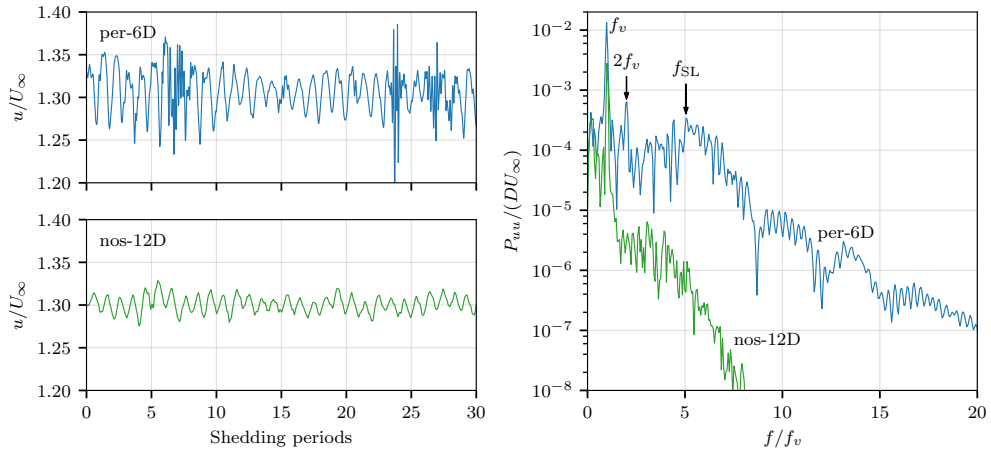

Figure 12: Left: Time traces of instantaneous streamwise velocity u in a point $(x, y, z) = (1.0, 0.8, 0.0)$ shown for 30 vortex shedding cycles. Right: Power spectral density computed with Welch's method [22] of the velocity measurement. The peak corresponding to the shear layer instability is marked f_{SL}.

the white region around the zero contour, we see that this contour extends all the way down to $x/D = 2.5$ in the *nos-24D* case, while in the periodic case this contour stops at $x/D = 1.8$. We also see that the regions with very high vorticity, above and below the color scale in this figure (pure white regions), are more or less of identical shape and size.

To show how the no-slip boundary condition stabilizes the shear layers, we conducted two additional simulations where we sampled the time trace of the velocity in discrete points for the *per-6D* and *nos-12D* cases. The sampling was over slightly more than 40 vortex shedding cycles. The time traces of the streamwise velocity u is shown in figure 12 for the 30 first cycles. We also computed the power spectral density for both time series. The velocity measurements for the case *per-6D* clearly show the same intermittent high-frequency bursts as discussed by Prasad and Williamson [23]. These high-frequency bursts occur at irregular intervals, with frequencies significantly higher than the vortex shedding frequency. The *nos-12D* case does not show any such features at all. The power spectra also shows that the case with no-slip boundary condition contains almost no energy for frequencies higher than the vortex shedding frequency. The *per-6D* case show a distinct high-energy region around $f/f_v = 5$ corresponding to the shear layer instability frequency f_{SL}, and a peak at $f/f_v = 2$ corresponding to the first harmonic of the shedding frequency. Neither of them is visible in the spectrum for the *nos-12D* case. In summary, the power spectrum for the *nos-12D* case is clearly much more narrow-banded than the *per-6D* case at this location in the wake.

5 Concluding Remarks

Our simulations show that even for long cylinders, placement of the cylinder in a channel with no-slip boundary conditions along the walls (e.g. a circulating water tunnel, wind tunnel etc.) gives huge impacts on the flow, also in the centre of the channel, far from the wall boundary layers.

The shear layers forming behind the cylinder are considerably more stable in the simulation with the no-slip walls, and this delays the roll-up and formation of the turbulent wake. This is seen both on the mean and instantaneous vorticity and on the time-trace of a velocity sampling just outside of the shear layer. For the case with no-slip walls there is significantly less energy content for higher frequencies compared to the case with periodic boundary conditions. These effects must be considered when designing experiments and also when comparing experimental and simulation results.

Another important result is that we showed that even though there is large regions of two-dimensional flow statistics in the center of the channel, this is not alone enough to claim that the results are independent of the aspect ratio or free of any end-wall effects. Our *nos-24D* case show that even tough there is a 12D wide region of 2-D flow statistics in the center of the channel, the flow statistics there are not representative for the reference case with periodic boundary conditions, i.e. for an infinitely long cylinder.

6 Attached animation

An animation of the shedding process in the periodic case is attached to the electronic version of this paper. The data and time series are the same as shown in figure 12. The reason for the high-frequency bursts are much more clearly visible in this animation than in the still images in figure 11. The black crosses in the animation indicate the position of the velocity sampling.

7 Acknowledgments

The authors wish to thank the employees at *KM Turbulenz GmbH* for all their help and technical support on the MGLET code. Computing time was granted by the *Leibniz Computing Center* (LRZ) of the *Bavarian Academy of Sciences* under project *pr84gi* and UNINETT Sigma2 under project *nn9191k*. We appreciate the effort of P. Parnadeau, J. Carlier, D. Heitz and E. Lamballais

for making the data from [11] available to us in numerical form.

The constructive suggestions and tips from the anonymous reviewers was crucial to improve the quality of the final paper.

References

[1] B. M. Sumer and J. Fredsøe. *Hydrodynamics Around Cylindrical Structures*. Advanced Series on Ocean Engineering. World Scientific, 2006. ISBN: 9812700390.

[2] C. Norberg. 'An experimental investigation of the flow around a circular cylinder: influence of aspect ratio'. *Journal of Fluid Mechanics* 258 (Jan. 1994), pp. 287–316. DOI: 10.1017/S0022112094003332.

[3] S. Szepessy and P. W. Bearman. 'Aspect ratio and end plate effects on vortex shedding from a circular cylinder'. *Journal of Fluid Mechanics* 234 (Jan. 1992), pp. 191–217. DOI: 10.1017/S0022112092000752.

[4] P. Stansby. 'The effects of end plates on the base pressure coefficient of a circular cylinder'. *Aeronautical Journal* 78 (Jan. 1974), pp. 36–37. DOI: 10.1017/S0001924000036319.

[5] H. Zhang, J.-M. Yang, L.-F. Xiao and H.-N. Lü. 'Large-eddy simulation of the flow past both finite and infinite circular cylinders at Re= 3900'. *Journal of Hydrodynamics, Ser. B* 27 (2) (2015), pp. 195–203. DOI: doi:10.1016/S1001-6058(15)60472-3.

[6] F. S. Pereira, G. Vaz and L. Eca. 'Flow past a circular cylinder: a comparison between RANS and hybrid turbulence models for a low Reynolds number'. In: *34th International Conference on Ocean, Offshore and Arctic Engineering*. OMAE2015-41235. St. John's, Canada, June 2015.

[7] J. Fröhlich and W. Rodi. 'LES of the flow around a circular cylinder of finite height'. *International Journal of Heat and Fluid Flow* 25 (3) (2004), pp. 537–548. DOI: doi.org/10.1016/j.ijheatfluidflow.2004.02.006.

[8] Z. Huang, H. I. Andersson and W. Cui. 'End-wall effects on vortex shedding in planar shear flow over a circular cylinder'. *Computers & Fluids* 42 (1) (Mar. 2011), pp. 102–107. ISSN: 0045-7930. DOI: 10.1016/j.compfluid.2010.10.009.

[9] H. Strandenes, J. P. Gallardo, J. Visscher, B. Pettersen, H. I. Andersson, H. Lie and R. Baarholm. 'A comparative study between DNS, LES and PIV for a marine riser with fairings'. In: *34th International Conference on Ocean, Offshore and Arctic Engineering*. OMAE2015-41494. St. John's, Canada, June 2015.

[10] H. Strandenes, J. P. Gallardo, B. Pettersen and H. I. Andersson. 'On the Effect of Boundary Conditions on the Flow around a Cylinder in a Channel'. In: *Proceedings of MekIT'15 Eighth National Conference on Computational Mechanics*. Ed. by B. H. Skallerud and H. I. Andersson. International Center for Numerical Methods in Engineering (CIMNE), 2015, pp. 343–357. ISBN: 97884944244-96.

[11] P. Parnaudeau, J. Carlier, D. Heitz and E. Lamballais. 'Experimental and numerical studies of the flow over a circular cylinder at Reynolds number 3900'. *Physics of Fluids* 20 (8) (2008), p. 085101. ISSN: 1070-6631. DOI: 10.1063/1.2957018.

[12] M. Manhart, F. Tremblay and R. Friedrich. 'MGLET: a parallel code for efficient DNS and LES of complex geometries'. In: *Parallel Computational Fluid Dynamics - Trends and Applications*. Ed. by C. B. Jenssen et al. Elsevier Science B.V., 2001, pp. 449–456.

[13] J. H. Williamson. 'Low-storage Runge-Kutta schemes'. *Journal of Computational Physics* 35 (1) (Mar. 1980), pp. 48–56. DOI: 10.1016/0021-9991(80)90033-9.

[14] N. Peller, A. L. Duc, F. Tremblay and M. Manhart. 'High-order stable interpolations for immersed boundary methods'. *International Journal for Numerical Methods in Fluids* 52 (11) (Apr. 2006), pp. 1175–1193. ISSN: 1097-0363. DOI: 10.1002/fld.1227.

[15] M. Manhart. 'A zonal grid algorithm for DNS of turbulent boundary layers'. *Computers & Fluids* 33 (3) (Mar. 2004), pp. 435–461. ISSN: 0045-7930. DOI: 10.1016/s0045-7930(03)00061-6.

[16] F. Nicoud and F. Ducros. 'Subgrid-scale stress modelling based on the square of the velocity gradient tensor'. *Flow, Turbulence and Combustion* 62 (3) (Sept. 1999), pp. 183–200. DOI: 10.1023/A:1009995426001.

[17] W. Schanderl and M. Manhart. 'Reliability of wall shear stress estimations of the flow around a wall-mounted cylinder'. *Computers & Fluids* 128 (2016), pp. 16–29. DOI: doi.org/10.1016/j.compfluid.2016.01.002.

[18] B. N. Rajani, A. Kandasamy and S. Majumdar. 'LES of flow past circular cylinder at Re = 3900'. *Journal of Applied Fluid Mechanics* 9 (3) (2016), pp. 1421–1435.

[19] R. Stäger and H. Eckelmann. 'The effect of endplates on the shedding frequency of circular cylinders in the irregular range'. *Physics of Fluids A: Fluid Dynamics* 3 (9) (1991), pp. 2116–2121. DOI: 10.1063/1.857894.

[20] X. Ma, G.-S. Karamanos and G. E. Karniadakis. 'Dynamics and low-dimensionality of a turbulent near wake'. *Journal of Fluid Mechanics* 410 (May 2000), pp. 29–65. DOI: 10.1017/S0022112099007934.

[21] F. Tremblay. 'Direct and large-eddy simulation of flow around a circular cylinder at subcritical Reynolds numbers'. PhD thesis. Technische Universität München, 2001.

[22] P. D. Welch. 'The use of fast Fourier transform for the estimation of power spectra: A method based on time averaging over short, modified periodograms'. *IEEE Transactions on audio and electroacoustics* 15 (2) (June 1967), pp. 70–73. DOI: 10.1109/TAU.1967.1161901.

[23] A. Prasad and C. H. Williamson. 'The instability of the shear layer separating from a bluff body'. *Journal of Fluid Mechanics* 333 (Feb. 1997), pp. 375–402. DOI: 10.1017/S0022112096004326.

Attached paper III

Efficient and adaptive Cartesian mesh generation and flow initialization for DNS

Håkon Strandenes, Fengjian Jiang, Florian Schwertfirm, Bjørnar Pettersen, Helge I. Andersson

Submitted to an international journal, September 2018.

Attached paper IV

Near-wake of an inclined 6:1 spheroid at Reynolds number 4000

Håkon Strandenes, Fengjian Jiang, Bjørnar Pettersen, Helge I. Andersson

Accepted for publication in AIAA Journal, December 2018
DOI: 10.2514/1.J057615

Near-wake of an inclined 6:1 spheroid at Reynolds number 4000

Håkon Strandenes[1], Fengjian Jiang[1], Bjørnar Pettersen[1], and Helge I. Andersson[2]
[1]*Department of Marine Technology,*
[2]*Department of Energy and Process Engineering*
[1,2]*Norwegian University of Science and Technology, NO-7491 Trondheim, Norway*
Corresponding author e-mail: fengjian.jiang@ntnu.no

The flow around a 6:1 prolate spheroid at 45° inclination angle and Reynolds number 4000 based on the minor axis is described. Despite that the inflow is uniform and steady, the resulting wake is highly asymmetric and unsteady. Two main vortical structures develop from the shear layers of the spheroid, one being significantly stronger than the other. This asymmetry results in a non-zero sideforce. The forces acting on the spheroid change dramatically from earlier works at Reynolds number 3000. The pressure inside the vortex cores also change with this moderate increase in Reynolds number. This indicates that the flow is highly transitional. It is also documented that, that close to the body, on the side of the weaker vortex, there is a region of negative axial velocity. In this backflow region, fluid enters from behind the spheroid and travels forward against the inflow and then exits the backflow region through one of the main vortical structures. This backflow has not been described before. A distinct Kelvin-Helmholtz shear-layer instability close to this region is also observed and described.

Nomenclature

λ	Aspect ratio $\lambda = L : D$	F_i	Force on spheroid, $i \in (x, y, z)$
λ_2	Vortex identification measure	f	Frequency
ν	Kinematic viscosity of fluid	L	Spheroid length
ρ	Density of fluid	M_i	Torque on spheroid around the axis i, $i \in (x, y, z)$
ω	Vorticity	p	Instantaneous pressure
A_{ref}	Reference area	$\overline{p}$	Time-averaged pressure
C_{Fi}	Force coefficient, $i \in (x, y, z)$	Re_D	Reynolds number $Re = DU_\infty/\nu$
C_{Mi}	Torque coefficient, $i \in (x, y, z)$	u, v, w	Instantaneous fluid velocity
C_p	Pressure coefficient	U_∞	Inlet (freestream) velocity
D	Spheroid diameter	x_{ax}	Spheroid major axis
d	Reference length $d = 1.817D$	x, y, z	Cartesian coordinates

I. Introduction

The 6:1 prolate spheroid serves as a model for various objects ranging from particles suspended in a fluid, underwater vehicles or submarines in the ocean to aircraft, rockets and drones in the air. Different aspect ratios and attack angles, give rise to a wide range of interesting flow features such as 3-D flow separation, wake asymmetry, etc. Therefore, laboratory experiments and numerical simulations of the flow around a prolate spheroid and its wake have become an appealing research topic for flow physicists and engineers. The intrinsic complexity of the flow physics in the wake also makes it an interesting case for high-resolution flow simulations (Direct Numerical Simulations - DNS).

The prolate spheroid geometry has been used to study boundary layer separation, see e.g. Wang [1] and Geissler [2]. Flow separation experiments are reported by Wetzel et al. [3]. Later on, more complicated experiments with 3-D flow measurements took place [4]. Due to the similarity with various vehicles, the prolate spheroid has also been used as prototype in manoeuvring experiments (e.g. Rhee and Hino [5]). The full history on this topic is properly summarized in Simpson [6] and Andersson et al. [7], therefore it will not be repeated here. Nevertheless, it is important to notice that in early research works, emphasis was on the integral body forces and flow details close to the geometry (essentially surface flow, boundary layers, separation, or in special cases the very near wake). Difficulties in measuring the complex wake in an experiment, the use of simplified numerical methods, as well as limited computational power, have all been constraints in earlier studies of the wake field behind a prolate spheroid. This is to a certain degree still the case.

DNS, however, is able to produce reliable and detailed results of the 3-D flow fields, and in-depth investigations of the complex wake is possible from the simulation data. DNS studies of the prolate spheroid wake were carried out by El Khoury et al. [8, 9], in which they described the detailed wake flow behind a 6:1 prolate spheroid in cross-flow, and outlined the special flow features and the wake transition scenario for this configuration. The wake of the prolate spheroid in cross-flow contains geometrical features similar to both finite-length cylinder wakes and wakes behind spheres, but turns out to be different from both.

The wake behind a 6:1 prolate spheroid, but at angle of attack 45°, were systematically investigated by Jiang et al. [10–12]. A wide range of Reynolds numbers (Re_D, defined based on the minor axis D) from 50 to 3000 were considered. These studies reveal that the dominating structure of the laminar wake when $Re_D < 1000$ is a pair of counter-rotating vortices. These vortices originate from the shear layers separated from the two sides of the spheroid, starting at the tip of the spheroid while growing larger downstream. This steady and fully symmetric laminar wake persists to a relatively high $Re_D = 1000$, at which the primary instability was observed, and the wake partly looses its symmetry (in the far wake only). At Reynolds numbers higher than about 1000, the wake becomes unsteady and asymmetric, but no vortex shedding or vortex filament flapping could be observed in the wake. As a result, the time-averaged flow field is also heavily asymmetric, thus exerts a strong side force onto the geometry.

The asymmetric time-averaged flow fields, together with the strong side force, deliver an important message. People have only considered this kind of asymmetric wake for sharp-nosed slender bodies such as an air-fighter forebody

[13, 14], and assumed that this asymmetry would not occur with blunt-nosed bodies, because they are generally less sensitive to asymmetric disturbances [15]. Coincidentally, a similar side force and asymmetric wake were observed in an experimental study carried out by Ashok et al. [16], for a spheroid-like submarine hull at incidence. These results revealed, beyond any doubt, that asymmetry is an intrinsic feature of similar wake flows. This conclusion may be especially important for the marine and aerospace community because prolate spheroids can be an idealized prototype for UUVs (Unmanned Underwater Vehicles), submarine bare hulls, and various aircraft, and the asymmetric wake may have significant influence on the manoeuvring capabilities of these vehicles.

Jiang et al. [17] continued their investigations of the 45°-inclined prolate spheroid wake, and conducted more detailed explorations of the coherent structures in the wake, i.e. a concentrated helical vortex, at $Re_D = 3000$. They took advantage of the very detailed flow information from a DNS simulation, and reported several interesting features of the coherent wake structure and complex vortex interactions in this specific wake problem.

Encouraged by the recent progress, we aim to further increase the Reynolds number of the 45°-inclined 6:1 prolate spheroid to $Re_D = 4000$, and study the flow physics in the resulting near-wake. We have learned from previous studies that the wake is transitional at $Re_D = 3000$. Therefore, a modest increase in Re_D has two advantages: firstly, the main features of the wake should not change dramatically; secondly, since the wake is under transition, we might anticipate new and interesting flow features. Although this range of Reynolds numbers is outside the operating conditions of the type of vehicles mentioned earlier, this Reynolds number regime is ideal for simulations both in order to describe and understand fundamental flow physics and to serve as computational benchmarks and validation for large-eddy simulations (LES), detached-eddy simulations (DES) and Reynolds-averaged Navier-Stokes (RANS) simulations.

II. Problem and definitions

This paper presents the flow around a prolate spheroid with an aspect ratio of $\lambda = L : D = 6 : 1$, where L is the length of the major axis and D is the length of the two minor axes. D is thus also the maximum diameter of the circular cross-section that appears when the spheroid is sliced perpendicular to the major axis. The spheroid's orientation in the global coordinate system is found by first aligning the major axis of the spheroid x_{ax} with the global x-axis, and then rotating it 45° around the global z-axis. The constant inflow velocity is uniform $u = U_\infty$ in the positive x-direction with $v = w = 0$. The outlet is a fixed-pressure boundary condition with zero-gradient Neumann conditions for the velocity. The four other side boundaries (perpendicular to either the y or z-axes) of the domain are slip-walls in which the wall-normal velocity component is prescribed to be zero, while the two other velocity components and the pressure have a zero-gradient Neumann condition. The flow is incompressible and assumed to be governed by the Navier-Stokes equations together with the equation for conservation of mass. The Reynolds number based on the equatorial diameter D is $Re_D = DU_\infty/\nu = 4000$ in the present work.

The size of the computational domain is shown in figure 1. To facilitate easy discussion we choose to adopt the

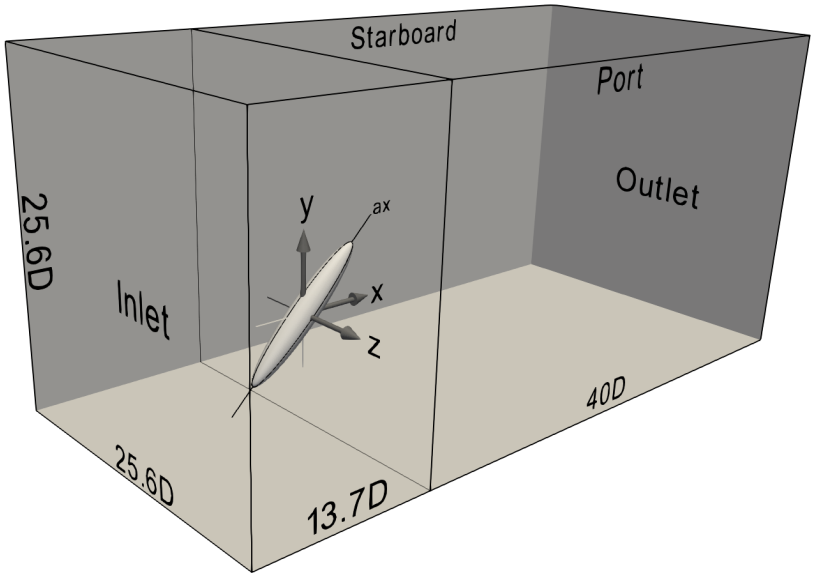

Figure 1 Computational domain and coordinate systems. D is the length of the spheroid's minor axis. The origin of the coordinate systems is in the center of the spheroid. To emphasize the spheroid shape and orientation, it is enlarged with respect to the surrounding domain. The terms *starboard* and *port* are used for the sides corresponding to the negative and positive z-axis, respectively. The spheroid is pointing with its nose down.

(aero)nautical terms *port* and *starboard* to distinguish the two sides of the spheroid. The port side is to the left when the observer is positioned at the spheroid and looking against the oncoming flow. In mathematical notation, the port side is the half of the spheroid with $z > 0$ and the starboard side is the half of the spheroid with $z < 0$.

We will also use a rotated coordinate system to present results. This coordinate system is found by rotating the original coordinate system (in which the inflow is parallel to the x-axis) 45° in positive direction around the z-axis, such that the resulting first axis coincide with the major axis of the spheroid. Flow variables presented in the rotated coordinate system will have the 'ax'-subscript, e.g. the flow velocity u_{ax}.

To enhance the 3-D visualizations and help in setting the point of view, we have added two meridian lines to several of the figures presented in this paper. The first line is the intersection line between the spheroid and the xy-plane, and the second line is the intersection between the spheroid and the zx_{ax}-plane.

III. Numerical methods

The code *MGLET* [18] has been used to perform all simulations presented in this paper. MGLET uses a finite-volume formulation on staggered Cartesian grids to solve the incompressible Navier-Stokes equations using linear interpolation and integration for all spatial terms, hence leading to second-order accuracy in space. A third-order low-storage explicit

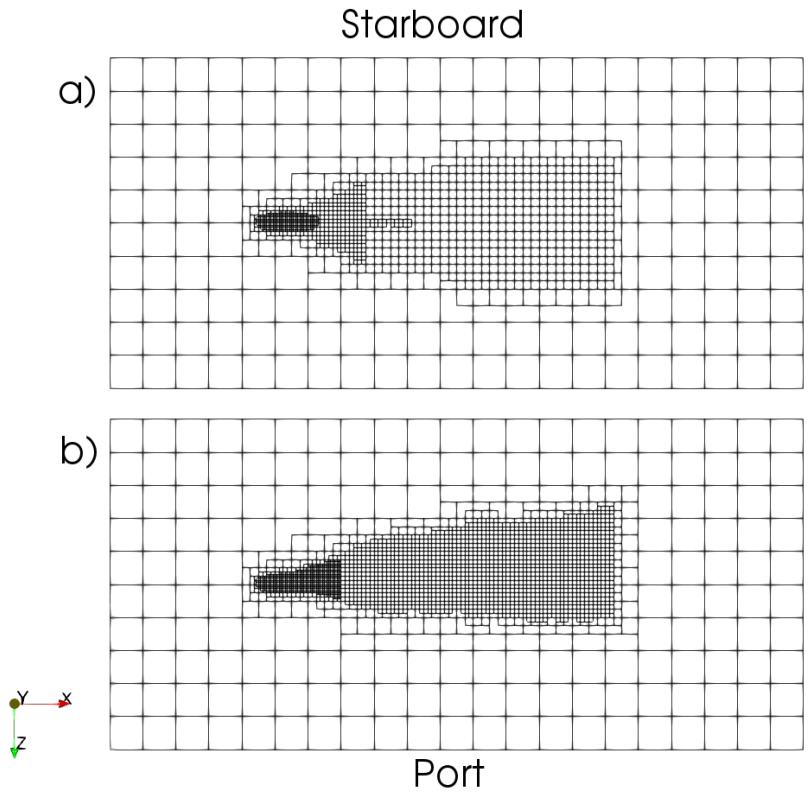

Figure 2 a) grid on which initial development of flow was conducted b) final grid on which the final results are computed. Each box in the figure represents a cube of $40 \times 40 \times 40$ grid cells.

Runge-Kutta time integration scheme [19] is used for time stepping. The time step is fixed at 0.001 D/U_∞ in the entire simulation.

MGLET introduces the solid geometry through an immersed boundary method [20]. A local refinement of the grid around the spheroid is achieved by constructing a multi-grid hierarchy that together form an unstructured arrangement of Cartesian grid boxes. In the simulation presented here, we use five grid levels in total. This resolves the solid geometry surface, its boundary layers and the wake behind it sufficiently while keeping the total number of grid cells at a reasonable level. The refinement process is a simple cell splitting, in which each parent grid cell subject to refinement is split into eight equal (3-D) child cells [21].

To develop an efficient grid without wasting cells in areas with no interesting flow structures, we initially constructed a symmetric grid with the desired final resolution close to the spheroid surface, as seen in figure 2a). The flow was simulated on this grid for a long time, and when the asymmetry was fully developed, we mapped the flow on to a new,

Table 1 Grid and simulation parameters compared to reference [11]. $\Delta x, \Delta y, \Delta z$ **is the grid spacing.**

Case	$Re_D = 3000$ [11]	$Re_D = 4000$ (present)
$min(\Delta x, \Delta y, \Delta z)$	$0.006D$	$0.004D$
Number of grid cells	0.75×10^9	2.1×10^9
Time step	$0.001D/U_\infty$	$0.001D/U_\infty$
Sampling time	$600D/U_\infty$	$369D/U_\infty$
Domain size $L_x \times L_y \times L_z$	$38D \times 24D \times 21D$	$53.7D \times 25.6D \times 25.6D$

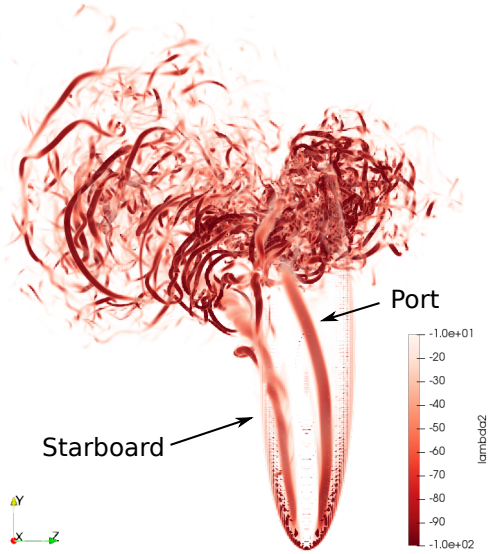

Figure 3 3-D rendering of the λ_2 vortex identification measure [22], seen seen from upstream. The spheroid body is not shown, to be able to see the flow structures behind it. The figure is created at time $t = 345.760D/U_\infty$.

asymmetric grid with improved wake resolution, as shown in figure 2b). After a second, short, simulation we used this result as the initial condition for all further simulations from where our reference time sampling $t = 0$ starts.

The resulting grid and simulation parameters are summarised in table 1. It is worth mentioning that due to recent efficiency improvements in the MGLET code, the present simulations are considerably cheaper to execute compared to previous works, despite the fact that we have nearly three times as many grid cells as in [11].

IV. Results

A. Forces and torques

Similar to Reynolds number 3000 [11], the present wake is highly asymmetric, see figure 3. Because of this, there is a strong sideforce F_z acting on the spheroid. The average sideforce is of the same order of magnitude as the average

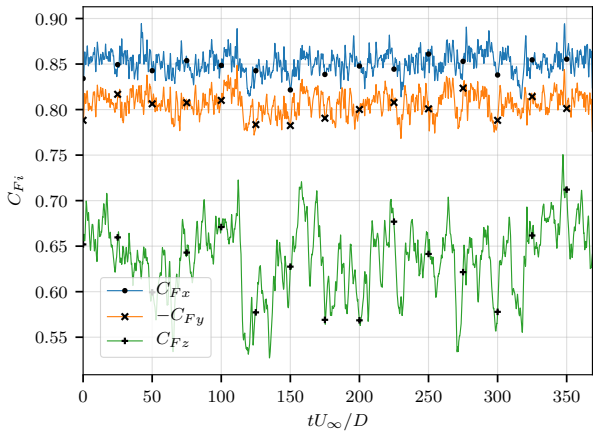

Figure 4 Force coefficients on the spheroid during the simulation.

Table 2 Mean and root-mean-square (RMS) of the force and torque coefficients. Coefficients at $Re_D = 3000$ are from [11].

Re_D		C_{Fx}	C_{Fy}	C_{Fz}	C_{Mx}	C_{My}	C_{Mz}
3000 (ref [11])	Mean	0.879	-0.796	-0.645	-0.168	0.166	0.311
	RMS	0.006	0.006	0.019	0.009	0.009	0.010
4000 (present)	Mean	0.852	-0.807	0.637	0.084	-0.082	0.315
	RMS	0.012	0.013	0.039	0.019	0.019	0.015

drag force F_x. See figure 4. Since the inflow and geometry is symmetric about the xy-plane, this asymmetry is caused by the resulting flow only.

In this work we normalize all forces the same way

$$C_{Fi} = \frac{F_i}{\frac{1}{2}\rho U_\infty^2 A_{\text{ref}}} \quad , \quad i = x, y, z \tag{1}$$

and for the torques

$$C_{Mi} = \frac{M_i}{\frac{1}{2}\rho U_\infty^2 A_{\text{ref}} d} \quad , \quad i = x, y, z \tag{2}$$

where M_i is the torque around axis i in the coordinate system given in figure 1. The reference length $d = 1.817D$ is the diameter of a sphere with the same volume as the 6:1 spheroid, and the reference area is $A_{\text{ref}} = \pi d^2/4$. This is the same as used in previous literature on the same geometry.

Table 2 gives the force coefficients for each of the three main directions. We see that in the present case, both the drag (C_{Fx}) and the sideforce (C_{Fz}) are slightly lower in magnitude than the corresponding values for $Re_D = 3000$ [11]. The average drag coefficient is $C_{Fx} = 0.852$ in our case, and the average sideforce coefficient is $C_{Fz} = 0.637$, that is 75 % of the magnitude of the drag force. Since the wake developed to the other side in the $Re_D = 3000$ case, the sideforce C_{Fz} and torques C_{Mx} and C_{My} have the opposite sign in the two cases. The different wake asymmetry is caused by insignificant numerical differences in the initial development of the flow. Each of the two asymmetric wakes are equally likely. The vertical lift force is $C_{Fy} = -0.807$, approximately the same as in the $Re_D = 3000$ case.

For $Re_D = 3000$ Jiang et al. [11] observed clear periodic oscillations in the sideforce F_z with a period of around $13.6D/U_\infty$, see figure 2 in [11]. At the present Reynolds number, the sideforce coefficient history, as shown in figure 4, no longer show any obvious periodic patterns. However, the magnitude of the fluctuations are twice as large, as seen in the difference in the RMS of C_{Fz} between the cases.

Compared to the previously reported force coefficients at $Re_D = 3000$, table 2 shows much of the same general tendency, except for the torque coefficients C_{Mx} and C_{My}. At the Reynolds number of 4000, the magnitude of the mean torque around the x and y-axis is half of that at Reynolds number 3000, but the root-mean-square (RMS) value of the fluctuations of the two coefficients are twice as large. At the present Reynolds number the RMS of the torque coefficients C_{Mx} and C_{My} are now about 25 % of the mean value. Similarly, the RMS of the force coefficients in all three directions have doubled. One possible explanation can be that this is a consequence of the increased turbulence and chaos in the flow associated with the strong port side vortex. The turbulence provides a more uniform and symmetric loading in average, but the oscillations are much higher in this more turbulent flow regime compared to $Re_D = 3000$.

The pressure in the core of the two main vortices are of interest to study. Jiang et al. [17] presented the pressure along the core of the weaker vortex (in the present case this is the starboard vortex in figure 3), which showed two

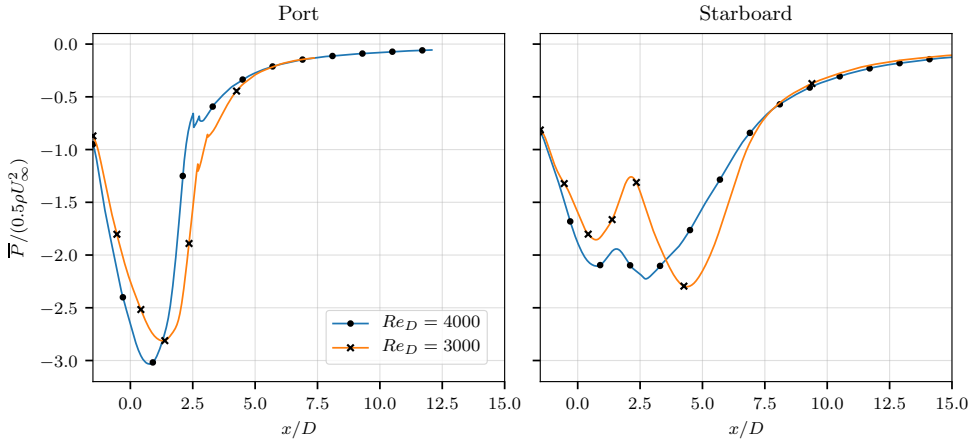

Figure 5 Time-average of pressure in the vortex cores of the present case compared to Reynolds number 3000. The Reynolds number 3000 results are mirrored (i.e. port and starboard are switched) to be comparable with the present case. Results from $Re_D = 3000$ are from [17].

distinct minima. In the present $Re_D = 4000$ case, we extracted the pressure along both vortex cores (defined as the locus of the pressure minima) in the same way, and observe a striking difference in both the strong and weak vortex. This is shown in figure 5. The present strong port side vortex has grown even stronger (with lower pressure), and the location of the pressure minima has shifted slightly forwards. In the weaker vortex core there were previously two distinct pressure minima with a significant peak in between, as seen in figure 5. This was associated with the helical vortex alteration as described by [17]. These minima have now shifted both in magnitude and position and coincide, only separated by a slight increase in pressure. The maxima in between them now also has a much lower pressure. The fact that the increase in Reynolds number between the cases is very modest, supports our claim that the present case is highly transitional and only a small change in Reynolds number gives rise to huge changes in the flow structures.

B. Overall wake topology

The coherent vortical structure originating from the weak starboard tip vortex is still present as for the lower Reynolds numbers, but it now appears to be more unsteady. Starting from the tip of the spheroid, a counter-rotating vortex pair is generated from the shear layers, see plane at $x/D = -1.5$ in figure 6. In the front part at $x/D = -1.5$, the port side vortex grows stronger by 25 % compared to the starboard side vortex, creating an imbalance between the two. The result is that the vortices twist and bend such that the stronger port vortex is attracted to the spheroid surface, moving towards the centerline further downstream along the spheroid, and the weaker starboard vortex is deflected outwards and downwards from the spheroid surface, see figure 6. The stronger port vortex is not much affected, neither by the shear layers forming from the spheroid nor the freestream, because it is mostly sheltered behind the spheroid body. Hence it is

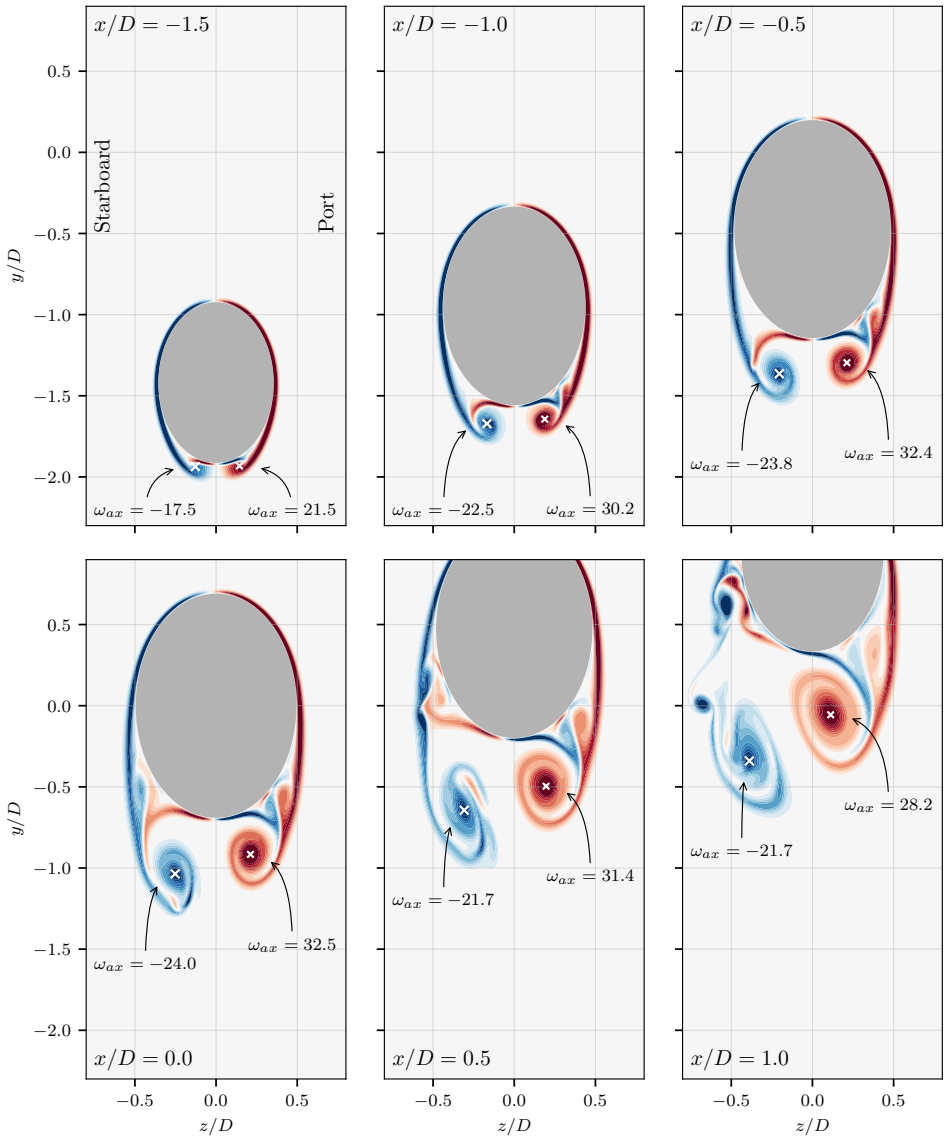

Figure 6 Axial vorticity ω_{ax} in six yz-planes along the spheroid, indicating the development of the tip vortices. Figures are created at time $t = 345.760D/U_\infty$. The maxima and minima of ω_{ax} in the vortex cores are indicated with a white cross. Blue colors indicate negative and red colors indicate positive vorticity. All individual plots share the same color scales.

nearly stationary. However, when the stronger port vortex reaches the aft end of the spheroid, close to $x/D = 2.0$, and meets the flow coming over the spheroid, it immediately disintegrates into smaller turbulent structures. The weaker starboard vortex on the other hand, interacts with both the shear layers forming from the sides of the spheroid and the freestream, but in a highly complicated manner.

C. Axial flow behind the spheroid

There is a strong axial flow underneath the spheroid, see figure 7. The maximum value of the axial velocity u_{ax} exceeds 1.5 times the freestream velocity. This was first reported and described by Jiang et al. [11]. Very close to the nose of the spheroid (around $x/D = -1.5$), the axial flow is strongest *between* the port and starboard vortex, and further downstream the axial flow in both vortex cores increases in strength and exceeds the velocity between the vortices. The strong port vortex provides a stronger axial flow field than the weaker starboard vortex. This is similar to the results at $Re_D = 3000$ [11] and will not be discussed any further in this paper.

In the present simulation we observe a region of moderately strong *negative* axial velocity ($u_{\mathrm{ax}} < 0$) on the starboard side of the spheroid, see figure 7 and 8. The region of negative axial velocity is at the same side as the weaker vortex. The negative axial velocity also leads to the formation of not only one, but two distinct shear layers with different direction of the shear. The first shear layer is between the spheroid surface (with $u = v = w = 0$) and the region of negative axial velocity, and the second shear layer is between this region and the freestream. These shear layers are easily visible as thin white layers in figure 7.

To investigate details in the region of negative axial velocity, we randomly selected a number of seedpoints in the volume where $u_{\mathrm{ax}} < 0$. From these points we integrated streamlines in the instantaneous velocity field both downstream and upstream. The result is shown in figure 8. We notice that a large majority of the fluid particles that end up in the region of negative axial velocity, originate from the port side of the spheroid nose. After the fluid particles 'turn around' underneath the nose, from the port to the starboard side, they are captured by the powerful upwards axial flow that is established between the two main vortices. The main wake deflects towards starboard in this case, and so do the fluid particles. When they reach about halfway up along the spheroid, the fluid particles change direction and travel towards the spheroid nose again. Eventually they are captured by the starboard vortex and escape, repelled downstream in the helical vortex core. From this we understand that the region of negative axial velocity is *not* a *recirculation region* where the same fluid is constrained in a small region and circulate without exchange of fluid, but a *backflow* region where the fluid enter in the rear part, flows towards the nose of the spheroid, and leaves through the starboard vortex. 'Fresh' fluid is continuously exchanged through the backflow region.

The exact mechanisms creating this backflow region is not yet fully understood, however, we suspect that differences in separation patterns between port and starboard side of the spheroid have strong influence on it. On the port side, there is suction due to the strong vortex (which is the cause of the strong sideforce F_z), while on the starboard side there is

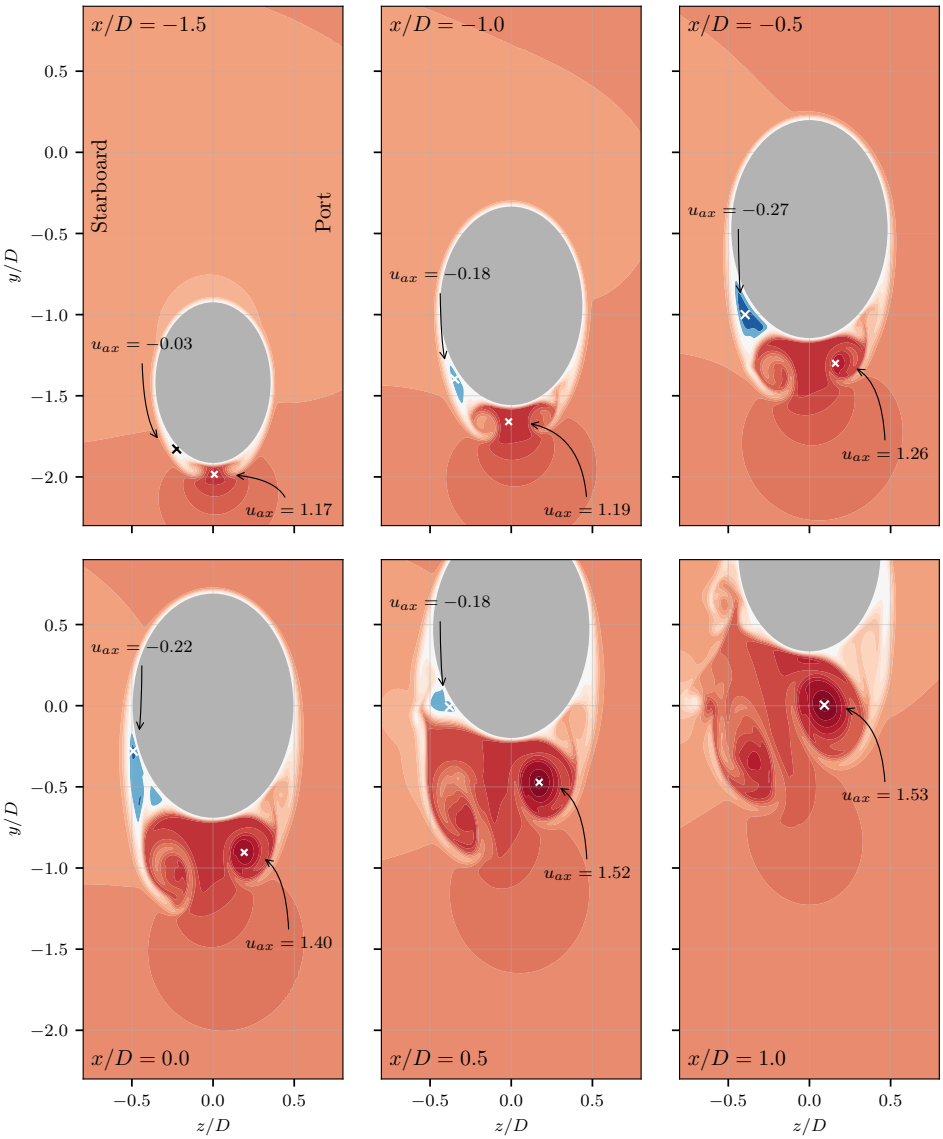

Figure 7 **Axial velocity u_{ax} in the same six yz-planes along the spheroid as in figure 6. Figures are created at time $t = 345.760D/U_\infty$. The velocity component shown is the component parallel to the spheroid axis. Blue colors indicate negative and red colors indicate positive velocity. All individual plots share the same color scales. The maximum and minimum values of velocity u_{ax} are indicated on the figure with crosses.**

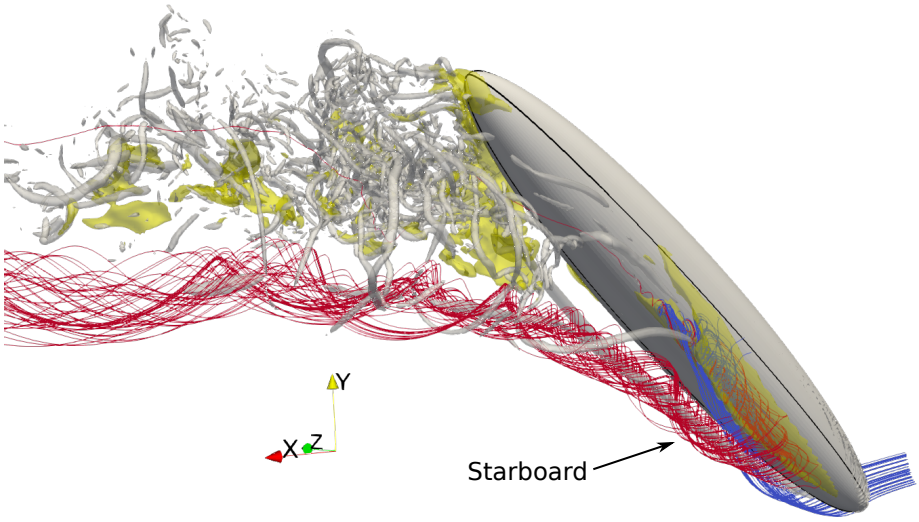

Figure 8 3-D perspective view of starboard side. Regions with backflow ($u_{\mathbf{ax}} < 0$) are enclosed with yellow isosurfaces. The spheroid body and vortex cores (here defined by $\lambda_2 < -80$) are both grey. The streamlines are integrated from randomly selected seed points in the backflow region both upstream and downstream. The lines from the backflow region and upstream towards the inflow, are blue, and the lines exiting and moving downstream and into the wake, are red. The perimeter of the 3-D yellow region near the starboard nose is the boundary of the backflow region. Figure is created at time $t = 345.760D/U_\infty$.

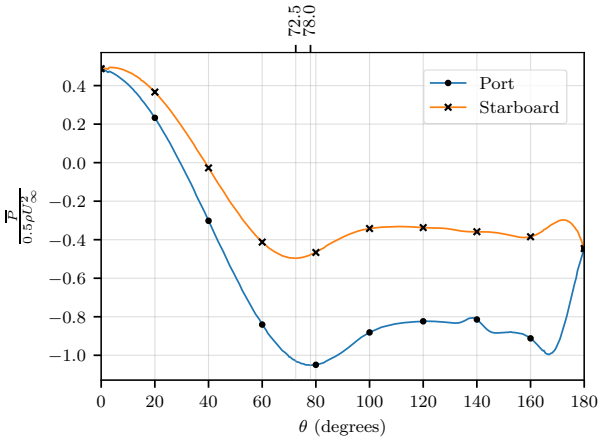

Figure 9 Time-averaged pressure in a plane perpendicular to the major spheroid axis at $x_{\mathbf{ax}} = 0.0$ (the centroid of the spheroid). The location of minima of the pressure at port and starboard side is indicated on the upper abscissa. Zero degree is the upper ridge of the spheroid, facing the inflow, and 180 degrees are the backside of the spheroid.

less suction. The minima of the pressure is shifted downwards about five degrees on port side compared to starboard side, see figure 9. Based on observations of the flow direction a few grid cells away from the wall, we see that the flow separation at the center of the spheroid is about 90 degrees from the ridge on the starboard side and 100 degrees on the port side.

D. Interaction between the starboard main vortex and the shear layer

The weaker starboard side vortex, being deflected away from the spheroid surface and into the freestream, interacts with the double shear layers between the spheroid, backflow region and freestream. In this interaction region, a number of interesting phenomena occur. In order to explore some of them, we conducted a simulation from where we saved the entire 3-D flow field in a selected region close to the spheroid every 15th time steps, that is every $0.015D/U_\infty$. The simulation was conducted for 30 000 timesteps, which resulted in a dataset of 2000 full 3-D flow field snapshots. This collection of 3-D flow fields has been examined and interesting flow phenomena have been selected and will be discussed in the following sub-sections. The same data is also used to create the attached animation.

For a long duration of time a double helical structure is observed, see figure 10a). The weak starboard tip vortex interacts with a secondary vortex originating from the shear layer on the starboard side. This vortex pair curl around each other, forming a helical pair of vortices with the same rotational direction. This secondary vortex is in fact stronger (in terms of maximum vorticity in the vortex core) than the starboard tip vortex. The two vortices both rotate in the same direction, that is, they have negative axial vorticity. This is easily explained by the fact that they are both generated from the same side of the spheroid, one originating from the nose and the other originating near the center of the spheroid. The same pair of helical vortices are also shown in figure 6, in the plane at $x/D = 1.0$.

The formation of this helical pair originates from the main starboard vortex that separates from the boundary layer and turns downstream. This is particularly visible in figure 8. However, the boundary layer continues to roll up, and generates more vortices. From several time instants in the simulation we count between two and four additional vortices being generated from the starboard boundary layer. All of them have the same rotational direction, and occasionally they form helical pairs with the main starboard vortex structure.

In another sequence of repetitive events a number of delicate and almost identical hairpin vortices are formed outside of the shadow of the spheroid and shear layers, as indicated on figure 10 b) and c). The hairpin vortices are generated and elongated, while they simultaneously wrap themselves around the core of the starboard tip vortex. The origin of these hairpin vortices is the turbulence generated by the port side tip vortex when it disintegrates. At certain times, a single vortex from the port side is wrapped around the starboard side tip vortex. This is when the hairpin vortices are created.

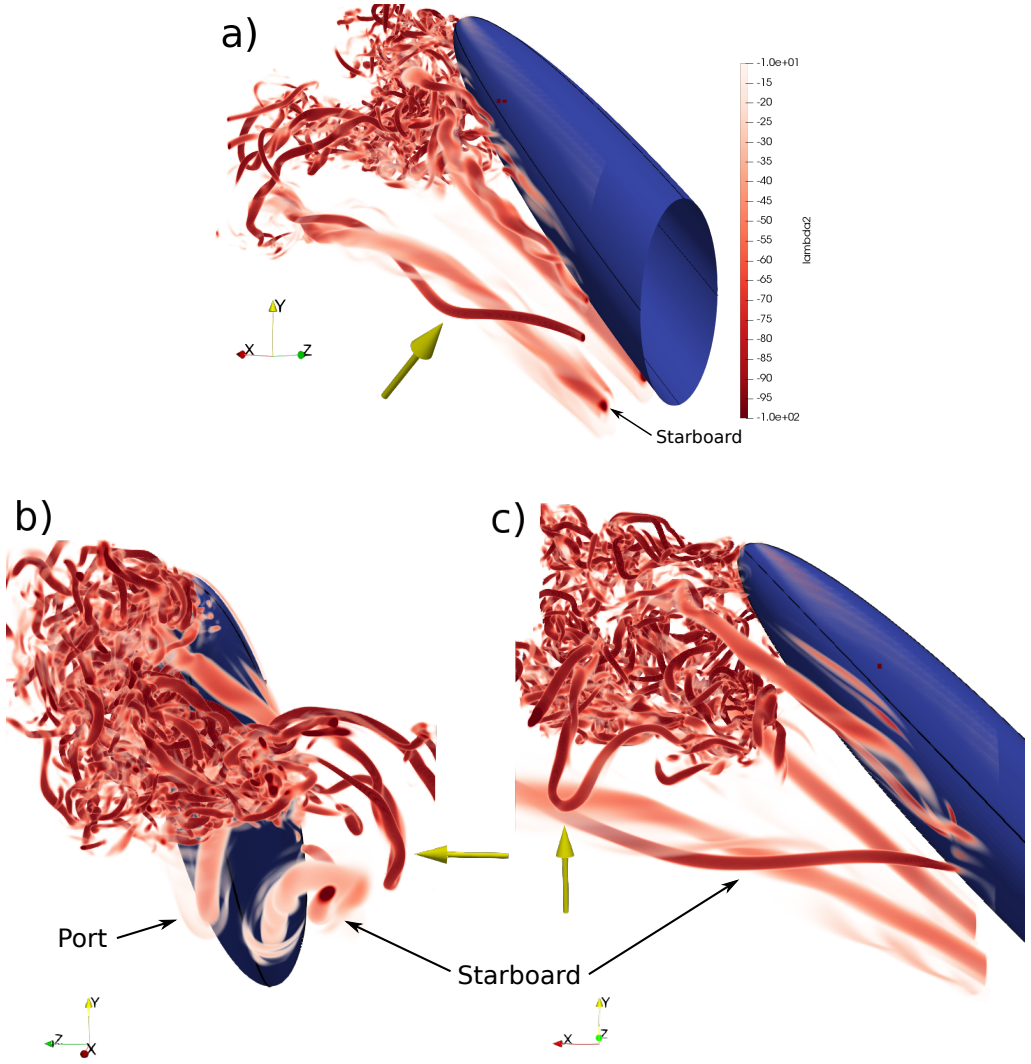

Figure 10 (a): double helical structure at time $t = 346.825D/U_\infty$. (b) and (c): hairpin vortex formation at time $t = 354.835D/U_\infty$ from two different viewpoints. The yellow arrows indicate the features of interest.

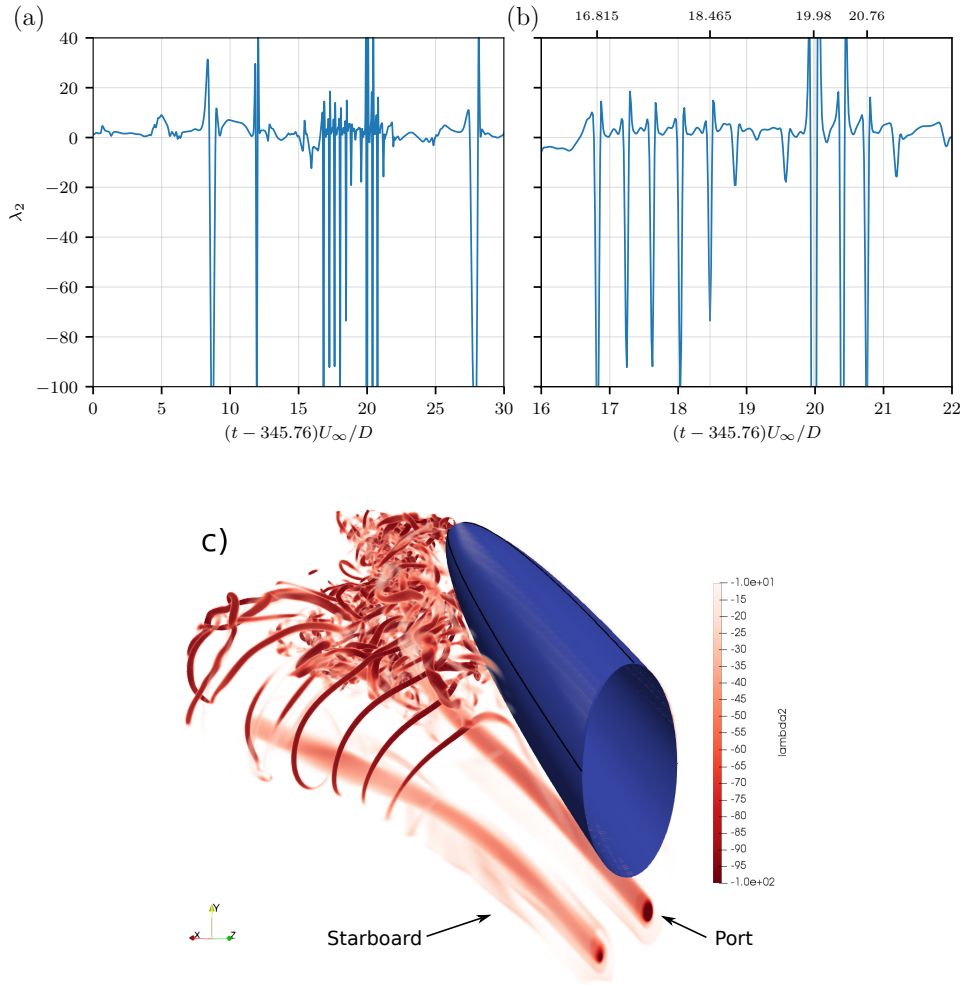

Figure 11 **a): Time-evolution of λ_2 through point $(x, y, z) = (1.5, 0.1, -0.85)$ indicating when a vortex core passes through this point. b): like a), but zoomed in around the region of the observed Kelvin-Helmholtz instabilities. c): 3-D rendering of the Kelvin-Helmholtz instability from the starboard shear layer at time $t = 363.790D/U_\infty$.**

E. Intermittent Kelvin-Helmholtz vortices

When we study the time-series from the simulations, a number of nearly identical vortex filaments are observed on the starboard side only. These are traced back to the shear layer that rolls up and forms the starboard side tip vortex. We have already discussed the double shear layers that form due to the backflow in this region, and from the outermost of these we observe the characteristic Kelvin-Helmholtz instability, similar to what occurs in the shear layer shed from a circular cylinder, see figure 11c).

Since the studied time series are limited and we only observed one of these 'bursts' of Kelvin-Helmholtz instabilities, we cannot compute the intermittency factor. However, we do get a very good estimate of the frequency of these events because they occur very regularly. Figure 11 a) and b) show λ_2 in a point $(x, y, z) = (1.5, 0.1, -0.85)$ as a function of time. Each time a vortex core passes by, in the vicinity of this point, the measured value drops far below 0 in the plot. In the time intervals (16.815 - 18.465 D/U_∞ and 19.98 - 20.76 D/U_∞) we see five and three such vortices passing by. In addition there might be some vortices passing nearby in the interval 18.465 - 19.98 D/U_∞, but that is not directly clear from the plot alone. In total, from figure 11b) we can estimate the period of the instabilities to be approximately $0.4D/U_\infty$, corresponding to a frequency of 2.5 U_∞/D.

This frequency of 2.5 U_∞/D is amazingly high for a Kelvin-Helmholtz shear layer instability compared to for instance similar frequencies found in the shear layers of circular cylinders. The similar instability frequency of shear layers shedding from a circular cylinder are $5f_v$ [23], which is around $1U_\infty/D$ for a Strouhal number of 0.2. This is generally valid over a broad range of Reynolds numbers around 4000. However, there is a striking similarity between the current investigated spheroid shear layer instability and the Kelvin-Helmholtz instabilities found in shear layers around spheres. Constantinescu and Squires [24] performed direct numerical simulations of the flow around a sphere at $Re = 10000$, and found Kelvin-Helmholtz instabilities in the frequency range between 1.9 and 2.4 U_∞/D. This is in good agreement with the present result.

Another very interesting observation is that the rotational direction of the Kelvin-Helmholtz vortices are opposite of the intuitive direction. In figure 12 the yellow arrows indicate regions of high and low fluid velocity, the larger arrow indicates higher velocity (details on this is shown in figure 7). Since the axial fluid velocity on the leeward side (back side) of the spheroid is *higher* than the freestream velocity, the observed Kelvin-Helmholtz vortices have a *positive* vorticity ω_y. If the fluid behind the spheroid was nearly stagnant (like the recirculation zone behind a circular cylinder) the rotation of the Kelvin-Helmholtz vortices would have been in the opposite direction.

V. Concluding Remarks

The wake behind the 45° inclined 6:1 prolate spheroid at $Re_D = 4000$ turned out to be severely skewed as in the $Re_D = 3000$ case, in spite of the completely symmetric geometry. Although the force coefficients were almost identical, the secondary torque coefficients in the present case were substantially reduced compared to the lower-Re case. Also,

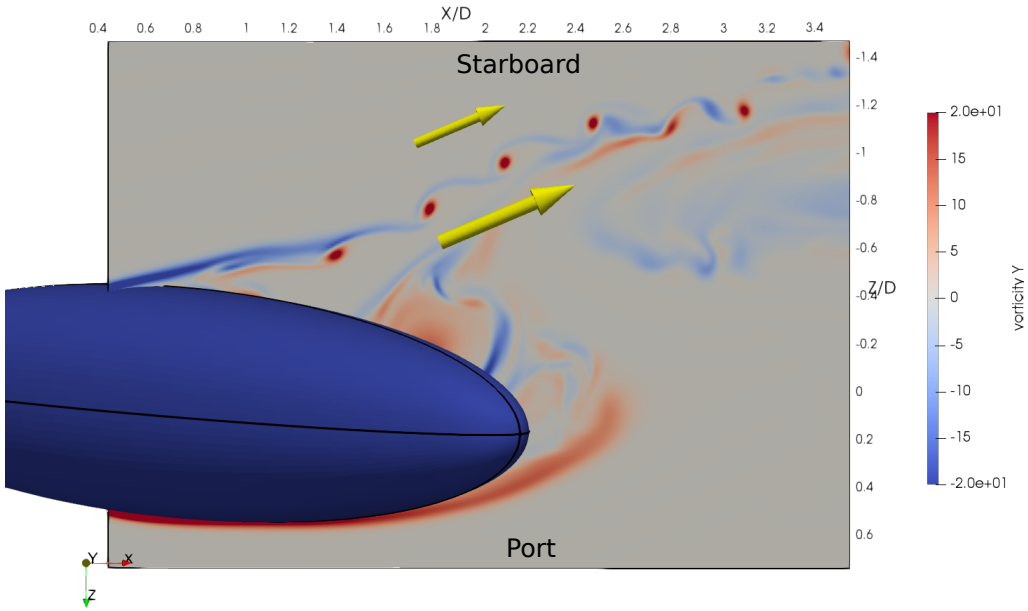

Figure 12 **A xz-slice at $z = 0.63$ colored by the vorticity ω_y, showing the Kelvin-Helmholtz vortices at time $t = 363.790D/U_\infty$. The yellow arrows indicate regions with high (large arrow) and low (small arrow) fluid velocity.**

the RMS of all force- and torque coefficients are roughly doubled from $Re_D = 3000$, which indicate a major change in the near-wake with more unsteadiness than before.

The pressure within the two main coherent vortical structures was also significantly changed from $Re_D = 3000$. The two minima from the helical vortex alteration process are almost gone in the present case. This confirms the hypothesis from the introduction, that the flow is highly transitional in this Reynolds number regime.

The present work is the first to describe the interesting backflow region associated with the weak starboard side vortex. In this region the fluid enters from behind, flows towards the nose and leaves through the weak starboard side vortex. There is a continuous exchange of fluid in this region.

The interesting flow phenomena reported in section IV, namely the double helix, the hairpin vortices and the Kelvin-Helmholtz vortices, are all observed intermittently. These phenomena repeat themselves intermittently, but the accompanying animations are not sufficiently long to draw conclusions about how recurrent they are. These intermittently occurring flow phenomena are confined in space and have only negligible influence on the force coefficients shown in figure 4. The intermittent vortex dynamics in the $Re_D = 4000$ wake strongly suggest that the flow is in a transitional regime where modest variations in the Reynolds number give rise to major changes in the wake. Neither the double helix nor any Kelvin-Helmholtz vortices were observed at $Re_D = 3000$. We therefore speculate that periodic vortex dynamics phenomena may occur if the Reynolds is somewhat further increased.

We admit that the wake flow at $Re_D = 4000$ is in a transitional flow regime and strongly Reynolds number dependent. The intermittent phenomena observed herein were not reported at lower Reynolds numbers. This makes the present wake distinctly different from the wake at $Re_D = 3000$, although the overall asymmetries are in common.

VI. Acknowledgments

The authors wish to thank the employees at *KM Turbulenz GmbH* for all their help and technical support on the MGLET code. Computing time was granted by UNINETT Sigma2 under project *nn9191k*. F.J. acknowledges the funding from the Future Industry's Leading Technology Development program (No. 10042430) of MOTIE/KEIT of Korea.

References

[1] Wang, K., "Separation patterns of boundary layer over an inclined body of revolution," *AIAA Journal*, Vol. 10, No. 8, 1972, pp. 1044–1050. doi:10.2514/3.50292, URL https://dx.doi.org/10.2514/3.50292.

[2] Geissler, W., "Three-dimensional laminar boundary layer over a body of revolution at incidence and with separation," *AIAA Journal*, Vol. 12, No. 12, 1974, pp. 1743–1745. doi:10.2514/3.49593, URL https://dx.doi.org/10.2514/3.49593.

[3] Wetzel, T. G., Simpson, R. L., and Chesnakas, C. J., "Measurement of three-dimensional crossflow separation," *AIAA Journal*, Vol. 36, No. 4, 1998, pp. 557–564. doi:10.2514/2.429, URL https://dx.doi.org/10.2514/2.429.

[4] Chesnakas, C. J., Taylor, D., and Simpson, R. L., "Detailed investigation of the three-dimensional separation about a 6:1 prolate spheroid," *AIAA journal*, Vol. 35, No. 6, 1997, pp. 990–999. doi:10.2514/2.208, URL https://dx.doi.org/10.2514/2.208.

[5] Rhee, S. H., and Hino, T., "Numerical simulation of unsteady turbulent flow around maneuvering prolate spheroid," *AIAA Journal*, Vol. 40, No. 10, 2002, pp. 2017–2026. doi:10.2514/2.1534, URL https://dx.doi.org/10.2514/2.1534.

[6] Simpson, R. L., "Aspects of turbulent boundary-layer separation," *Progress in Aerospace Sciences*, Vol. 32, No. 5, 1996, pp. 457–521. doi:10.1016/0376-0421(95)00012-7, URL https://doi.org/10.1016/0376-0421(95)00012-7.

[7] Andersson, H. I., Jiang, F., and Okulov, V. L., "Instabilities in the Wake of an Inclined Prolate Spheroid," *Computational Modelling of Bifurcations and Instabilities in Fluid Dynamics*, edited by A. Gelfgat, Springer International Publishing AG, Switzerland, 2019, Chap. 9, pp. 311–352. doi:10.1007/978-3-319-91494-7_9.

[8] El Khoury, G. K., Andersson, H. I., and Pettersen, B., "Crossflow past a prolate spheroid at Reynolds number of 10000," *Journal of Fluid Mechanics*, Vol. 659, 2010, pp. 365–374. doi:10.1017/S0022112010003216, URL https://doi.org/10.1017/S0022112010003216.

[9] El Khoury, G. K., Andersson, H. I., and Pettersen, B., "Wakes behind a prolate spheroid in crossflow," *Journal of Fluid Mechanics*, Vol. 701, 2012, pp. 98–136. doi:10.1017/jfm.2012.135, URL https://doi.org/10.1017/jfm.2012.135.

[10] Jiang, F., Gallardo, J. P., and Andersson, H. I., "The laminar wake behind a 6:1 prolate spheroid at 45° incidence angle," *Physics of Fluids*, Vol. 26, No. 11, 2014, p. 113602. doi:10.1063/1.4902015, URL https://doi.org/10.1063/1.4902015.

[11] Jiang, F., Gallardo, J. P., Andersson, H. I., and Zhang, Z., "The transitional wake behind an inclined prolate spheroid," *Physics of Fluids*, Vol. 27, No. 9, 2015, p. 093602. doi:10.1063/1.4929764, URL https://doi.org/10.1063/1.4929764.

[12] Jiang, F., Gallardo, J. P., and Andersson, H. I., "Transition and loss of symmetry in the wake behind an inclined prolate spheroid," *8th National Conference on Computational Mechanics MekIT'15*, edited by B. Skallerud and H. I. Andersson, International Center for Numerical Methods in Engineering (CIMNE), Barcelona, Spain, 2015, pp. 219–232.

[13] Cobleigh, B., "High-angle-of-attack yawing moment asymmetry of the X-31 aircraft from flight test," *12th Applied Aerodynamics Conference*, 1994, p. 1803. doi:10.2514/6.1994-1803, URL https://doi.org/10.2514/6.1994-1803.

[14] Bridges, D., "The asymmetric vortex wake problem - Asking the right question," *36th AIAA Fluid Dynamics Conference and Exhibit*, 2006, p. 3553. doi:10.2514/6.2006-3553, URL https://doi.org/10.2514/6.2006-3553.

[15] Moskowitz, C., Dejarnette, F. R., and Hall, R. M., "Effects of nose bluntness, roughness, and surface perturbations on the asymmetric flow past slender bodies at large angles of attack," *7th Applied Aerodynamics Conference*, 1989, p. 2236. doi:10.2514/6.1989-2236, URL https://doi.org/10.2514/6.1989-2236.

[16] Ashok, A., Van Buren, T., and Smits, A., "Asymmetries in the wake of a submarine model in pitch," *Journal of Fluid Mechanics*, Vol. 774, 2015, pp. 416–442. doi:10.1017/jfm.2015.277, URL https://doi.org/10.1017/jfm.2015.277.

[17] Jiang, F., Andersson, H. I., Gallardo, J. P., and Okulov, V. L., "On the peculiar structure of a helical wake vortex behind an inclined prolate spheroid," *Journal of Fluid Mechanics*, Vol. 801, 2016, pp. 1–12. doi:10.1017/jfm.2016.428, URL https://doi.org/10.1017/jfm.2016.428.

[18] Manhart, M., Tremblay, F., and Friedrich, R., "MGLET: a parallel code for efficient DNS and LES of complex geometries," *Parallel Computational Fluid Dynamics - Trends and Applications*, edited by C. B. Jenssen, T. Kvamdal, H. I. Andersson, B. Pettersen, A. Ecer, J. Periaux, N. Satofuka, and P. Fox, Elsevier Science B.V., The Netherlands, 2001, pp. 449–456. doi:10.1016/B978-044450673-3/50123-8, URL https://doi.org/10.1016/B978-044450673-3/50123-8.

[19] Williamson, J. H., "Low-storage Runge-Kutta schemes," *Journal of Computational Physics*, Vol. 35, No. 1, 1980, pp. 48–56. doi:10.1016/0021-9991(80)90033-9, URL http://dx.doi.org/10.1016/0021-9991(80)90033-9.

[20] Peller, N., Duc, A. L., Tremblay, F., and Manhart, M., "High-order stable interpolations for immersed boundary methods," *International Journal for Numerical Methods in Fluids*, Vol. 52, No. 11, 2006, pp. 1175–1193. doi:10.1002/fld.1227, URL http://dx.doi.org/10.1002/fld.1227.

[21] Manhart, M., "A zonal grid algorithm for DNS of turbulent boundary layers," *Computers & Fluids*, Vol. 33, No. 3, 2004, pp. 435–461. doi:10.1016/s0045-7930(03)00061-6, URL http://dx.doi.org/10.1016/S0045-7930(03)00061-6.

[22] Jeong, J., and Hussain, F., "On the identification of a vortex," *Journal of Fluid Mechanics*, Vol. 285, 1995, pp. 69–94. doi:doi.org/10.1017/S0022112095000462, URL https://doi.org/10.1017/S0022112095000462.

[23] Prasad, A., and Williamson, C. H. K., "The instability of the shear layer separating from a bluff body," *Journal of Fluid Mechanics*, Vol. 333, 1997, pp. 375–402. doi:10.1017/S0022112096004326, URL http://dx.doi.org/10.1017/S0022112096004326.

[24] Constantinescu, G., and Squires, K., "Numerical investigations of flow over a sphere in the subcritical and supercritical regimes," *Physics of fluids*, Vol. 16, No. 5, 2004, pp. 1449–1466. doi:10.1063/1.1688325, URL https://doi.org/10.1063/1.1688325.

Attached paper V

Low-Frequent Oscillations in Flow past an Inclined Prolate Spheroid

Håkon Strandenes, Fengjian Jiang, Bjørnar Pettersen, Helge I. Andersson

Under review in *International Journal of Heat and Fluid Flow*, September 2018.

Accepted for publication in International Journal of Heat and Fluid Flow

Low-Frequent Oscillations in Flow past an Inclined Prolate Spheroid

Håkon Strandenes[1], Fengjian Jiang[1], Bjørnar Pettersen[1], and Helge I. Andersson[2]

[1] *Department of Marine Technology*

[2] *Department of Energy and Process Engineering*

[1,2] *Norwegian University of Science and Technology, NO-7491 Trondheim, Norway*

Corresponding author e-mail: fengjian.jiang@ntnu.no

10th September 2018

Abstract

We analyse the forces on a 45° inclined 6:1 prolate spheroid at Reynolds number $Re_D = 8000$. In contrast to flow at lower Reynolds numbers previously investigated, we now find a strong oscillatory behaviour in the global forces. The Strouhal number associated with the forces is 0.05 and the peak-to-peak amplitude of the oscillations in the sideforce is more than 25% of the average. A Fourier transformation of the entire flow field reveals that the cause of the force fluctuations is spatial oscillations in one of the two primary vortices generated behind the spheroid. This phenomena is attributed to a three-dimensional vortex instability.

1 Introduction

The flow past a 45° inclined 6:1 (length:diameter) prolate spheroid has been subject to several numerical studies recently with emphasis on investigating details in the wake flow for cases up to $Re_D = 3000$ [1, 2, 3, 4]. The main motivation for studying this case is the flow features common for many vehicles in the air and ocean space. Based on the results from both simulations and experiments, there is acceptance for the resulting wake flow and forces on the spheroid to be asymmetric, despite the symmetric geometry and inflow condition. This applies to many inclined slender body flow cases [5, 6, 7].

Being a prototype for various vehicles, such as airplanes, drones, ROVs and submarines, focus in this work is on the manoeuvring capabilities and the external forces acting on the spheroid.

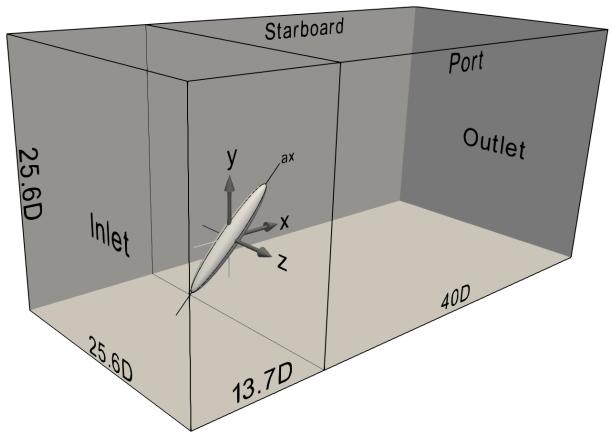

Figure 1: Computational domain and coordinate system. The origin of the coordinate system is in the center of the spheroid. The figure is not to scale.

We have learned from previous studies that the time-averaged wake exerts a significant mean side force on the spheroid, which can be up to 75% of the mean drag force at $Re_D = 3000$ (see e.g. [3]). Considering the engineering background of the inclined spheroid, it is interesting to investigate how strong this side force becomes and vary when the Reynolds number is further increased. This is the primary scope of the present study. At lower Reynolds numbers, very low-frequent oscillations of the side force were detected, see e.g. fig. 2 in [3], but were not carefully studied. It is assumed that three-dimensional effects could be the mechanism behind it, as addressed by Jiang et al. [3] and Zeiger et al. [8]. Some recent works on the wake behind sharp-nosed slender bodies at high incidence indicate similar low frequency forces from vortex oscillations other than vortex shedding (see e.g. [9] and [10]). It is therefore also of interest to investigate whether this low-frequency still manifests itself and how it develops as the Reynolds number is increased. In the present work, we will address these points by discussing results obtained by Direct Numerical Simulation (DNS).

Figure 1 shows the simulation domain along with its dimensions. The flow is governed by the mass conservation and Navier-Stokes equations for incompressible flow. The constant inflow velocity is uniform with $u = U_\infty$, $v = w = 0$. The outlet is a fixed-pressure boundary condition with zero-gradient Neumann conditions for the velocity. The four other side boundaries of the domain, perpendicular to the y and z-axes, are slip-walls in which the wall-normal velocity component is prescribed to be zero, while the other velocity components and the pressure have a zero-gradient Neumann condition. The Reynolds number based on the equatorial diameter D is $Re_D = DU_\infty/\nu = 8000$.

Table 1: Grid convergence study setup. All cases was simulated 163840 timesteps starting from the same initial condition, and the timestep was 0.001 D/U_∞ in all cases.

Simulation	coarse	medium	fine
Number of grid cells	0.447×10^9	1.660×10^9	2.077×10^9
Min. $\Delta x/D$	0.016	0.008	0.004

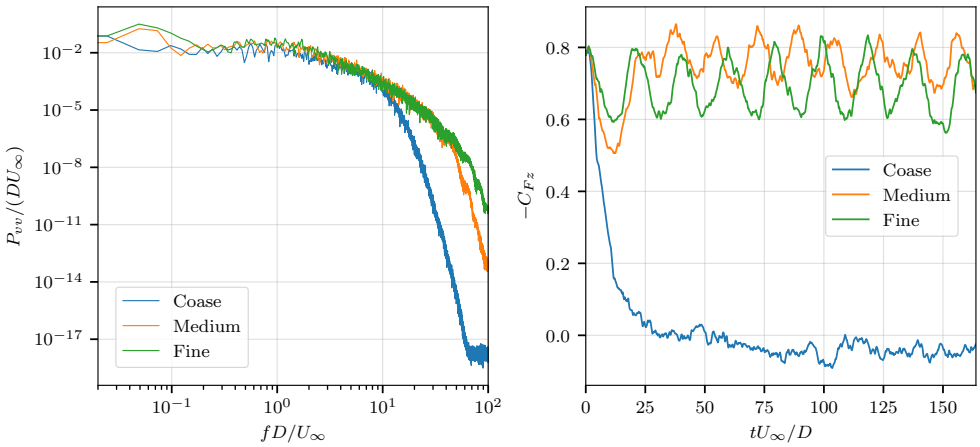

Figure 2: Results from the grid resolution study. Left: Power spectra of v-velocity sampled in point $(x, y, z) = (2.5, 1.32, 0.5)D$. Right: Sideforce coefficient C_{Fz} as a function of time.

2 Numerical methods

The code *MGLET* [11] is used for the simulations presented in this paper. In short, MGLET uses a finite-volume formulation on staggered Cartesian grids to solve the incompressible Navier-Stokes equations using linear interpolation and integration for all spatial terms, hence leading to second-order accuracy in space. A third-order low-storage explicit Runge-Kutta time integration scheme [12] is used for time stepping. The solid geometry is introduced through an immersed boundary method [13]. A combined multi-grid and local grid refinement method is used to *i)* increase the convergence rate of the pressure solver and *ii)* resolve geometrical and flow structures sufficiently [14].

To justify that the grid resolution is sufficient for the problem in question, we performed a grid resolution study. Three different meshes with different resolution were created (see table 1), and a fully developed flow field was computed on the finest grid. This solution was then transferred to the two coarser grids, and the three simulations were restarted and run for the same number of timesteps.

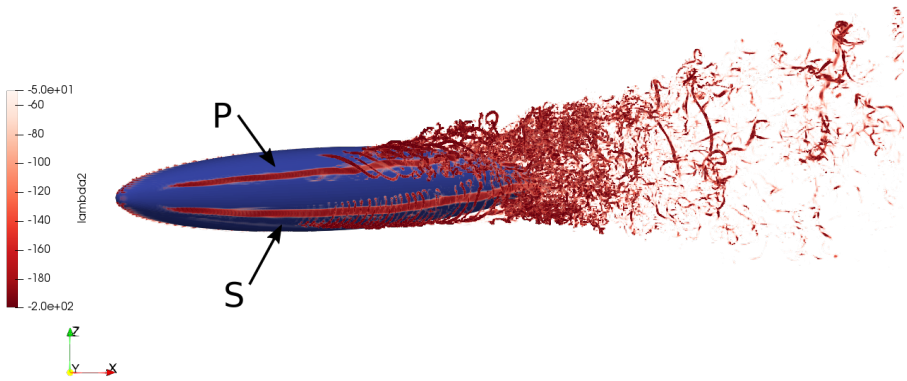

Figure 3: Overview of the wake visualized by a volume rendering of the λ_2 vortex identification criterion. The strongest of the two vortices is the lower one.

Figure 2 gives an overview of the results. The coarsest grid tested in this convergence study is clearly not satisfactory. The initial condition is a flow field with a strongly asymmetric side force C_{Fz}, which quickly develops into a nearly symmetric flow state with almost zero mean sideforce after restarting with the coarser grid. On the two finer grids (medium and fine) the asymmetric side force persists, but there are still differences in the computed forces. The power spectra of the v-velocity in a selected point in the wake, as shown to the left in figure 2, also indicate that the flow on the coarsest grid is severely under-resolved. A major portion of the energy at the higher frequencies is lost. The two finest grids show reasonable agreement, but the finer grid clearly manage to resolve more scales compared to the medium grid. In conclusion, we believe that the finest grid presented here is sufficiently fine to resolve all essential scales present in this flow with the required precision. The results discussed hereafter are all from the simulation using the finest mesh.

3 Results

In general, the flow structures in this flow configuration at $Re_D = 8000$ share many similarities with the flow at lower Reynolds numbers ($Re_D \approx 3000$), as referred to in the introduction. However, there are a few important distinctions. Figure 3 gives an overview of the flow structures of the present case, and shows the two main coherent vortices originating from the tip, here named S and P. The weaker of the two vortices is P and the stronger one is S, by means of maximum vorticity in the vortex core. The figure clearly shows that the weaker one, P, is the one to disintegrate closest to the nose. This is the opposite of the lower Reynolds number cases,

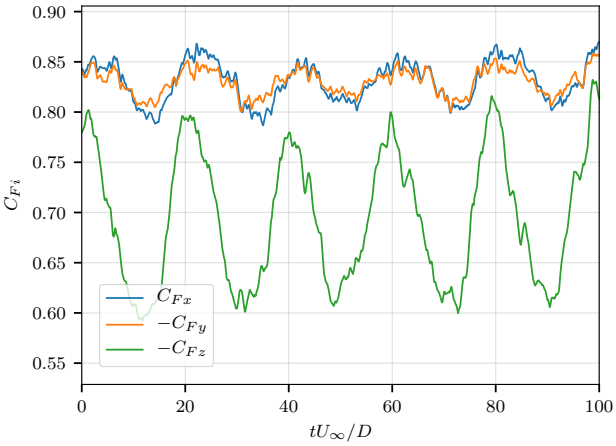

Figure 4: Drag and sideways force coefficients at $Re_D = 8000$ for the first 100 D/U_∞ simulated.

where the weakest of the two vortices was the most stable structure, persisting far downstream of the spheroid tail. Further details and analysis of the wake will be subject to a separate study and will not be presented herein.

We present the mean and RMS of the force coefficients compared to earlier results in table 2. From this we observe that the mean drag coefficient C_{Fx} decreases as the Reynolds number increases, while in the two other directions the coefficients C_{Fy} and C_{Fz} increases. This means that the side forces become more significant at $Re_D = 8000$ compared to for instance $Re_D = 3000$. Furthermore, there is one fundamentally new phenomenon that has never been reported before, at any Reynolds number, that is a very strong low-frequency oscillation in the forces from the fluid acting on the spheroid. Figure 4 gives an overview of the evolution of the force coefficients, from which this phenomenon is evident. This paper aims to present a concise and focused study on this new phenomenon.

The period of these low-frequent oscillations are almost exactly $T = 1/f = 20\ D/U_\infty$, leading to a Strouhal number of $St = fD/U_\infty = 0.05$. Compared to a typical vortex street behind a circular cylinder at similar Reynolds number with Strouhal number of $St = 0.2$, the present oscillation is surprisingly slow. One easily notice from figure 4, that the peak-to-peak amplitude of the side force C_{Fz} oscillations are more than 25 % of their mean value, revealing very strong flow dynamics in the wake that heavily influences the near pressure field. However, by inspections of the velocity field in the wake, we cannot find any signs of vortex shedding, and the presence of a von Karman vortex street can be ruled out. By using visualization in 2-D and 3-D of quantities

Table 2: Mean and root-mean-square (RMS) of the force and torque coefficients. Coefficients at $Re_D = 3000$ are from [3].

Re_D		C_{Fx}	C_{Fy}	C_{Fz}	C_{Mx}	C_{My}	C_{Mz}
3000 (ref [3])	Mean	0.879	-0.796	-0.645	-0.168	0.166	0.311
	RMS				0.009	0.009	0.010
4000	Mean	0.852	-0.807	0.637	0.084	-0.082	0.315
	RMS	0.012	0.013	0.039	0.019	0.019	0.015
8000 (present)	Mean	0.832	-0.831	-0.701	-0.123	0.122	0.316
	RMS	0.022	0.014	0.069	0.023	0.023	0.014

such as velocity, pressure, vorticity, λ_2 etc. no obvious other structures can be attributed to this phenomenon either.

In order to identify the source of these low-frequent oscillations, we employ a simple, novel technique we call *in-situ Fourier transform*. In this technique we evaluate a discrete Fourier transform of the entire pressure field for selected, pre-defined frequencies. This evaluation is performed in discrete time windows. Once each window is finished, the results are added to an accumulated, time-averaged Fourier coefficient for the selected frequencies. The real part of this Fourier coefficient is the total energy content of the selected wavelength, and is computed for every gridcell in the computational domain. In practice, the results are the same as if we had stored the pressure in every gridcell every timestep, and computed the energy spectra from these data, but only extracted the energies corresponding to a few frequencies. Therefore, this technique is especially economical and effective for DNS in light of the enormous number of grid cells used in the simulations.

The result is shown in figure 5. The red areas indicate zones where the pressure fluctuates strongly with $f = 1/20\ U_\infty/D$, and the blue areas indicate zones where the pressure fluctuates with frequency $2f = 2/20\ U_\infty/D$. The observed pattern can easily be explained: there is a cyclic motion of the two main wake vortices. The strongest vortex (S), which is located to the left in figure 5, moves from the leftmost red area (where it is strong), passing through the blue area (where it gets weaker or the path is more uncertain), and towards the next red area again, before it returns back the same path towards the origin at the leftmost red area. The vortex passes through the blue area twice per cycle, hence the double frequency. The pattern of this motion is an upside-down 'U'-pattern.

The weaker main vortex (P) also exhibits a similar motion, but along an almost vertical line instead of the curved path of the stronger vortex. In addition, the vortex itself is much weaker,

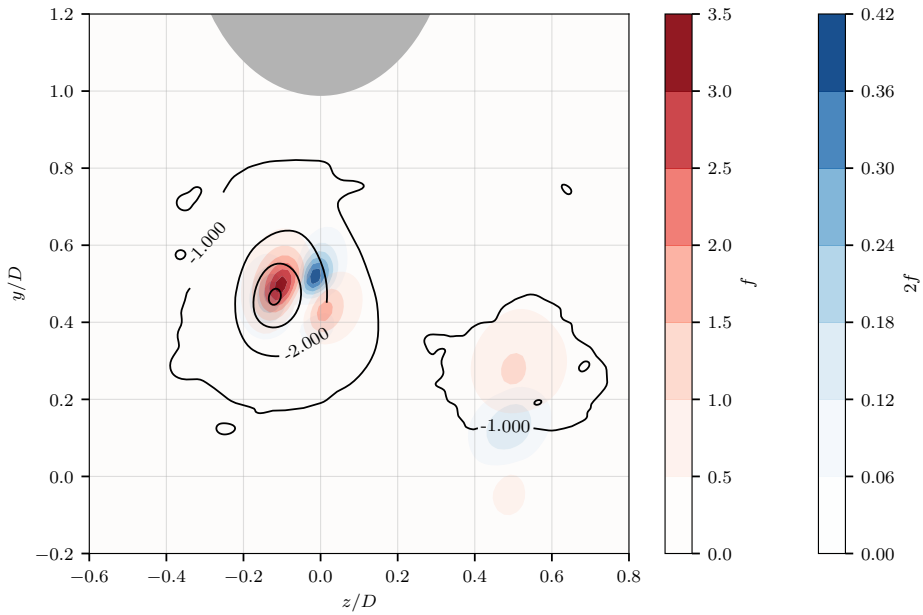

Figure 5: yz plane at $x/D = 1.55$. Spheroid cross-section are grey. Fourier amplitudes of the pressure at the frequency corresponding to the low-frequent oscillations in the forces $f = 1/20\ U_\infty/D$ (red colors) and the double of this frequency $2f = 2/20\ U_\infty/D$ (blue colors). The pressure coefficient $C_p = p/(0.5\rho U_\infty^2)$ from a randomly selected timestep is drawn with black iso-contours.

and thus the energies recorded are lower.

To further understand the motion of this vortex and how it influence the forces on the spheroid, additional simulations were carried out. In these simulations, the pressure was recorded in several planes perpendicular to the x-axis. From these time series, we identified the location of the vortex core by searching for the position of the lowest pressure. The trajectories of the vortex center in each x-plane, are shown in figure 6. Each dot corresponds to the position of the vortex core at a time instant, and the color indicates the strength of the vortex core at that time.

From figure 6 we can see that the motion of the vortex core at $x/D = 0.0$ is already visible, and forms an elliptical path. By the colouring, we also observe that the vortex core vary in strength throughout this oscillatory motion. When the vortex core is furthest away from the spheroid, it is usually stronger than when the vortex core is closer to the body. In the plane $x/D = 0.5$ the circular path has transformed into a line. At $x/D = 1.0$ the elliptical shape is yet again visible. Also here, it is evident that the vortex core is stronger when it is in a position further away from the body than when it is close. Finally, at $x/D = 1.55$, we see the same 'U'-shape as we predicted based on the in-situ Fourier transform. We also see, that the vortex

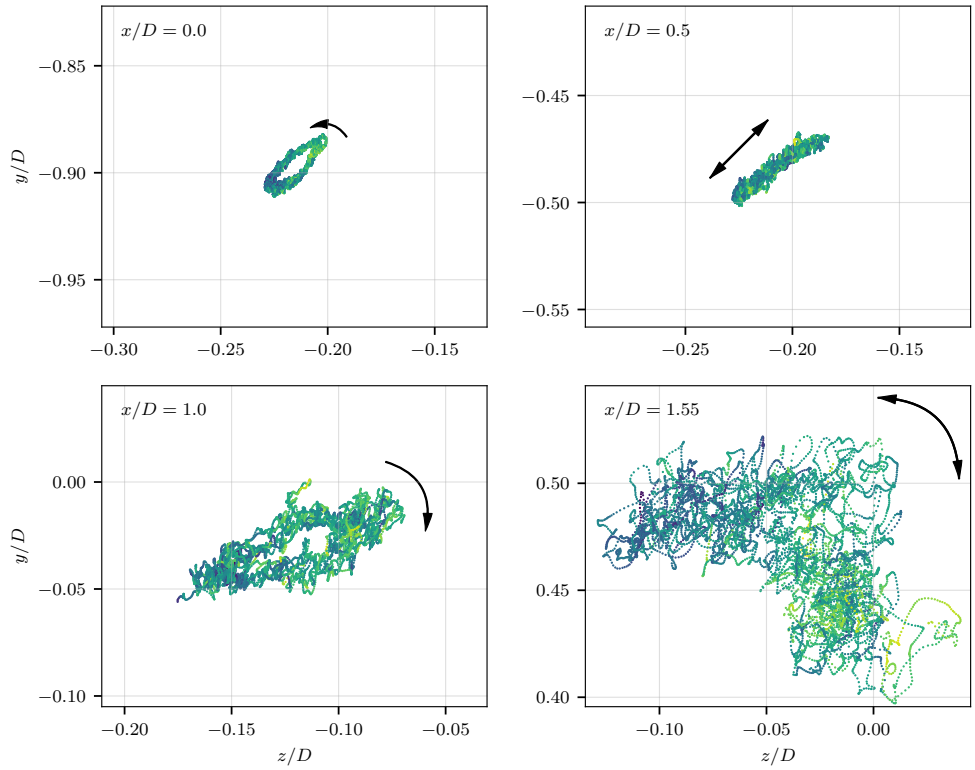

Figure 6: The trajectories of the vortex core in four yz-planes at different x-locations. Each point correspond to the position of the vortex core at one time instance. The color of the point correspond to the pressure of the vortex core. Darker colours (deep blue) indicate lower pressure and stronger suction while lighter colours (yellow) indicate higher pressure and weaker suction. A total of five cycles (100 D/U_∞) are plotted. In all plots, the spheroid is located above and to the right. Arrows indicate direction of path.

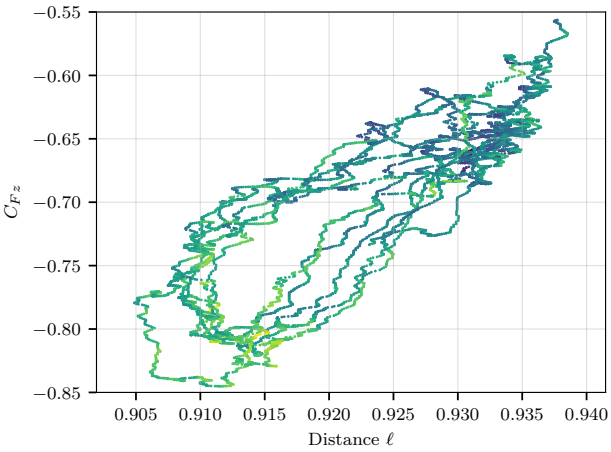

Figure 7: Correlation between the overall sideforce on the spheroid body and the distance from the vortex core to the point $(y, z) = (0, 0)$ in the plane $x/D = 0.0$. The color indicate C_p as described in the caption of fig. 6.

core oscillates both in strength and position. This explains why the two red areas to the left in figure 5 are of different magnitude.

The trajectories of the vortex cores are plotted along with the pressure in an attached animation, from which we unexpectedly notice that the motion of the vortex core is anti-clockwise at $x/D = 0.0$ but clockwise at $x/D = 1.0$. In the plane $x/D = 0.5$ the motion is back and forth a straight path. This interesting observation is also marked with arrows in figure 6. The plots in figure 6 show that the vortex tube is under both a wave type motion in the axial direction and a helical motion, suggesting therefore the three-dimensional vortex instability [15]. The frequency of this instability coincides with the frequency of the overall body forces.

It is furthermore interesting to notice, from figure 6, that the spatial oscillation of the vortex is accompanied by pressure (C_p) variation, meaning the source of the oscillatory body forces may come from either the spatial oscillation or the pressure variation, or the joint effect of them. To clarify this, we plot the correlation between the side force and the vortex core location in plane $x/D = 0.0$ in figure 7. The abscissa is the distance, ℓ, from the center of the spheroid ($(x, y, z) = (0, 0, 0)$) to the vortex core position in the plane $x = 0$. We clearly observe that the side force is stronger as the vortex moves closer to the spheroid, however, the colours in figure 7 indicated that the pressure is higher as the vortex is closer to the spheroid, which seems to be contradictory. Further investigation of C_p and the side force shows no correlation between them. Additionally, we do not find any correlations between C_p in the vortex core at $x/D = 0.0$

and $x/D = 1.0$, at the same instant. This tell us that the variation in pressure in the vortex core is a local phenomenon and does not influence the overall integrated force on the spheroid. Therefore, the oscillatory body force is only caused by the spatial oscillation of the vortex, which is originally induced by the three-dimensional vortex instability.

4 Concluding Remarks

The discovery of the low-frequent forces acting on the 6:1 prolate spheroid at Reynolds number $Re_D = 8000$ is of great importance for manoeuvring capabilities of vehicles. The period of the observed low-frequent phenomenon is four times that of typical vortex shedding from cylinders. This unexpected phenomenon is caused by the cyclic motion of the primary wake vortex, which oscillates both in strength and space. The spatial oscillations seem to be the dominant source of the oscillatory forces, because the variations in strength are in local regions only. The exploration of this phenomenon is still on-going. Simulations at higher Reynolds numbers are in progress, and seems to confirm that the oscillations are still present at higher Re_D.

The phenomenon is similar to the phenomena reported by Ma et al. [9, 10], however, the absence of vortex shedding in the present configuration makes the flow and wake configuration qualitatively different from their results.

5 Acknowledgments

Computing time was granted by UNINETT Sigma2 under project *nn9191k*. F.J. acknowledges the funding from the Future Industry's Leading Technology Development program (No. 10042430) of MOTIE/KEIT of Korea.

References

[1] F. Jiang, J. P. Gallardo and H. I. Andersson. 'The laminar wake behind a 6:1 prolate spheroid at 45° incidence angle'. *Physics of Fluids* 26 (11) (2014), p. 113602. DOI: 10.1063/1.4902015.

[2] F. Jiang, J. P. Gallardo and H. I. Andersson. 'Transition and loss of symmetry in the wake behind an inclined prolate spheroid'. In: *8th National Conference on Computational Mechanics MekIT'15*. Ed. by B. Skallerud and H. I. Andersson. International Center for Numerical Methods in Engineering (CIMNE), Barcelona, Spain, 2015, pp. 219–232.

[3] F. Jiang, J. P. Gallardo, H. I. Andersson and Z. Zhang. 'The transitional wake behind an inclined prolate spheroid'. *Physics of Fluids* 27 (9) (2015), p. 093602. DOI: 10.1063/1.4929764.

[4] F. Jiang, H. I. Andersson, J. P. Gallardo and V. L. Okulov. 'On the peculiar structure of a helical wake vortex behind an inclined prolate spheroid'. *Journal of Fluid Mechanics* 801 (2016), pp. 1–12. DOI: 10.1017/jfm.2016.428.

[5] C. Moskowitz, F. R. Dejarnette and R. M. Hall. 'Effects of nose bluntness, roughness, and surface perturbations on the asymmetric flow past slender bodies at large angles of attack'. In: *7th Applied Aerodynamics Conference*. 1989, p. 2236. DOI: 10.2514/6.1989-2236.

[6] B. Cobleigh. 'High-angle-of-attack yawing moment asymmetry of the X-31 aircraft from flight test'. In: *12th Applied Aerodynamics Conference*. 1994, p. 1803. DOI: 10.2514/6.1994-1803.

[7] A. Ashok, T. Van Buren and A. Smits. 'Asymmetries in the wake of a submarine model in pitch'. *Journal of Fluid Mechanics* 774 (2015), pp. 416–442. DOI: 10.1017/jfm.2015.277.

[8] M. Zeiger, D. Telionis and P. Vlachos. 'Unsteady separated flows over three-dimensional slender bodies'. *Progress in Aerospace Sciences* 40 (4-5) (2004), pp. 291–320. DOI: 10.1016/j.paerosci.2004.06.002.

[9] B.-F. Ma and T.-X. Liu. 'Low-frequency vortex oscillation around slender bodies at high angles-of-attack'. *Physics of Fluids* 26 (9) (2014), p. 091701. DOI: 10.1063/1.4895599.

[10] B.-F. Ma and S.-L. Yin. 'Vortex oscillations around a hemisphere-cylinder body with a high fineness ratio'. *AIAA Journal* 56 (4) (2018), pp. 1402–1420. DOI: 10.2514/1.J056047.

[11] M. Manhart, F. Tremblay and R. Friedrich. 'MGLET: a parallel code for efficient DNS and LES of complex geometries'. In: *Parallel Computational Fluid Dynamics - Trends and*

Applications. Ed. by C. B. Jenssen et al. Elsevier Science B.V., 2001, pp. 449–456. DOI: 10.1016/B978-044450673-3/50123-8.

[12] J. H. Williamson. 'Low-storage Runge-Kutta schemes'. *Journal of Computational Physics* 35 (1) (Mar. 1980), pp. 48–56. DOI: 10.1016/0021-9991(80)90033-9.

[13] N. Peller, A. L. Duc, F. Tremblay and M. Manhart. 'High-order stable interpolations for immersed boundary methods'. *International Journal for Numerical Methods in Fluids* 52 (11) (Apr. 2006), pp. 1175–1193. ISSN: 1097-0363. DOI: 10.1002/fld.1227.

[14] M. Manhart. 'A zonal grid algorithm for DNS of turbulent boundary layers'. *Computers & Fluids* 33 (3) (Mar. 2004), pp. 435–461. ISSN: 0045-7930. DOI: 10.1016/s0045-7930(03)00061-6.

[15] R. L. Ash and M. R. Khorrami. 'Vortex Stability'. In: *Fluid Vortices*. Ed. by S. I. Green. Springer Science+Business Media B.V., 1995, pp. 317–372. DOI: 10.1007/978-94-011-0249-0_8.

Previous PhD theses published at the Department of Marine Technology (earlier: Faculty of Marine Technology) NORWEGIAN UNIVERSITY OF SCIENCE AND TECHNOLOGY

Report No.	Author	Title
	Kavlie, Dag	Optimization of Plane Elastic Grillages, 1967
	Hansen, Hans R.	Man-Machine Communication and Data-Storage Methods in Ship Structural Design, 1971
	Gisvold, Kaare M.	A Method for non-linear mixed -integer programming and its Application to Design Problems, 1971
	Lund, Sverre	Tanker Frame Optimalization by means of SUMT-Transformation and Behaviour Models, 1971
	Vinje, Tor	On Vibration of Spherical Shells Interacting with Fluid, 1972
	Lorentz, Jan D.	Tank Arrangement for Crude Oil Carriers in Accordance with the new Anti-Pollution Regulations, 1975
	Carlsen, Carl A.	Computer-Aided Design of Tanker Structures, 1975
	Larsen, Carl M.	Static and Dynamic Analysis of Offshore Pipelines during Installation, 1976
UR-79-01	Brigt Hatlestad, MK	The finite element method used in a fatigue evaluation of fixed offshore platforms. (Dr.Ing. Thesis)
UR-79-02	Erik Pettersen, MK	Analysis and design of cellular structures. (Dr.Ing. Thesis)
UR-79-03	Sverre Valsgård, MK	Finite difference and finite element methods applied to nonlinear analysis of plated structures. (Dr.Ing. Thesis)
UR-79-04	Nils T. Nordsve, MK	Finite element collapse analysis of structural members considering imperfections and stresses due to fabrication. (Dr.Ing. Thesis)
UR-79-05	Ivar J. Fylling, MK	Analysis of towline forces in ocean towing systems. (Dr.Ing. Thesis)
UR-80-06	Nils Sandsmark, MM	Analysis of Stationary and Transient Heat Conduction by the Use of the Finite Element Method. (Dr.Ing. Thesis)
UR-80-09	Sverre Haver, MK	Analysis of uncertainties related to the stochastic modeling of ocean waves. (Dr.Ing. Thesis)
UR-81-15	Odland, Jonas	On the Strength of welded Ring stiffened cylindrical Shells primarily subjected to axial Compression
UR-82-17	Engesvik, Knut	Analysis of Uncertainties in the fatigue Capacity of

		Welded Joints
UR-82-18	Rye, Henrik	Ocean wave groups
UR-83-30	Eide, Oddvar Inge	On Cumulative Fatigue Damage in Steel Welded Joints
UR-83-33	Mo, Olav	Stochastic Time Domain Analysis of Slender Offshore Structures
UR-83-34	Amdahl, Jørgen	Energy absorption in Ship-platform impacts
UR-84-37	Mørch, Morten	Motions and mooring forces of semi submersibles as determined by full-scale measurements and theoretical analysis
UR-84-38	Soares, C. Guedes	Probabilistic models for load effects in ship structures
UR-84-39	Aarsnes, Jan V.	Current forces on ships
UR-84-40	Czujko, Jerzy	Collapse Analysis of Plates subjected to Biaxial Compression and Lateral Load
UR-85-46	Alf G. Engseth, MK	Finite element collapse analysis of tubular steel offshore structures. (Dr.Ing. Thesis)
UR-86-47	Dengody Sheshappa, MP	A Computer Design Model for Optimizing Fishing Vessel Designs Based on Techno-Economic Analysis. (Dr.Ing. Thesis)
UR-86-48	Vidar Aanesland, MH	A Theoretical and Numerical Study of Ship Wave Resistance. (Dr.Ing. Thesis)
UR-86-49	Heinz-Joachim Wessel, MK	Fracture Mechanics Analysis of Crack Growth in Plate Girders. (Dr.Ing. Thesis)
UR-86-50	Jon Taby, MK	Ultimate and Post-ultimate Strength of Dented Tubular Members. (Dr.Ing. Thesis)
UR-86-51	Walter Lian, MH	A Numerical Study of Two-Dimensional Separated Flow Past Bluff Bodies at Moderate KC-Numbers. (Dr.Ing. Thesis)
UR-86-52	Bjørn Sortland, MH	Force Measurements in Oscillating Flow on Ship Sections and Circular Cylinders in a U-Tube Water Tank. (Dr.Ing. Thesis)
UR-86-53	Kurt Strand, MM	A System Dynamic Approach to One-dimensional Fluid Flow. (Dr.Ing. Thesis)
UR-86-54	Arne Edvin Løken, MH	Three Dimensional Second Order Hydrodynamic Effects on Ocean Structures in Waves. (Dr.Ing. Thesis)
UR-86-55	Sigurd Falch, MH	A Numerical Study of Slamming of Two-Dimensional Bodies. (Dr.Ing. Thesis)
UR-87-56	Arne Braathen, MH	Application of a Vortex Tracking Method to the Prediction of Roll Damping of a Two-Dimension Floating Body. (Dr.Ing. Thesis)

UR-87-57	Bernt Leira, MK	Gaussian Vector Processes for Reliability Analysis involving Wave-Induced Load Effects. (Dr.Ing. Thesis)
UR-87-58	Magnus Småvik, MM	Thermal Load and Process Characteristics in a Two-Stroke Diesel Engine with Thermal Barriers (in Norwegian). (Dr.Ing. Thesis)
MTA-88-59	Bernt Arild Bremdal, MP	An Investigation of Marine Installation Processes – A Knowledge - Based Planning Approach. (Dr.Ing. Thesis)
MTA-88-60	Xu Jun, MK	Non-linear Dynamic Analysis of Space-framed Offshore Structures. (Dr.Ing. Thesis)
MTA-89-61	Gang Miao, MH	Hydrodynamic Forces and Dynamic Responses of Circular Cylinders in Wave Zones. (Dr.Ing. Thesis)
MTA-89-62	Martin Greenhow, MH	Linear and Non-Linear Studies of Waves and Floating Bodies. Part I and Part II. (Dr.Techn. Thesis)
MTA-89-63	Chang Li, MH	Force Coefficients of Spheres and Cubes in Oscillatory Flow with and without Current. (Dr.Ing. Thesis
MTA-89-64	Hu Ying, MP	A Study of Marketing and Design in Development of Marine Transport Systems. (Dr.Ing. Thesis)
MTA-89-65	Arild Jæger, MH	Seakeeping, Dynamic Stability and Performance of a Wedge Shaped Planing Hull. (Dr.Ing. Thesis)
MTA-89-66	Chan Siu Hung, MM	The dynamic characteristics of tilting-pad bearings
MTA-89-67	Kim Wikstrøm, MP	Analysis av projekteringen for ett offshore projekt. (Licenciat-avhandling)
MTA-89-68	Jiao Guoyang, MK	Reliability Analysis of Crack Growth under Random Loading, considering Model Updating. (Dr.Ing. Thesis)
MTA-89-69	Arnt Olufsen, MK	Uncertainty and Reliability Analysis of Fixed Offshore Structures. (Dr.Ing. Thesis)
MTA-89-70	Wu Yu-Lin, MR	System Reliability Analyses of Offshore Structures using improved Truss and Beam Models. (Dr.Ing. Thesis)
MTA-90-71	Jan Roger Hoff, MH	Three-dimensional Green function of a vessel with forward speed in waves. (Dr.Ing. Thesis)
MTA-90-72	Rong Zhao, MH	Slow-Drift Motions of a Moored Two-Dimensional Body in Irregular Waves. (Dr.Ing. Thesis)
MTA-90-73	Atle Minsaas, MP	Economical Risk Analysis. (Dr.Ing. Thesis)
MTA-90-74	Knut-Aril Farnes, MK	Long-term Statistics of Response in Non-linear Marine Structures. (Dr.Ing. Thesis)
MTA-90-75	Torbjørn Sotberg, MK	Application of Reliability Methods for Safety Assessment of Submarine Pipelines. (Dr.Ing.

		Thesis)
MTA-90-76	Zeuthen, Steffen, MP	SEAMAID. A computational model of the design process in a constraint-based logic programming environment. An example from the offshore domain. (Dr.Ing. Thesis)
MTA-91-77	Haagensen, Sven, MM	Fuel Dependant Cyclic Variability in a Spark Ignition Engine - An Optical Approach. (Dr.Ing. Thesis)
MTA-91-78	Løland, Geir, MH	Current forces on and flow through fish farms. (Dr.Ing. Thesis)
MTA-91-79	Hoen, Christopher, MK	System Identification of Structures Excited by Stochastic Load Processes. (Dr.Ing. Thesis)
MTA-91-80	Haugen, Stein, MK	Probabilistic Evaluation of Frequency of Collision between Ships and Offshore Platforms. (Dr.Ing. Thesis)
MTA-91-81	Sødahl, Nils, MK	Methods for Design and Analysis of Flexible Risers. (Dr.Ing. Thesis)
MTA-91-82	Ormberg, Harald, MK	Non-linear Response Analysis of Floating Fish Farm Systems. (Dr.Ing. Thesis)
MTA-91-83	Marley, Mark J., MK	Time Variant Reliability under Fatigue Degradation. (Dr.Ing. Thesis)
MTA-91-84	Krokstad, Jørgen R., MH	Second-order Loads in Multidirectional Seas. (Dr.Ing. Thesis)
MTA-91-85	Molteberg, Gunnar A., MM	The Application of System Identification Techniques to Performance Monitoring of Four Stroke Turbocharged Diesel Engines. (Dr.Ing. Thesis)
MTA-92-86	Mørch, Hans Jørgen Bjelke, MH	Aspects of Hydrofoil Design: with Emphasis on Hydrofoil Interaction in Calm Water. (Dr.Ing. Thesis)
MTA-92-87	Chan Siu Hung, MM	Nonlinear Analysis of Rotordynamic Instabilities in Highspeed Turbomachinery. (Dr.Ing. Thesis)
MTA-92-88	Bessason, Bjarni, MK	Assessment of Earthquake Loading and Response of Seismically Isolated Bridges. (Dr.Ing. Thesis)
MTA-92-89	Langli, Geir, MP	Improving Operational Safety through exploitation of Design Knowledge - an investigation of offshore platform safety. (Dr.Ing. Thesis)
MTA-92-90	Sævik, Svein, MK	On Stresses and Fatigue in Flexible Pipes. (Dr.Ing. Thesis)
MTA-92-91	Ask, Tor Ø., MM	Ignition and Flame Growth in Lean Gas-Air Mixtures. An Experimental Study with a Schlieren System. (Dr.Ing. Thesis)
MTA-86-92	Hessen, Gunnar, MK	Fracture Mechanics Analysis of Stiffened Tubular Members. (Dr.Ing. Thesis)

MTA-93-93	Steinebach, Christian, MM	Knowledge Based Systems for Diagnosis of Rotating Machinery. (Dr.Ing. Thesis)
MTA-93-94	Dalane, Jan Inge, MK	System Reliability in Design and Maintenance of Fixed Offshore Structures. (Dr.Ing. Thesis)
MTA-93-95	Steen, Sverre, MH	Cobblestone Effect on SES. (Dr.Ing. Thesis)
MTA-93-96	Karunakaran, Daniel, MK	Nonlinear Dynamic Response and Reliability Analysis of Drag-dominated Offshore Platforms. (Dr.Ing. Thesis)
MTA-93-97	Hagen, Arnulf, MP	The Framework of a Design Process Language. (Dr.Ing. Thesis)
MTA-93-98	Nordrik, Rune, MM	Investigation of Spark Ignition and Autoignition in Methane and Air Using Computational Fluid Dynamics and Chemical Reaction Kinetics. A Numerical Study of Ignition Processes in Internal Combustion Engines. (Dr.Ing. Thesis)
MTA-94-99	Passano, Elizabeth, MK	Efficient Analysis of Nonlinear Slender Marine Structures. (Dr.Ing. Thesis)
MTA-94-100	Kvålsvold, Jan, MH	Hydroelastic Modelling of Wetdeck Slamming on Multihull Vessels. (Dr.Ing. Thesis)
MTA-94-102	Bech, Sidsel M., MK	Experimental and Numerical Determination of Stiffness and Strength of GRP/PVC Sandwich Structures. (Dr.Ing. Thesis)
MTA-95-103	Paulsen, Hallvard, MM	A Study of Transient Jet and Spray using a Schlieren Method and Digital Image Processing. (Dr.Ing. Thesis)
MTA-95-104	Hovde, Geir Olav, MK	Fatigue and Overload Reliability of Offshore Structural Systems, Considering the Effect of Inspection and Repair. (Dr.Ing. Thesis)
MTA-95-105	Wang, Xiaozhi, MK	Reliability Analysis of Production Ships with Emphasis on Load Combination and Ultimate Strength. (Dr.Ing. Thesis)
MTA-95-106	Ulstein, Tore, MH	Nonlinear Effects of a Flexible Stern Seal Bag on Cobblestone Oscillations of an SES. (Dr.Ing. Thesis)
MTA-95-107	Solaas, Frøydis, MH	Analytical and Numerical Studies of Sloshing in Tanks. (Dr.Ing. Thesis)
MTA-95-108	Hellan, Øyvind, MK	Nonlinear Pushover and Cyclic Analyses in Ultimate Limit State Design and Reassessment of Tubular Steel Offshore Structures. (Dr.Ing. Thesis)
MTA-95-109	Hermundstad, Ole A., MK	Theoretical and Experimental Hydroelastic Analysis of High Speed Vessels. (Dr.Ing. Thesis)
MTA-96-110	Bratland, Anne K., MH	Wave-Current Interaction Effects on Large-Volume Bodies in Water of Finite Depth. (Dr.Ing. Thesis)

MTA-96-111	Herfjord, Kjell, MH	A Study of Two-dimensional Separated Flow by a Combination of the Finite Element Method and Navier-Stokes Equations. (Dr.Ing. Thesis)
MTA-96-112	Æsøy, Vilmar, MM	Hot Surface Assisted Compression Ignition in a Direct Injection Natural Gas Engine. (Dr.Ing. Thesis)
MTA-96-113	Eknes, Monika L., MK	Escalation Scenarios Initiated by Gas Explosions on Offshore Installations. (Dr.Ing. Thesis)
MTA-96-114	Erikstad, Stein O., MP	A Decision Support Model for Preliminary Ship Design. (Dr.Ing. Thesis)
MTA-96-115	Pedersen, Egil, MH	A Nautical Study of Towed Marine Seismic Streamer Cable Configurations. (Dr.Ing. Thesis)
MTA-97-116	Moksnes, Paul O., MM	Modelling Two-Phase Thermo-Fluid Systems Using Bond Graphs. (Dr.Ing. Thesis)
MTA-97-117	Halse, Karl H., MK	On Vortex Shedding and Prediction of Vortex-Induced Vibrations of Circular Cylinders. (Dr.Ing. Thesis)
MTA-97-118	Igland, Ragnar T., MK	Reliability Analysis of Pipelines during Laying, considering Ultimate Strength under Combined Loads. (Dr.Ing. Thesis)
MTA-97-119	Pedersen, Hans-P., MP	Levendefiskteknologi for fiskefartøy. (Dr.Ing. Thesis)
MTA-98-120	Vikestad, Kyrre, MK	Multi-Frequency Response of a Cylinder Subjected to Vortex Shedding and Support Motions. (Dr.Ing. Thesis)
MTA-98-121	Azadi, Mohammad R. E., MK	Analysis of Static and Dynamic Pile-Soil-Jacket Behaviour. (Dr.Ing. Thesis)
MTA-98-122	Ulltang, Terje, MP	A Communication Model for Product Information. (Dr.Ing. Thesis)
MTA-98-123	Torbergsen, Erik, MM	Impeller/Diffuser Interaction Forces in Centrifugal Pumps. (Dr.Ing. Thesis)
MTA-98-124	Hansen, Edmond, MH	A Discrete Element Model to Study Marginal Ice Zone Dynamics and the Behaviour of Vessels Moored in Broken Ice. (Dr.Ing. Thesis)
MTA-98-125	Videiro, Paulo M., MK	Reliability Based Design of Marine Structures. (Dr.Ing. Thesis)
MTA-99-126	Mainçon, Philippe, MK	Fatigue Reliability of Long Welds Application to Titanium Risers. (Dr.Ing. Thesis)
MTA-99-127	Haugen, Elin M., MH	Hydroelastic Analysis of Slamming on Stiffened Plates with Application to Catamaran Wetdecks. (Dr.Ing. Thesis)
MTA-99-128	Langhelle, Nina K., MK	Experimental Validation and Calibration of Nonlinear Finite Element Models for Use in Design of Aluminium Structures Exposed to Fire. (Dr.Ing.

		Thesis)
MTA-99-129	Berstad, Are J., MK	Calculation of Fatigue Damage in Ship Structures. (Dr.Ing. Thesis)
MTA-99-130	Andersen, Trond M., MM	Short Term Maintenance Planning. (Dr.Ing. Thesis)
MTA-99-131	Tveiten, Bård Wathne, MK	Fatigue Assessment of Welded Aluminium Ship Details. (Dr.Ing. Thesis)
MTA-99-132	Søreide, Fredrik, MP	Applications of underwater technology in deep water archaeology. Principles and practice. (Dr.Ing. Thesis)
MTA-99-133	Tønnessen, Rune, MH	A Finite Element Method Applied to Unsteady Viscous Flow Around 2D Blunt Bodies With Sharp Corners. (Dr.Ing. Thesis)
MTA-99-134	Elvekrok, Dag R., MP	Engineering Integration in Field Development Projects in the Norwegian Oil and Gas Industry. The Supplier Management of Norne. (Dr.Ing. Thesis)
MTA-99-135	Fagerholt, Kjetil, MP	Optimeringsbaserte Metoder for Ruteplanlegging innen skipsfart. (Dr.Ing. Thesis)
MTA-99-136	Bysveen, Marie, MM	Visualization in Two Directions on a Dynamic Combustion Rig for Studies of Fuel Quality. (Dr.Ing. Thesis)
MTA-2000-137	Storteig, Eskild, MM	Dynamic characteristics and leakage performance of liquid annular seals in centrifugal pumps. (Dr.Ing. Thesis)
MTA-2000-138	Sagli, Gro, MK	Model uncertainty and simplified estimates of long term extremes of hull girder loads in ships. (Dr.Ing. Thesis)
MTA-2000-139	Tronstad, Harald, MK	Nonlinear analysis and design of cable net structures like fishing gear based on the finite element method. (Dr.Ing. Thesis)
MTA-2000-140	Kroneberg, André, MP	Innovation in shipping by using scenarios. (Dr.Ing. Thesis)
MTA-2000-141	Haslum, Herbjørn Alf, MH	Simplified methods applied to nonlinear motion of spar platforms. (Dr.Ing. Thesis)
MTA-2001-142	Samdal, Ole Johan, MM	Modelling of Degradation Mechanisms and Stressor Interaction on Static Mechanical Equipment Residual Lifetime. (Dr.Ing. Thesis)
MTA-2001-143	Baarholm, Rolf Jarle, MH	Theoretical and experimental studies of wave impact underneath decks of offshore platforms. (Dr.Ing. Thesis)
MTA-2001-144	Wang, Lihua, MK	Probabilistic Analysis of Nonlinear Wave-induced Loads on Ships. (Dr.Ing. Thesis)
MTA-2001-145	Kristensen, Odd H. Holt, MK	Ultimate Capacity of Aluminium Plates under Multiple Loads, Considering HAZ Properties.

		(Dr.Ing. Thesis)
MTA-2001-146	Greco, Marilena, MH	A Two-Dimensional Study of Green-Water Loading. (Dr.Ing. Thesis)
MTA-2001-147	Heggelund, Svein E., MK	Calculation of Global Design Loads and Load Effects in Large High Speed Catamarans. (Dr.Ing. Thesis)
MTA-2001-148	Babalola, Olusegun T., MK	Fatigue Strength of Titanium Risers – Defect Sensitivity. (Dr.Ing. Thesis)
MTA-2001-149	Mohammed, Abuu K., MK	Nonlinear Shell Finite Elements for Ultimate Strength and Collapse Analysis of Ship Structures. (Dr.Ing. Thesis)
MTA-2002-150	Holmedal, Lars E., MH	Wave-current interactions in the vicinity of the sea bed. (Dr.Ing. Thesis)
MTA-2002-151	Rognebakke, Olav F., MH	Sloshing in rectangular tanks and interaction with ship motions. (Dr.Ing. Thesis)
MTA-2002-152	Lader, Pål Furset, MH	Geometry and Kinematics of Breaking Waves. (Dr.Ing. Thesis)
MTA-2002-153	Yang, Qinzheng, MH	Wash and wave resistance of ships in finite water depth. (Dr.Ing. Thesis)
MTA-2002-154	Melhus, Øyvin, MM	Utilization of VOC in Diesel Engines. Ignition and combustion of VOC released by crude oil tankers. (Dr.Ing. Thesis)
MTA-2002-155	Ronæss, Marit, MH	Wave Induced Motions of Two Ships Advancing on Parallel Course. (Dr.Ing. Thesis)
MTA-2002-156	Økland, Ole D., MK	Numerical and experimental investigation of whipping in twin hull vessels exposed to severe wet deck slamming. (Dr.Ing. Thesis)
MTA-2002-157	Ge, Chunhua, MK	Global Hydroelastic Response of Catamarans due to Wet Deck Slamming. (Dr.Ing. Thesis)
MTA-2002-158	Byklum, Eirik, MK	Nonlinear Shell Finite Elements for Ultimate Strength and Collapse Analysis of Ship Structures. (Dr.Ing. Thesis)
IMT-2003-1	Chen, Haibo, MK	Probabilistic Evaluation of FPSO-Tanker Collision in Tandem Offloading Operation. (Dr.Ing. Thesis)
IMT-2003-2	Skaugset, Kjetil Bjørn, MK	On the Suppression of Vortex Induced Vibrations of Circular Cylinders by Radial Water Jets. (Dr.Ing. Thesis)
IMT-2003-3	Chezhian, Muthu	Three-Dimensional Analysis of Slamming. (Dr.Ing. Thesis)
IMT-2003-4	Buhaug, Øyvind	Deposit Formation on Cylinder Liner Surfaces in Medium Speed Engines. (Dr.Ing. Thesis)
IMT-2003-5	Tregde, Vidar	Aspects of Ship Design: Optimization of Aft Hull with Inverse Geometry Design. (Dr.Ing. Thesis)

IMT-2003-6	Wist, Hanne Therese	Statistical Properties of Successive Ocean Wave Parameters. (Dr.Ing. Thesis)
IMT-2004-7	Ransau, Samuel	Numerical Methods for Flows with Evolving Interfaces. (Dr.Ing. Thesis)
IMT-2004-8	Soma, Torkel	Blue-Chip or Sub-Standard. A data interrogation approach of identity safety characteristics of shipping organization. (Dr.Ing. Thesis)
IMT-2004-9	Ersdal, Svein	An experimental study of hydrodynamic forces on cylinders and cables in near axial flow. (Dr.Ing. Thesis)
IMT-2005-10	Brodtkorb, Per Andreas	The Probability of Occurrence of Dangerous Wave Situations at Sea. (Dr.Ing. Thesis)
IMT-2005-11	Yttervik, Rune	Ocean current variability in relation to offshore engineering. (Dr.Ing. Thesis)
IMT-2005-12	Fredheim, Arne	Current Forces on Net-Structures. (Dr.Ing. Thesis)
IMT-2005-13	Heggernes, Kjetil	Flow around marine structures. (Dr.Ing. Thesis
IMT-2005-14	Fouques, Sebastien	Lagrangian Modelling of Ocean Surface Waves and Synthetic Aperture Radar Wave Measurements. (Dr.Ing. Thesis)
IMT-2006-15	Holm, Håvard	Numerical calculation of viscous free surface flow around marine structures. (Dr.Ing. Thesis)
IMT-2006-16	Bjørheim, Lars G.	Failure Assessment of Long Through Thickness Fatigue Cracks in Ship Hulls. (Dr.Ing. Thesis)
IMT-2006-17	Hansson, Lisbeth	Safety Management for Prevention of Occupational Accidents. (Dr.Ing. Thesis)
IMT-2006-18	Zhu, Xinying	Application of the CIP Method to Strongly Nonlinear Wave-Body Interaction Problems. (Dr.Ing. Thesis)
IMT-2006-19	Reite, Karl Johan	Modelling and Control of Trawl Systems. (Dr.Ing. Thesis)
IMT-2006-20	Smogeli, Øyvind Notland	Control of Marine Propellers. From Normal to Extreme Conditions. (Dr.Ing. Thesis)
IMT-2007-21	Storhaug, Gaute	Experimental Investigation of Wave Induced Vibrations and Their Effect on the Fatigue Loading of Ships. (Dr.Ing. Thesis)
IMT-2007-22	Sun, Hui	A Boundary Element Method Applied to Strongly Nonlinear Wave-Body Interaction Problems. (PhD Thesis, CeSOS)
IMT-2007-23	Rustad, Anne Marthine	Modelling and Control of Top Tensioned Risers. (PhD Thesis, CeSOS)
IMT-2007-24	Johansen, Vegar	Modelling flexible slender system for real-time

		simulations and control applications
IMT-2007-25	Wroldsen, Anders Sunde	Modelling and control of tensegrity structures. (PhD Thesis, CeSOS)
IMT-2007-26	Aronsen, Kristoffer Høye	An experimental investigation of in-line and combined inline and cross flow vortex induced vibrations. (Dr. avhandling, IMT)
IMT-2007-27	Gao, Zhen	Stochastic Response Analysis of Mooring Systems with Emphasis on Frequency-domain Analysis of Fatigue due to Wide-band Response Processes (PhD Thesis, CeSOS)
IMT-2007-28	Thorstensen, Tom Anders	Lifetime Profit Modelling of Ageing Systems Utilizing Information about Technical Condition. (Dr.ing. thesis, IMT)
IMT-2008-29	Refsnes, Jon Erling Gorset	Nonlinear Model-Based Control of Slender Body AUVs (PhD Thesis, IMT)
IMT-2008-30	Berntsen, Per Ivar B.	Structural Reliability Based Position Mooring. (PhD-Thesis, IMT)
IMT-2008-31	Ye, Naiquan	Fatigue Assessment of Aluminium Welded Box-stiffener Joints in Ships (Dr.ing. thesis, IMT)
IMT-2008-32	Radan, Damir	Integrated Control of Marine Electrical Power Systems. (PhD-Thesis, IMT)
IMT-2008-33	Thomassen, Paul	Methods for Dynamic Response Analysis and Fatigue Life Estimation of Floating Fish Cages. (Dr.ing. thesis, IMT)
IMT-2008-34	Pákozdi, Csaba	A Smoothed Particle Hydrodynamics Study of Two-dimensional Nonlinear Sloshing in Rectangular Tanks. (Dr.ing.thesis, IMT/ CeSOS)
IMT-2007-35	Grytøyr, Guttorm	A Higher-Order Boundary Element Method and Applications to Marine Hydrodynamics. (Dr.ing.thesis, IMT)
IMT-2008-36	Drummen, Ingo	Experimental and Numerical Investigation of Nonlinear Wave-Induced Load Effects in Containerships considering Hydroelasticity. (PhD thesis, CeSOS)
IMT-2008-37	Skejic, Renato	Maneuvering and Seakeeping of a Singel Ship and of Two Ships in Interaction. (PhD-Thesis, CeSOS)
IMT-2008-38	Harlem, Alf	An Age-Based Replacement Model for Repairable Systems with Attention to High-Speed Marine Diesel Engines. (PhD-Thesis, IMT)
IMT-2008-39	Alsos, Hagbart S.	Ship Grounding. Analysis of Ductile Fracture, Bottom Damage and Hull Girder Response. (PhD-thesis, IMT)
IMT-2008-40	Graczyk, Mateusz	Experimental Investigation of Sloshing Loading and Load Effects in Membrane LNG Tanks Subjected to Random Excitation. (PhD-thesis, CeSOS)

IMT-2008-41	Taghipour, Reza	Efficient Prediction of Dynamic Response for Flexible amd Multi-body Marine Structures. (PhD-thesis, CeSOS)
IMT-2008-42	Ruth, Eivind	Propulsion control and thrust allocation on marine vessels. (PhD thesis, CeSOS)
IMT-2008-43	Nystad, Bent Helge	Technical Condition Indexes and Remaining Useful Life of Aggregated Systems. PhD thesis, IMT
IMT-2008-44	Soni, Prashant Kumar	Hydrodynamic Coefficients for Vortex Induced Vibrations of Flexible Beams, PhD thesis, CeSOS
IMT-2009-45	Amlashi, Hadi K.K.	Ultimate Strength and Reliability-based Design of Ship Hulls with Emphasis on Combined Global and Local Loads. PhD Thesis, IMT
IMT-2009-46	Pedersen, Tom Arne	Bond Graph Modelling of Marine Power Systems. PhD Thesis, IMT
IMT-2009-47	Kristiansen, Trygve	Two-Dimensional Numerical and Experimental Studies of Piston-Mode Resonance. PhD-Thesis, CeSOS
IMT-2009-48	Ong, Muk Chen	Applications of a Standard High Reynolds Number Model and a Stochastic Scour Prediction Model for Marine Structures. PhD-thesis, IMT
IMT-2009-49	Hong, Lin	Simplified Analysis and Design of Ships subjected to Collision and Grounding. PhD-thesis, IMT
IMT-2009-50	Koushan, Kamran	Vortex Induced Vibrations of Free Span Pipelines, PhD thesis, IMT
IMT-2009-51	Korsvik, Jarl Eirik	Heuristic Methods for Ship Routing and Scheduling. PhD-thesis, IMT
IMT-2009-52	Lee, Jihoon	Experimental Investigation and Numerical in Analyzing the Ocean Current Displacement of Longlines. Ph.d.-Thesis, IMT.
IMT-2009-53	Vestbøstad, Tone Gran	A Numerical Study of Wave-in-Deck Impact usin a Two-Dimensional Constrained Interpolation Profile Method, Ph.d.thesis, CeSOS.
IMT-2009-54	Bruun, Kristine	Bond Graph Modelling of Fuel Cells for Marine Power Plants. Ph.d.-thesis, IMT
IMT 2009-55	Holstad, Anders	Numerical Investigation of Turbulence in a Sekwed Three-Dimensional Channel Flow, Ph.d.-thesis, IMT.
IMT 2009-56	Ayala-Uraga, Efren	Reliability-Based Assessment of Deteriorating Ship-shaped Offshore Structures, Ph.d.-thesis, IMT
IMT 2009-57	Kong, Xiangjun	A Numerical Study of a Damaged Ship in Beam Sea Waves. Ph.d.-thesis, IMT/CeSOS.
IMT 2010-58	Kristiansen, David	Wave Induced Effects on Floaters of Aquaculture Plants, Ph.d.-thesis, CeSOS.

IMT 2010-59	Ludvigsen, Martin	An ROV-Toolbox for Optical and Acoustic Scientific Seabed Investigation. Ph.d.-thesis IMT.
IMT 2010-60	Hals, Jørgen	Modelling and Phase Control of Wave-Energy Converters. Ph.d.thesis, CeSOS.
IMT 2010- 61	Shu, Zhi	Uncertainty Assessment of Wave Loads and Ultimate Strength of Tankers and Bulk Carriers in a Reliability Framework. Ph.d. Thesis, IMT/ CeSOS
IMT 2010-62	Shao, Yanlin	Numerical Potential-Flow Studies on Weakly-Nonlinear Wave-Body Interactions with/without Small Forward Speed, Ph.d.thesis,CeSOS.
IMT 2010-63	Califano, Andrea	Dynamic Loads on Marine Propellers due to Intermittent Ventilation. Ph.d.thesis, IMT.
IMT 2010-64	El Khoury, George	Numerical Simulations of Massively Separated Turbulent Flows, Ph.d.-thesis, IMT
IMT 2010-65	Seim, Knut Sponheim	Mixing Process in Dense Overflows with Emphasis on the Faroe Bank Channel Overflow. Ph.d.thesis, IMT
IMT 2010-66	Jia, Huirong	Structural Analysis of Intect and Damaged Ships in a Collission Risk Analysis Perspective. Ph.d.thesis CeSoS.
IMT 2010-67	Jiao, Linlin	Wave-Induced Effects on a Pontoon-type Very Large Floating Structures (VLFS). Ph.D.-thesis, CeSOS.
IMT 2010-68	Abrahamsen, Bjørn Christian	Sloshing Induced Tank Roof with Entrapped Air Pocket. Ph.d.thesis, CeSOS.
IMT 2011-69	Karimirad, Madjid	Stochastic Dynamic Response Analysis of Spar-Type Wind Turbines with Catenary or Taut Mooring Systems. Ph.d.-thesis, CeSOS.
IMT -2011-70	Erlend Meland	Condition Monitoring of Safety Critical Valves. Ph.d.-thesis, IMT.
IMT – 2011-71	Yang, Limin	Stochastic Dynamic System Analysis of Wave Energy Converter with Hydraulic Power Take-Off, with Particular Reference to Wear Damage Analysis, Ph.d. Thesis, CeSOS.
IMT – 2011-72	Visscher, Jan	Application of Particla Image Velocimetry on Turbulent Marine Flows, Ph.d.Thesis, IMT.
IMT – 2011-73	Su, Biao	Numerical Predictions of Global and Local Ice Loads on Ships. Ph.d.Thesis, CeSOS.
IMT – 2011-74	Liu, Zhenhui	Analytical and Numerical Analysis of Iceberg Collision with Ship Structures. Ph.d.Thesis, IMT.
IMT – 2011-75	Aarsæther, Karl Gunnar	Modeling and Analysis of Ship Traffic by Observation and Numerical Simulation. Ph.d.Thesis, IMT.
IMT – 2011-76	Wu, Jie	Hydrodynamic Force Identification from Stochastic Vortex Induced Vibration Experiments with

		Slender Beams. Ph.d.Thesis, IMT.
IMT– 2011-77	Amini, Hamid	Azimuth Propulsors in Off-design Conditions. Ph.d.Thesis, IMT.
IMT –2011-78	Nguyen, Tan-Hoi	Toward a System of Real-Time Prediction and Monitoring of Bottom Damage Conditions During Ship Grounding. Ph.d.thesis, IMT.
IMT- 2011-79	Tavakoli, Mohammad T.	Assessment of Oil Spill in Ship Collision and Grounding, Ph.d.thesis, IMT.
IMT- 2011-80	Guo, Bingjie	Numerical and Experimental Investigation of Added Resistance in Waves. Ph.d.Thesis, IMT.
IMT- 2011-81	Chen, Qiaofeng	Ultimate Strength of Aluminium Panels, considering HAZ Effects, IMT
IMT-2012-82	Kota, Ravikiran S.	Wave Loads on Decks of Offshore Structures in Random Seas, CeSOS.
IMT-2012-83	Sten, Ronny	Dynamic Simulation of Deep Water Drilling Risers with Heave Compensating System, IMT.
IMT-2012-84	Berle, Øyvind	Risk and resilience in global maritime supply chains, IMT.
IMT-2012-85	Fang, Shaoji	Fault Tolerant Position Mooring Control Based on Structural Reliability, CeSOS.
IMT-2012-86	You, Jikun	Numerical studies on wave forces and moored ship motions in intermediate and shallow water, CeSOS.
IMT-2012-87	Xiang ,Xu	Maneuvering of two interacting ships in waves, CeSOS
IMT-2012-88	Dong, Wenbin	Time-domain fatigue response and reliability analysis of offshore wind turbines with emphasis on welded tubular joints and gear components, CeSOS
IMT-2012-89	Zhu, Suji	Investigation of Wave-Induced Nonlinear Load Effects in Open Ships considering Hull Girder Vibrations in Bending and Torsion, CeSOS
IMT-2012-90	Zhou, Li	Numerical and Experimental Investigation of Station-keeping in Level Ice, CeSOS
IMT-2012-91	Ushakov, Sergey	Particulate matter emission characteristics from diesel enignes operating on conventional and alternative marine fuels, IMT
IMT-2013-1	Yin, Decao	Experimental and Numerical Analysis of Combined In-line and Cross-flow Vortex Induced Vibrations, CeSOS
IMT-2013-2	Kurniawan, Adi	Modelling and geometry optimisation of wave energy converters, CeSOS

IMT- 2013-3	Al Ryati, Nabil	Technical condition indexes doe auxiliary marine diesel engines, IMT
IMT-2013-4	Firoozkoohi, Reza	Experimental, numerical and analytical investigation of the effect of screens on sloshing, CeSOS
IMT-2013-5	Ommani, Babak	Potential-Flow Predictions of a Semi-Displacement Vessel Including Applications to Calm Water Broaching, CeSOS
IMT- 2013-6	Xing, Yihan	Modelling and analysis of the gearbox in a floating spar-type wind turbine, CeSOS
IMT-7-2013	Balland, Océane	Optimization models for reducing air emissions from ships, IMT
IMT-8-2013	Yang, Dan	Transitional wake flow behind an inclined flat plate-----Computation and analysis, IMT
IMT-9-2013	Abdillah, Suyuthi	Prediction of Extreme Loads and Fatigue Damage for a Ship Hull due to Ice Action, IMT
IMT-10-2013	Ramìrez, Pedro Agustìn Pèrez	Ageing management and life extension of technical systems- Concepts and methods applied to oil and gas facilities, IMT
IMT-11-2013	Chuang, Zhenju	Experimental and Numerical Investigation of Speed Loss due to Seakeeping and Maneuvering. IMT
IMT-12-2013	Etemaddar, Mahmoud	Load and Response Analysis of Wind Turbines under Atmospheric Icing and Controller System Faults with Emphasis on Spar Type Floating Wind Turbines, IMT
IMT-13-2013	Lindstad, Haakon	Strategies and measures for reducing maritime CO2 emissons, IMT
IMT-14-2013	Haris, Sabril	Damage interaction analysis of ship collisions, IMT
IMT-15-2013	Shainee, Mohamed	Conceptual Design, Numerical and Experimental Investigation of a SPM Cage Concept for Offshore Mariculture, IMT
IMT-16-2013	Gansel, Lars	Flow past porous cylinders and effects of biofouling and fish behavior on the flow in and around Atlantic salmon net cages, IMT
IMT-17-2013	Gaspar, Henrique	Handling Aspects of Complexity in Conceptual Ship Design, IMT
IMT-18-2013	Thys, Maxime	Theoretical and Experimental Investigation of a Free Running Fishing Vessel at Small Frequency of Encounter, CeSOS
IMT-19-2013	Aglen, Ida	VIV in Free Spanning Pipelines, CeSOS
IMT-1-2014	Song, An	Theoretical and experimental studies of wave diffraction and radiation loads on a horizontally submerged perforated plate, CeSOS

IMT-2-2014	Rogne, Øyvind Ygre	Numerical and Experimental Investigation of a Hinged 5-body Wave Energy Converter, CeSOS
IMT-3-2014	Dai, Lijuan	Safe and efficient operation and maintenance of offshore wind farms ,IMT
IMT-4-2014	Bachynski, Erin Elizabeth	Design and Dynamic Analysis of Tension Leg Platform Wind Turbines, CeSOS
IMT-5-2014	Wang, Jingbo	Water Entry of Freefall Wedged – Wedge motions and Cavity Dynamics, CeSOS
IMT-6-2014	Kim, Ekaterina	Experimental and numerical studies related to the coupled behavior of ice mass and steel structures during accidental collisions, IMT
IMT-7-2014	Tan, Xiang	Numerical investigation of ship's continuous- mode icebreaking in leverl ice, CeSOS
IMT-8-2014	Muliawan, Made Jaya	Design and Analysis of Combined Floating Wave and Wind Power Facilities, with Emphasis on Extreme Load Effects of the Mooring System, CeSOS
IMT-9-2014	Jiang, Zhiyu	Long-term response analysis of wind turbines with an emphasis on fault and shutdown conditions, IMT
IMT-10-2014	Dukan, Fredrik	ROV Motion Control Systems, IMT
IMT-11-2014	Grimsmo, Nils I.	Dynamic simulations of hydraulic cylinder for heave compensation of deep water drilling risers, IMT
IMT-12-2014	Kvittem, Marit I.	Modelling and response analysis for fatigue design of a semisubmersible wind turbine, CeSOS
IMT-13-2014	Akhtar, Juned	The Effects of Human Fatigue on Risk at Sea, IMT
IMT-14-2014	Syahroni, Nur	Fatigue Assessment of Welded Joints Taking into Account Effects of Residual Stress, IMT
IMT-1-2015	Bøckmann, Eirik	Wave Propulsion of ships, IMT
IMT-2-2015	Wang, Kai	Modelling and dynamic analysis of a semi-submersible floating vertical axis wind turbine, CeSOS
IMT-3-2015	Fredriksen, Arnt Gunvald	A numerical and experimental study of a two-dimensional body with moonpool in waves and current, CeSOS
IMT-4-2015	Jose Patricio Gallardo Canabes	Numerical studies of viscous flow around bluff bodies, IMT
IMT-5-2015	Vegard Longva	Formulation and application of finite element techniques for slender marine structures subjected to contact interactions, IMT
IMT-6-2015	Jacobus De Vaal	Aerodynamic modelling of floating wind turbines, CeSOS

IMT-7-2015	Fachri Nasution	Fatigue Performance of Copper Power Conductors, IMT
IMT-8-2015	Oleh I Karpa	Development of bivariate extreme value distributions for applications in marine technology,CeSOS
IMT-9-2015	Daniel de Almeida Fernandes	An output feedback motion control system for ROVs, AMOS
IMT-10-2015	Bo Zhao	Particle Filter for Fault Diagnosis: Application to Dynamic Positioning Vessel and Underwater Robotics, CeSOS
IMT-11-2015	Wenting Zhu	Impact of emission allocation in maritime transportation, IMT
IMT-12-2015	Amir Rasekhi Nejad	Dynamic Analysis and Design of Gearboxes in Offshore Wind Turbines in a Structural Reliability Perspective, CeSOS
IMT-13-2015	Arturo Jesùs Ortega Malca	Dynamic Response of Flexibles Risers due to Unsteady Slug Flow, CeSOS
IMT-14-2015	Dagfinn Husjord	Guidance and decision-support system for safe navigation of ships operating in close proximity, IMT
IMT-15-2015	Anirban Bhattacharyya	Ducted Propellers: Behaviour in Waves and Scale Effects, IMT
IMT-16-2015	Qin Zhang	Image Processing for Ice Parameter Identification in Ice Management, IMT
IMT-1-2016	Vincentius Rumawas	Human Factors in Ship Design and Operation: An Experiential Learning, IMT
IMT-2-2016	Martin Storheim	Structural response in ship-platform and ship-ice collisions, IMT
IMT-3-2016	Mia Abrahamsen Prsic	Numerical Simulations of the Flow around single and Tandem Circular Cylinders Close to a Plane Wall, IMT
IMT-4-2016	Tufan Arslan	Large-eddy simulations of cross-flow around ship sections, IMT
IMT-5-2016	Pierre Yves-Henry	Parametrisation of aquatic vegetation in hydraulic and coastal research,IMT
IMT-6-2016	Lin Li	Dynamic Analysis of the Instalation of Monopiles for Offshore Wind Turbines, CeSOS
IMT-7-2016	Øivind Kåre Kjerstad	Dynamic Positioning of Marine Vessels in Ice, IMT

IMT-8-2016	Xiaopeng Wu	Numerical Analysis of Anchor Handling and Fish Trawling Operations in a Safety Perspective, CeSOS
IMT-9-2016	Zhengshun Cheng	Integrated Dynamic Analysis of Floating Vertical Axis Wind Turbines, CeSOS
IMT-10-2016	Ling Wan	Experimental and Numerical Study of a Combined Offshore Wind and Wave Energy Converter Concept
IMT-11-2016	Wei Chai	Stochastic dynamic analysis and reliability evaluation of the roll motion for ships in random seas, CeSOS
IMT-12-2016	Øyvind Selnes Patricksson	Decision support for conceptual ship design with focus on a changing life cycle and future uncertainty, IMT
IMT-13-2016	Mats Jørgen Thorsen	Time domain analysis of vortex-induced vibrations, IMT
IMT-14-2016	Edgar McGuinness	Safety in the Norwegian Fishing Fleet – Analysis and measures for improvement, IMT
IMT-15-2016	Sepideh Jafarzadeh	Energy effiency and emission abatement in the fishing fleet, IMT
IMT-16-2016	Wilson Ivan Guachamin Acero	Assessment of marine operations for offshore wind turbine installation with emphasis on response-based operational limits, IMT
IMT-17-2016	Mauro Candeloro	Tools and Methods for Autonomous Operations on Seabed and Water Coumn using Underwater Vehicles, IMT
IMT-18-2016	Valentin Chabaud	Real-Time Hybrid Model Testing of Floating Wind Tubines, IMT
IMT-1-2017	Mohammad Saud Afzal	Three-dimensional streaming in a sea bed boundary layer
IMT-2-2017	Peng Li	A Theoretical and Experimental Study of Wave-induced Hydroelastic Response of a Circular Floating Collar
IMT-3-2017	Martin Bergström	A simulation-based design method for arctic maritime transport systems
IMT-4-2017	Bhushan Taskar	The effect of waves on marine propellers and propulsion
IMT-5-2017	Mohsen Bardestani	A two-dimensional numerical and experimental study of a floater with net and sinker tube in waves and current
IMT-6-2017	Fatemeh Hoseini Dadmarzi	Direct Numerical Simualtion of turbulent wakes behind different plate configurations

IMT-7-2017	Michel R. Miyazaki	Modeling and control of hybrid marine power plants
IMT-8-2017	Giri Rajasekhar Gunnu	Safety and effiency enhancement of anchor handling operations with particular emphasis on the stability of anchor handling vessels
IMT-9-2017	Kevin Koosup Yum	Transient Performance and Emissions of a Turbocharged Diesel Engine for Marine Power Plants
IMT-10-2017	Zhaolong Yu	Hydrodynamic and structural aspects of ship collisions
IMT-11-2017	Martin Hassel	Risk Analysis and Modelling of Allisions between Passing Vessels and Offshore Installations
IMT-12-2017	Astrid H. Brodtkorb	Hybrid Control of Marine Vessels – Dynamic Positioning in Varying Conditions
IMT-13-2017	Kjersti Bruserud	Simultaneous stochastic model of waves and current for prediction of structural design loads
IMT-14-2017	Finn-Idar Grøtta Giske	Long-Term Extreme Response Analysis of Marine Structures Using Inverse Reliability Methods
IMT-15-2017	Stian Skjong	Modeling and Simulation of Maritime Systems and Operations for Virtual Prototyping using co-Simulations
IMT-1-2018	Yingguang Chu	Virtual Prototyping for Marine Crane Design and Operations
IMT-2-2018	Sergey Gavrilin	Validation of ship manoeuvring simulation models
IMT-3-2018	Jeevith Hegde	Tools and methods to manage risk in autonomous subsea inspection,maintenance and repair operations
IMT-4-2018	Ida M. Strand	Sea Loads on Closed Flexible Fish Cages
IMT-5-2018	Erlend Kvinge Jørgensen	Navigation and Control of Underwater Robotic Vehicles
IMT-6-2018	Bård Stovner	Aided Intertial Navigation of Underwater Vehicles
IMT-7-2018	Erlend Liavåg Grotle	Thermodynamic Response Enhanced by Sloshing in Marine LNG Fuel Tanks
IMT-8-2018	Børge Rokseth	Safety and Verification of Advanced Maritime Vessels
IMT-9-2018	Jan Vidar Ulveseter	Advances in Semi-Empirical Time Domain Modelling of Vortex-Induced Vibrations

IMT-10-2018	Chenyu Luan	Design and analysis for a steel braceless semi-submersible hull for supporting a 5-MW horizontal axis wind turbine
IMT-11-2018	Carl Fredrik Rehn	Ship Design under Uncertainty
IMT-12-2018	Øyvind Ødegård	Towards Autonomous Operations and Systems in Marine Archaeology
IMT-13- 2018	Stein Melvær Nornes	Guidance and Control of Marine Robotics for Ocean Mapping and Monitoring
IMT-14-2018	Petter Norgren	Autonomous Underwater Vehicles in Arctic Marine Operations: Arctic marine research and ice monitoring
IMT-15-2018	Minjoo Choi	Modular Adaptable Ship Design for Handling Uncertainty in the Future Operating Context
MT-16-2018	Ole Alexander Eidsvik	Dynamics of Remotely Operated Underwater Vehicle Systems
IMT-17-2018	Mahdi Ghane	Fault Diagnosis of Floating Wind Turbine Drivetrain- Methodologies and Applications
IMT-18-2018	Christoph Alexander Thieme	Risk Analysis and Modelling of Autonomous Marine Systems
IMT-19-2018	Yugao Shen	Operational limits for floating-collar fish farms in waves and current, without and with well-boat presence
IMT-20-2018	Tianjiao Dai	Investigations of Shear Interaction and Stresses in Flexible Pipes and Umbilicals
IMT-21-2018	Sigurd Solheim Pettersen	Resilience by Latent Capabilities in Marine Systems
IMT-22-2018	Thomas Sauder	Fidelity of Cyber-physical Empirical Methods. Application to the Active Truncation of Slender Marine Structures
IMT-23-2018	Jan-Tore Horn	Statistical and Modelling Uncertainties in the Design of Offshore Wind Turbines
IMT-24-2018	Anna Swider	Data Mining Methods for the Analysis of Power Systems of Vessels
IMT-1-2019	Zhao He	Hydrodynamic study of a moored fish farming cage with fish influence
IMT-2-2019	Isar Ghamari	Numerical and Experimental Study on the Ship Parametric Roll Resonance and the Effect of Anti-Roll Tank
IMT-3-2019	Håkon Strandenes	Turbulent Flow Simulations at Higher Reynolds Numbers